NEUTRINO PHYSICS AT THE TEVATRON

R.Blair, Y.Chu, Jin N., D.MacFarlane, R. Messner
D.Novikoff, M.Purohit, F.Sciulli, and M.Shaevitz
California Institute of Technology, Pasadena, California 91125

F.Merritt, B.Aker
University of Chicago, Chicago, Illinois 60637

D.Edwards, E.Fisk, Y.Fukushima, D.Yovanovitch, Q.Kerns, T.Kondo,
P.Rapidis, S.Segler, R.Stefanski, and D.Theriot
Fermi National Accelerator Lab, Batavia, Illinois 60510

A.Bodek, R.Coleman, W.Marsh
Univesity of Rochester, Rochester, New York 14627

O.Fackler and K.Jenkins
Rockefeller University, New York, New York 10021

April 1980

Spokesmen:
F.Sciulli
M.Shaevitz
Caltech

ABSTRACT

As part of our continuing program in neutrino physics at Fermilab, we propose to use the Lab E detector to investigate neutrino and antineutrino interactions at Tevatron energies. Emphasis is placed on charged current physics with measurements of structure functions and absolute cross sections using data of a Tevatron run combined with our present sample of E616. In addition, we will study neutral current interactions and multimuon events for indications of new phenomena in the higher energy regime accessible at the Tevatron.

An early run of 2×10^{18} protons with the dichromatic beam at the Tevatron would extend the Q^2 range of our data to greater than 500 GeV^2 and allow definitive tests of the present strong interaction theory, QCD. The increased range in Q^2 provided by the Tevatron data will, when combined with E616 data already taken, improve the errors on α_s, the quark-gluon coupling constant, by a factor of 3 to 4. Furthermore the data will provide measurements of $F_L = F_2 - 2xF_1$ or $R = F_L/2xF_1$ in a region where theoretical uncertainties are small. The proposed run would yield about 150,000 neutrino and antineutrino events and lead to measurements of R with statistical errors of $0.03 < \Delta R < 0.1$ for $x < 0.5$.

The Lab E detector and flux monitoring system at Fermilab are optimized for the measurement of absolute cross sections and structure functions. The detector is a massive device with the target-calorimeter separate from the muon-spectrometer. The experimentally verified resolutions of the Lab E detector and the 1-4% absolute measurements of ν and $\bar{\nu}$ fluxes are sufficient for QCD tests in the present energy regime and are more than adequate for the higher Tevatron energies. In all cases, we believe the systematic errors to be smaller than the expected statistical errors.

We are also considering upgrades for the detector to improve its physics and multi-event capabilities. Appendix A describes a possible scheme involving replacement of the spark chambers with analog readout drift chambers. We intend to investigate this option by building prototype chambers and electronics in the near future.

TABLE OF CONTENTS

List of Figures

List of Figures

List of Figures

List of Tables

I. Introduction

There are several motivations for pursuing the physics of neutrino collisions with nucleons. These include:

(a) Measurement of the neutral current cross-section and its energy dependence as a precise test of the Weinberg-Salaam Theory.

(b) Observation of multi-muon phenomena. The interpretation of multimuon events as originating from charm allows a derivation of the strange sea distribution. The energy dependence of multi-muon phenomena could be of great importance to pointing to new production mechanisms or existence of new quantum numbers. (See Appendix G)

(c) Measurement of charged current cross-sections, on which we will concentrate.

The interpretation of the inclusive charged current processes

$$\nu_\mu + N \to \mu^- + X \qquad (1a)$$

$$\bar{\nu}_\mu + N \to \mu^+ + X \qquad (1b)$$

as the scattering from constituents more fundamental than the nucleon, i.e. quarks, has had great success. At lower energies, these predictions were expected to be no more accurate than ~ 20% due to the presence of M^2/Q^2 effects (where M is of the order of the nucleon mass) and, historically, due to the theoretical ignorance of the quantative nature of the force between quarks. The three structure functions: $F_2(x,Q^2)$, $xF_3(x,Q^2)$, $F_1(x,Q^2)$ are measurable by taking the cross-section sums and differences for processes (1a) and (1b):

$$\frac{d\sigma^\nu + d\sigma^{\bar{\nu}}}{dxdy} = \frac{G^2ME}{\pi}\left[\{1 + (1-y)^2\}\, 2xF_1(x,Q^2) + 2(1-y)\, F_L(x,Q^2)\right]$$

$$\frac{d\sigma^\nu - d\sigma^{\bar{\nu}}}{dxdy} = \frac{G^2ME}{\pi}\, xF_3(x,Q^2)\left[1-(1-y)^2\right] \qquad (2)$$

where:

$$F_L(x,Q^2) = R(x,Q^2)\ 2xF_1(x,Q^2)$$

$$F_2(x,Q^2) = (1+R)\ 2xF_1(x,Q^2)$$

The early free quark model predicts "scaling", i.e. that F_1, F_3, and F_L are independent of Q^2 and that $R = F_L/2xF_1 = 0$. Qualitative corroboration of this simple picture came with the electron-nucleon inelastic data from SLAC[1] at $E \leq 18$ GeV and the neutrino-nucleon data from Cern-Gargamelle at even lower energy. Although the data did not scale very well in the variable $x = Q^2/2M\nu$, redefinition of the scaling variable

$$x' = \frac{x}{1 + M^2x/Q^2}$$

improved the behavior at large x' to give scaling at roughly the 20% level, assuming R to be about 0.18 (See figure 1).

More recently, theoretical developments relating to the forces between quarks (QCD) have led to well-defined predictions for the Q^2 dependence of these structure functions. Unfortunately, these predictions are presently rigorous only in Q^2-regions where (a) the binding energies associated with the quark wave functions in the nucleon are negligible and (b) the perturbative QCD series expansion converges reasonably rapidly (i.e. where the quark-gluon coupling constant is small). In general, both of these conditions are valid only if Q^2 is large ($Q^2 > 20$ GeV^2).

Figure 2 shows the zeroth-order (free quark) and first-order diagrams that are expected from asymptotic QCD. These are such that the xF_3 structure function evolves as follows[2]:

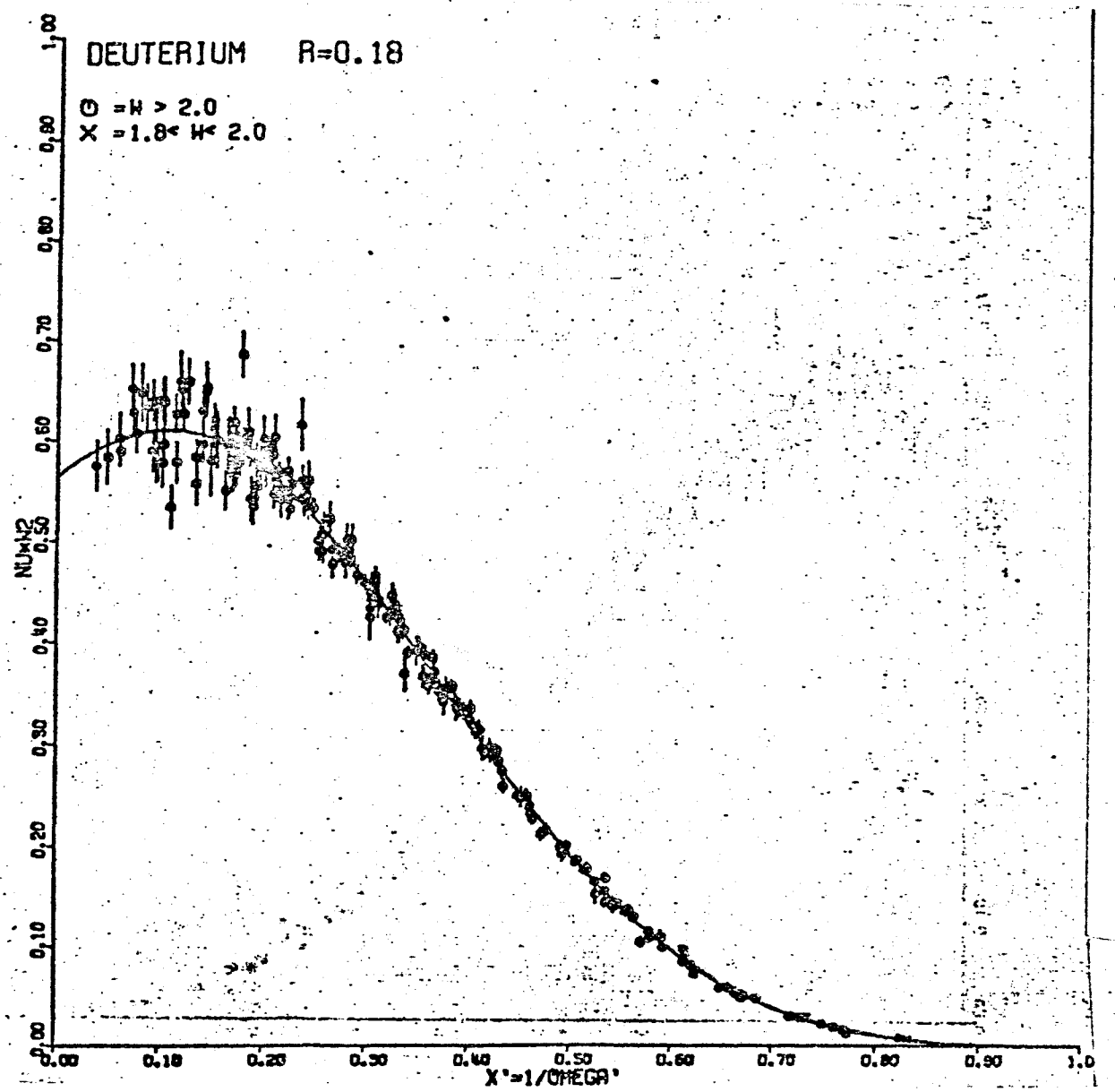

Figure 1: νW_{2_D} vs. X' for W greater than 2 GeV and Q^2 greater than 1.0 $(GeV/c)^2$

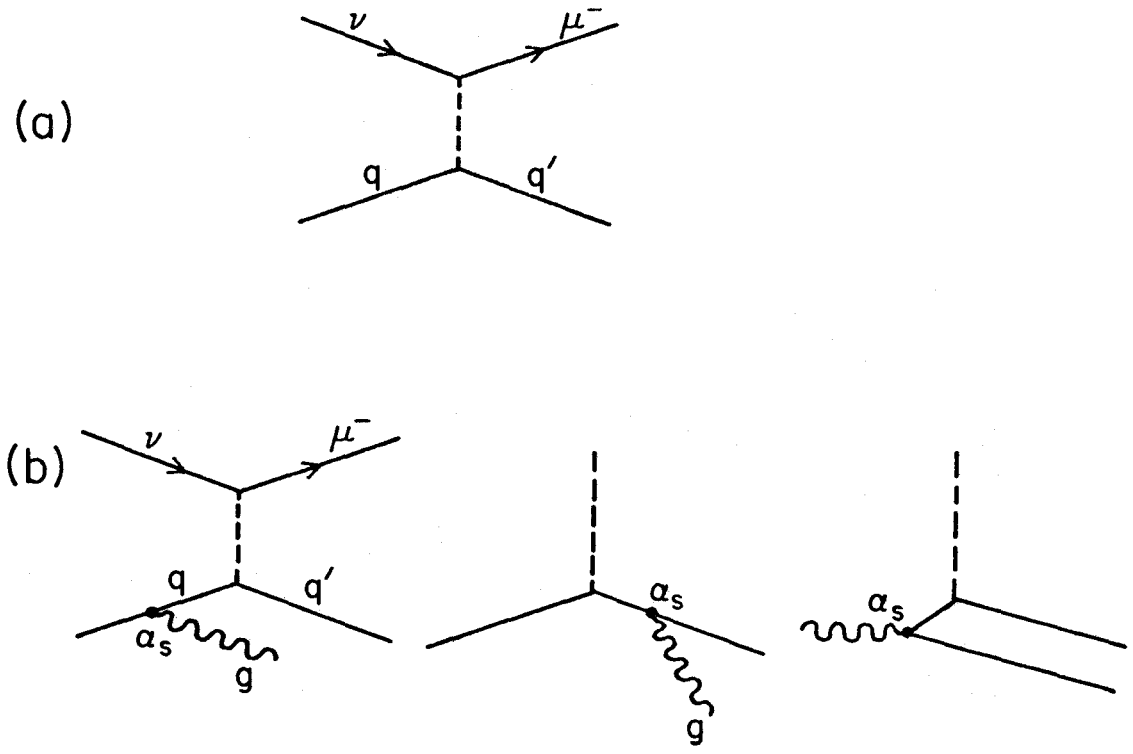

Figure 2: Zeroth and first order diagrams of QCD

$$\frac{\partial x F_3(x,Q^2)}{\partial \ell n Q^2} = \frac{\alpha_s(Q^2)}{3\pi} \{3 + 4\ \ell n\ (1-x)\}\ x F_3(x,Q^2) \qquad (3)$$

$$+ \int_x^1 dw\ \frac{2}{1-w} \left[(1+w^2)\ \frac{x F_3(\frac{x}{w}, Q^2)}{w} - 2x F_3(x,Q^2) \right]$$

where $\alpha_s(Q^2)$ is the quark-gluon coupling constant (see figure 2).

As can be seen from the formula, the evolution of xF_3 only involves integrals of the quark structure function and does not depend on the gluon distribution. This behavior is a result of the fact that only the first two diagrams in figure 2b contribute to the xF_3 evolution. On the other hand, the changes in ($2xF_1$ or F_2) with Q^2 are more complicated and involve gluon terms from the third diagram in figure 2b.

A measurement of $xF_3\ (x,Q^2)$ at a single value of Q^2 permits the right-hand side of formula (3) to be calculated up to the factor $\alpha_s\ (Q^2)$. The experimental variation of xF_3 with Q^2 then permits extraction of α_s.

The most accurate data[3] available on xF_3, shown in Figure 3, is based on 20,000 events. The QCD fits are really not much better than fits incorporating expected M^2/Q^2 effects. If we are, indeed, presently observing M^2/Q^2 effects, this would imply the effective re-establishment of scaling at high Q^2. In any case, we are presently far from having a good, quantitative measurement of α_s in this Q^2 region ($\sim$ 50 GeV^2).

We believe that data taken in E616 combined with Tevatron data will rectify this problem. (See Section IV). We anticipate that a modest Tevatron run will permit α_s to be measured at $Q^2 \simeq 50$ GeV^2 to better than 10%, if its value is as large as 0.3. If scaling were re-established, an upper limit $\alpha_s < 0.1$ would be possible (see section IV).

The values of $F_2(x,Q^2)$ and $F_L(x,Q^2)$ are obtained from fits to the sum of neutrino and antineutrino cross section data (equation 2a). The Q^2-evolution of F_2 is directly related to the same quark-gluon coupling constant, α_s, and

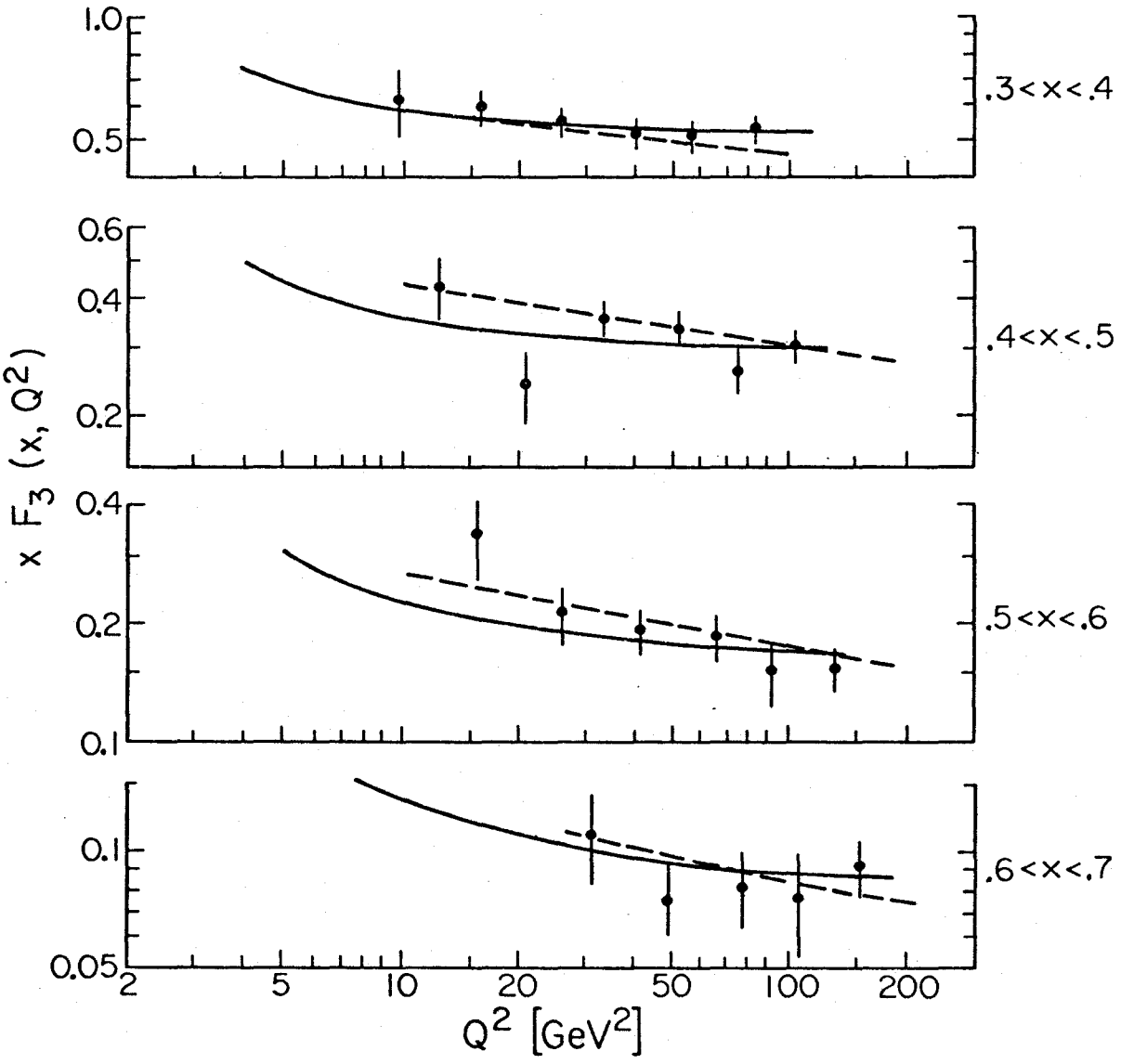

Figure 3: xF_3 vs. Q^2 as measured by the CDHS[1] group. Solid line is a fit using "perfect scaling" in the in the variable $x' = x/(1 + M^2/Q^2)$ dashed line is a QCD fit by Buras-Gaemers[2].

the gluon distribution, $G(x,Q^2)$. This data can be used, once α_s is known from the xF_3 data, to obtain $G(x,Q^2)$. As further check on the completeness of the picture, F_L can be predicted by the theory[4]

$$F_L(x,Q^2) = \frac{\alpha_s(Q^2)}{2\pi}\ x^2\left[\int_x^1 \frac{1}{z^3}\ \frac{8}{3}\ F_2(z,Q^2)\ dz + \int_x^1 \frac{1}{z^3}\ 16\ (1-\frac{x}{z})G(z,Q^2)\ dz\right] \quad (4)$$

This F_L is predicted to vary slowly (logarithmically) with Q^2, while M^2/Q^2 effects would make it fall quickly. We anticipate that the E616 data combined with Tevatron data will allow a clear delineation of these two possibilities and will provide an indisputable measurement of α_s (see Section IV). The systematic errors associated with such a measurement should be small compared to the statistical errors (see proposal P616).

In summary, we have concluded after much study that this experiment using high energy neutrino collisions is likely to provide the most definitive method for investigating the behavior of the nucleon structure functions in our present Q^2-region (including the Tevatron). Systematic errors and resolutions are well matched to extracting the structure functions, F_2, F_3, F_L from the data using equations (2). This is in contrast to muon or electron scattering, for example, where considerably better resolutions are required to compensate for a multiplying $Q^{-4} = (2MExy)^{-2}$ factor, and where the very important parity-violating structure function, xF_3, cannot be measured. Furthermore, an increase in the Q^2 range of the data provided by the Tevatron will, when combined with E616 data already taken, permit a reduction in errors on α_s (or an upper limit on α_s) by a factor of between 3 and 4 (see Section IV).

We proceed in the next sections to describe our existing detection equipment and the expected event rates at the Tevatron. In section IV we look, in more detail, at what might reasonably be expected from

Tevatron data, combined with E616 data, with regard to tests of QCD. In section V, we summarize and make specific our requests. Appendix A deals with a possible up-grade of the Lab E detection equipment that could be very important for long-term use of the lab E detector.

II. Lab E Detector and Flux Monitoring

As described in the proposal for E616, the only model independent method to extract the nucleon structure functions, $F_2(x,Q^2)$ and $F_L(x,Q^2)$, from neutrino (equation 2) is to fit y distributions at fixed hadron energy. This assures that $Q^2 = 2ME_{HAD}\,x$ will also be constant. Different $y = E_{HAD}/E_\nu$ values are obtained by varying the neutrino energy, E_ν. This method imposes severe experimental requirements which can only be satisfied by using a well instrumented dichromatic neutrino beam. In order to combine various neutrino energies, one must have absolute normalization of the measured cross sections demanding secondary fluxes to be known to about 1-2%. Measurement errors which tend to smear the extracted structure functions, especially at high x values, must be understood and reduced, if possible, to minimize large corrections. The flat neutrino energy spectrum from a dichromatic beam is also essential in reducing these smearing errors. In the following sections, we investigate the use of our flux measuring system and the Lab E detector to make such measurements at Tevatron energies.

A. Flux Monitoring

Since structure functions are obtained by combining flux normalized neutrino and antineutrino data at fixed x and Q^2, the accuracy of the structure function is no better than our knowledge of the neutrino flux. It is, therefore, important to review the existing monitoring system and to discuss changes which are needed for the Tevatron.

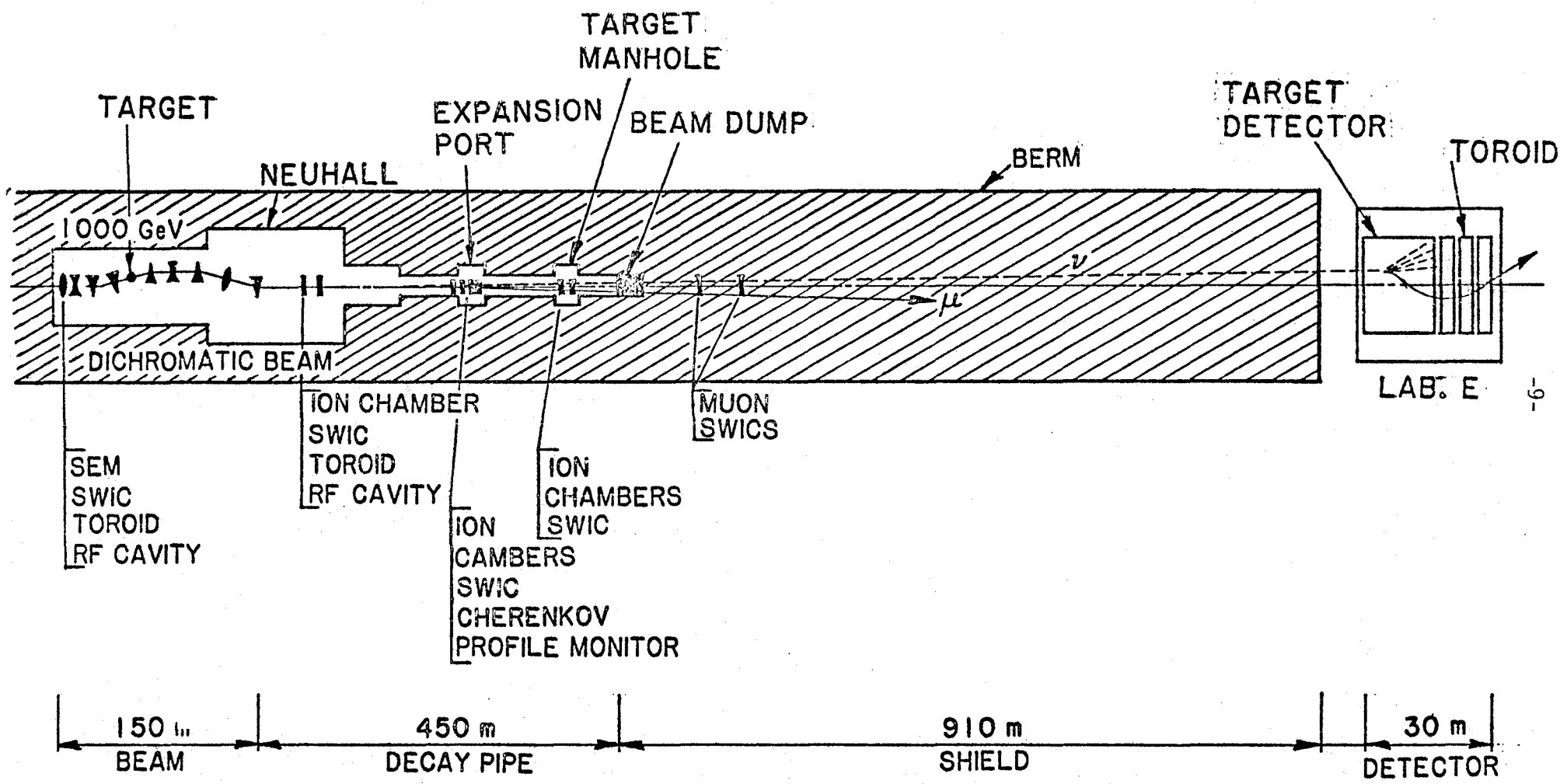

Figure 4: Proposed layout for the Tevatron Neutrino Experiment

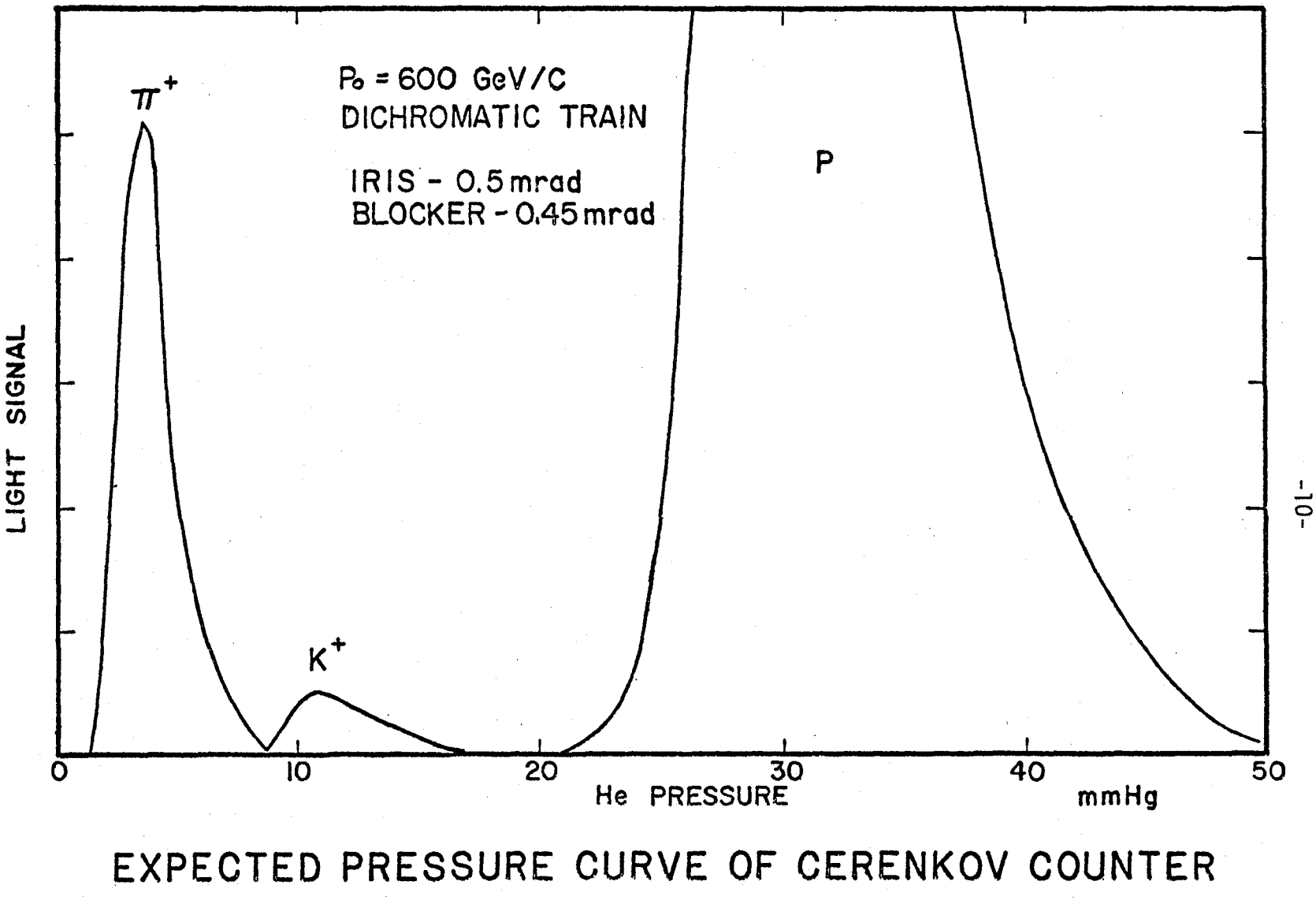

Figure 5: An example of a Cerenkov curve from 600 GeV/c beam at the Tevatron.

The present flux measurements are discussed in detail in Appendix A. Utilizing the techniques discussed there, we conclude that pion and kaon fluxes are being measured at the 1-2% and 2-4% level, respectively.

With the existing system plus some improvements, we estimate that kaon and pion fluxes for the proposed Tevatron dichromatic beam can be measured to 1-2%. The proposed changes are shown in Fig. 4 . They are: 1) the addition of a new flux monitoring station just downstream of the dichromatic train; 2) an improved Cerenkov counter; and 3) the addition of two muon SWIC's downstream of the hadron dump at the end of the decay pipe.

The new flux monitoring station incorporates a precision ion chamber to measure particle fluxes, a split plate ion chamber to measure the mean beam position at the end of the train, a profile SWIC, and a toroid to measure the particle flux. The reliability and utility of the ion chambers and SWICs have been proven in E616 and other experiments.

The large diameter toroid built for E616 proved to have adequate sensitivity to the beam current but was overly sensitive to particles passing through its high permeability iron core. Since the beam size at the exit of the train is smaller than at the expansion port (where the E616 toroid was located) we expect the halo at the iron core radius to be small enough to permit reliable operation of the toroid. It is important to have redundancy in the measurement of beam flux. The toroid, if reliable at the few percent level, will provide an independent measurement of the secondary beam intensity. This measurement will serve as a check on the beam intensity measured by the ion chambers which have different systematic errors.

The Cerenkov counter should be modified to further reduce the background level, and the data taking process should be automated. (An example of a Tevatron Cerenkov curve is shown in Figure 5.) The background due

to light scattering can be reduced by decreasing the number of mirrors in the optical path. The background due to particle interactions can be reduced by decreasing the amount of material upstream of the counter. The data taking process can be automated with the use of a microprocessor which will allow us to take adequate data in a reasonable length of time without it being the full time job dictated by the present arrangement.

An important addition to the E616 monitoring system was the muon SWIC. The muon flux, measured downstream of the decay pipe with a large area SWIC, has provided an important check on the number of pion neutrinos as calculated from the measured total particle flux and the kaon:pion:proton ratios determined with the Cerenkov counter. The present muon SWIC has an area of $1\ m^2$ and is not large enough to contain all of the muons from kaon decay. By constructing a larger SWIC (2m x 2m) it should be possible to intercept all of the muons originating in both kaon and pion decay for beam energies above 500 GeV.

In summary, we have learned a great deal about monitoring fluxes for normalized cross section measurements and believe that we can build a flux monitoring system which will measure pion and kaon fluxes at the 1-2% level.

B. Lab E Neutrino Detector:

The Lab E detector at Fermilab is optimized for the measurement of absolute cross-sections and structure functions. It is a large tonnage (1100 tons) device with the target-calorimeter separate from the muon spectrometer. A schematic drawing of the detector is shown in Fig. 6. A more complete description is provided in Appendix C. The target is composed of 680 tons of steel with transverse dimensions 3m x 3m and is interspersed with scintillation counters every 10cm of steel and with spark chambers every 20 cm. The non-magnetized nature of the target has

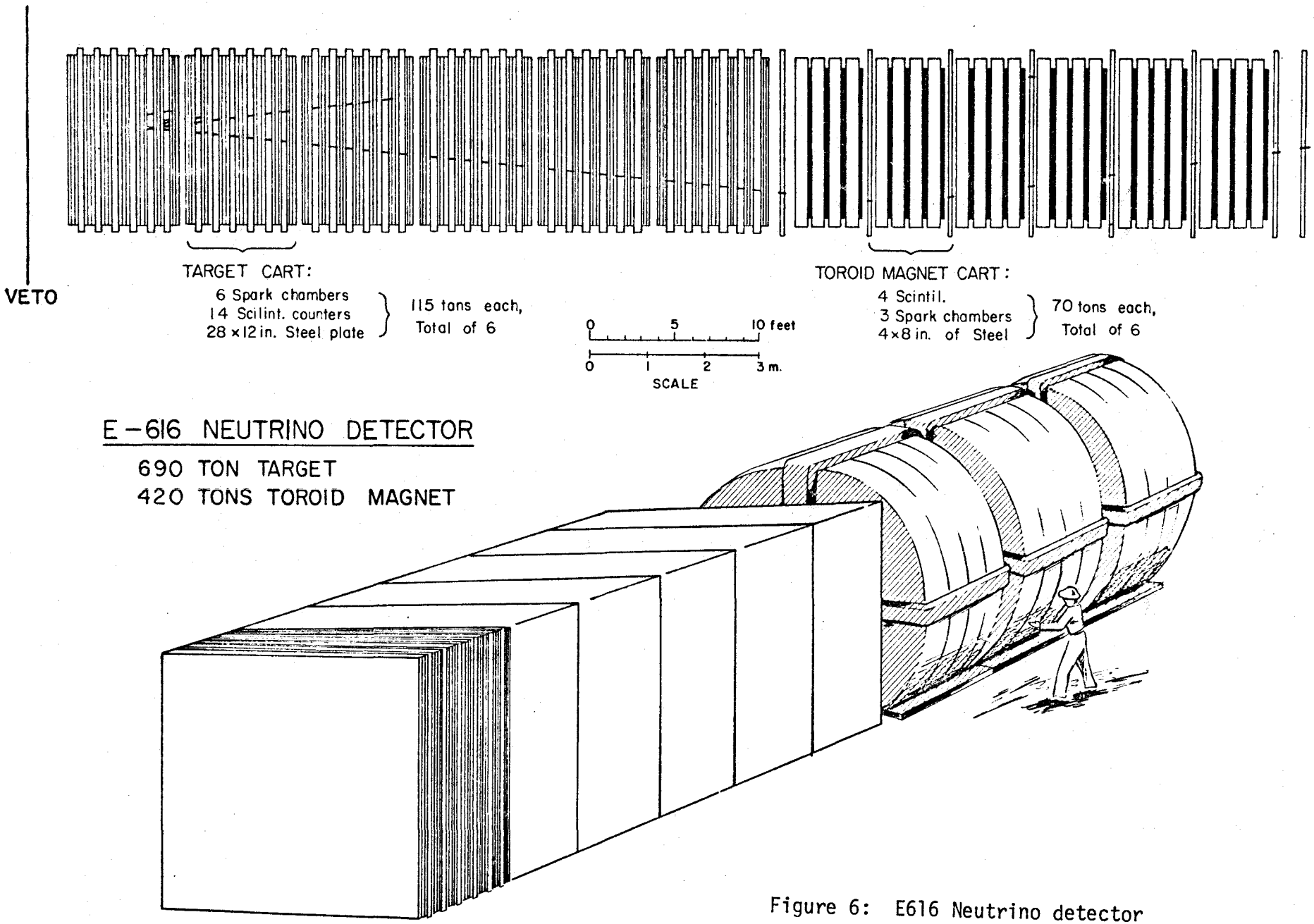

Figure 6: E616 Neutrino detector

several advantages over a magnetized one:

(1) The angle of the muon at the interaction vertex can be measured with much better accuracy in a non-magnetized medium with straight muon trajectories (See Appendix D and F). In addition, the high segmentation (chambers every 20cm of steel) and multi-spark capabilities of the spark chambers reduce the error in angle measurements, giving $\sigma_{\theta_\mu}^{PROJ} = (.3 + \frac{68\ GeV}{P})$ mR for a position error of 1mm. (Recent measurements have shown this precision to be 0.5mm in our detector.) A comparison of this detector with the present CERN CDHS detector (a magnetized target detector) shows the angular resolution to be better in our detector by more than a factor of 3.

(2) The scintillation counters have uniform response over most of their area (For radii less than 1m, the pulse height variation is less than 20%.) There are no dead regions in the center of the counters, so that standard calorimetric techniques can be used to obtain the hadronic energy with a demonstrated resolution of

$$\Delta E_{HAD}/E_{HAD} = .93/\sqrt{E_{HAD}} \qquad \text{(See appendix E)}$$

(3) The neutrino beam produced from the decays of pions and kaons is strongly peaked in the center of the detector. For example (Fig. 7), with a secondary beam energy of 500 GeV, all neutrinos from pion decay with energies $70 < E_\nu < 210$ GeV will be within .5m of the center: neutrinos from kaon decay with $250 < E_\nu < 475$ GeV will be within 1m. The Lab E detector has no significant non-uniformities in this important central region in contrast to a toroidal magnet system with a hole in the center.

Downstream of the target-caloriemter is a muon spectrometer composed of a 450 ton, 3.5m diameter, iron toroidal magnet with a $P_\perp$ kick of 2.4 GeV, spark chambers every 80cm, and scintillation counters every 20cm of steel. With this configuration, muon momenta can be measured with an error

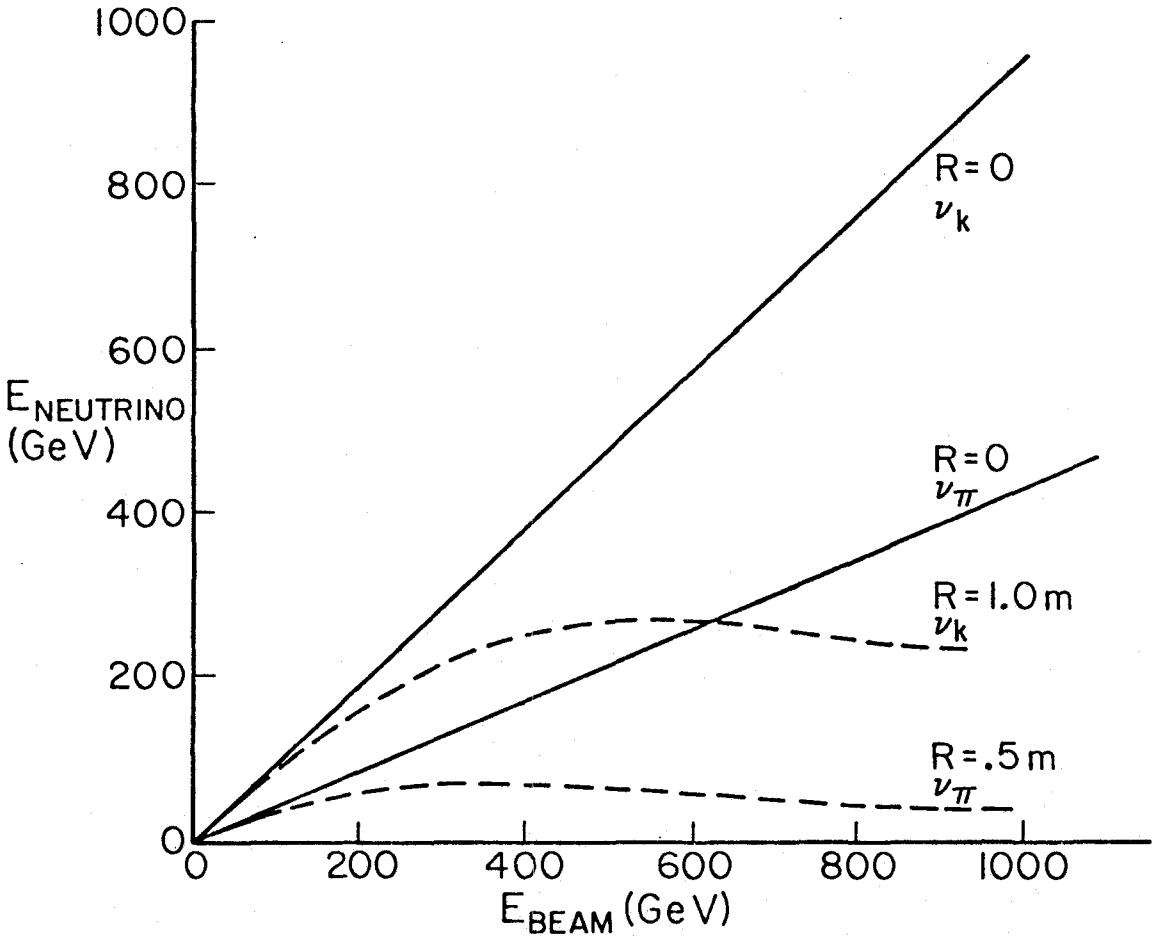

Figure 7: Neutrino energies at Lab E vs. secondary beam energy

$\frac{\Delta p}{p} \approx 11\%$ dominated by multiple scattering in the steel.

C. Resolution Study at Higher Energies

The main thrust of a neutrino experiment at the Tevatron will be to extend the structure function measurements to higher Q^2. This raises the question as to whether the present detector has adequate resolution at high energies and whether possible improvements could reduce the measurement errors significantly. It should be noted that most resolutions (except muon momentum errors) improve at higher energies. The x resolution, as mentioned before, is critical for structure function measurements; we will focus on errors for this variable. In terms of the measured quantities, the x resolution is given by:

$$\sigma_x^2 = \left(\frac{E_\nu}{2M}\,\frac{1-y}{y}\right)^2 \sigma_{\theta_\mu}^2 + (2-y)^2\, x^2 \left(\frac{\sigma_\mu}{E_\mu}\right)^2 + (1-y)^2\, x^2 \left(\frac{\sigma_{had}}{E_{had}}\right)^2 \qquad (6)$$

As is shown in Figure 8, the error at small x has its most significant contributions from muon angle and momentum resolution; at high x it is dominated by the muon momentum determination. For all x values with Q^2 greater than 50 GeV^2, the contribution from hadron energy errors to the x resolution is negligible and, thus, improvements in this measurement are not very relevant. (See Figure 9 (e) and (f)).

The muon angle measurement could be improved by a more precise position detector in the target. Figure 9 (a) and (b) shows a comparison of x resolution for detectors with 1mm and .25mm accuracy. There are some improvements at small x especially at low and high y. A recent analysis of data from E616 has shown the present spark chambers in the target to have .5mm resolution. Replacement of these chambers with drift chambers might lower the position error by a factor of two ($\sigma = 250\ \mu m$) and improve the x resolutions slightly.

Muon momentum resolution for the present detector is dominated by

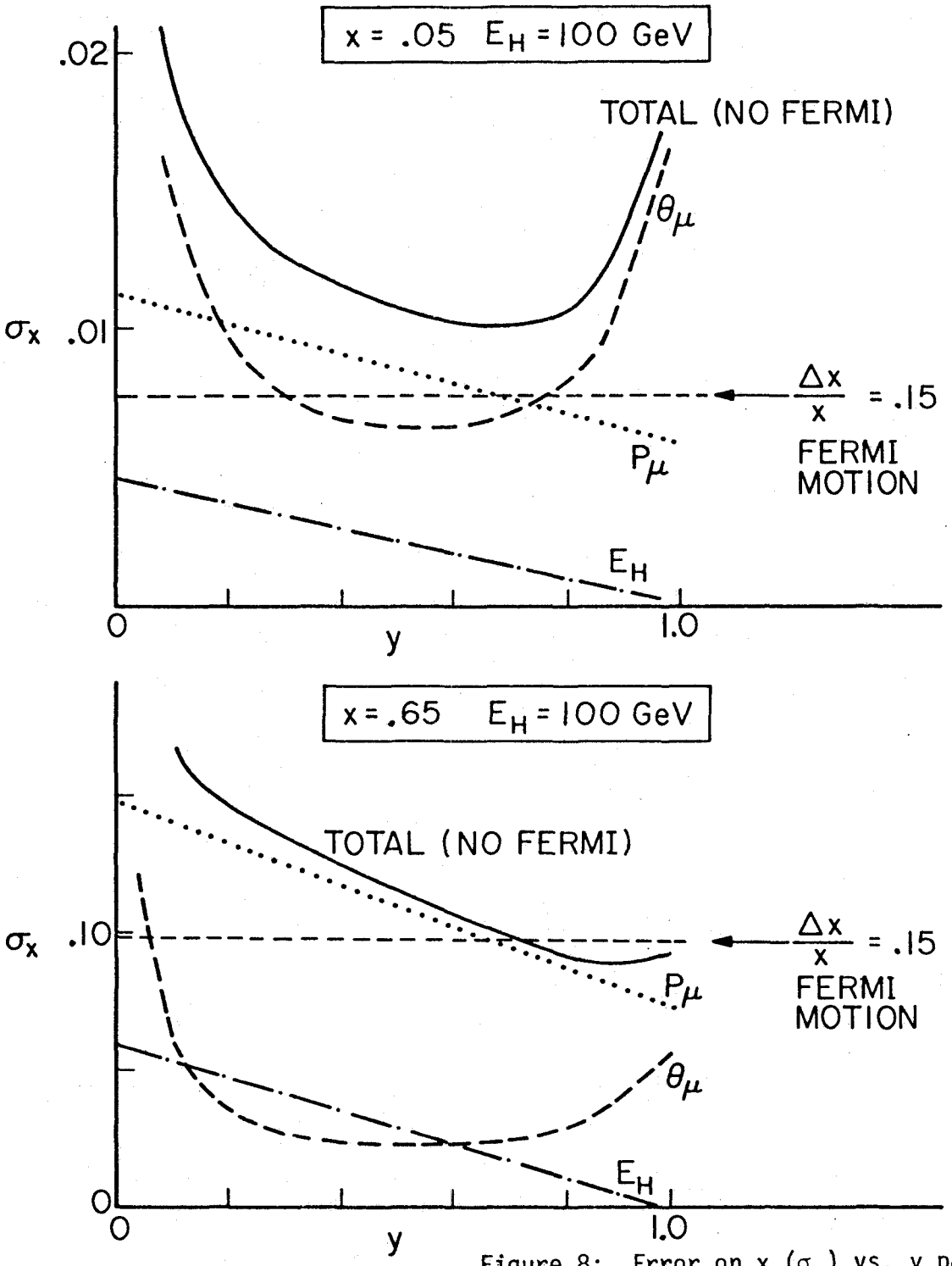

Figure 8: Error on x (σ_x) vs. y parameter for two x-values. The various curves show contributions from muon momentum (P_μ), muon angle (θ_μ), and hadron energy (E_H) measurement errors. The total includes all these contributions. The level of σ_x from Fermi motion is also indicated.

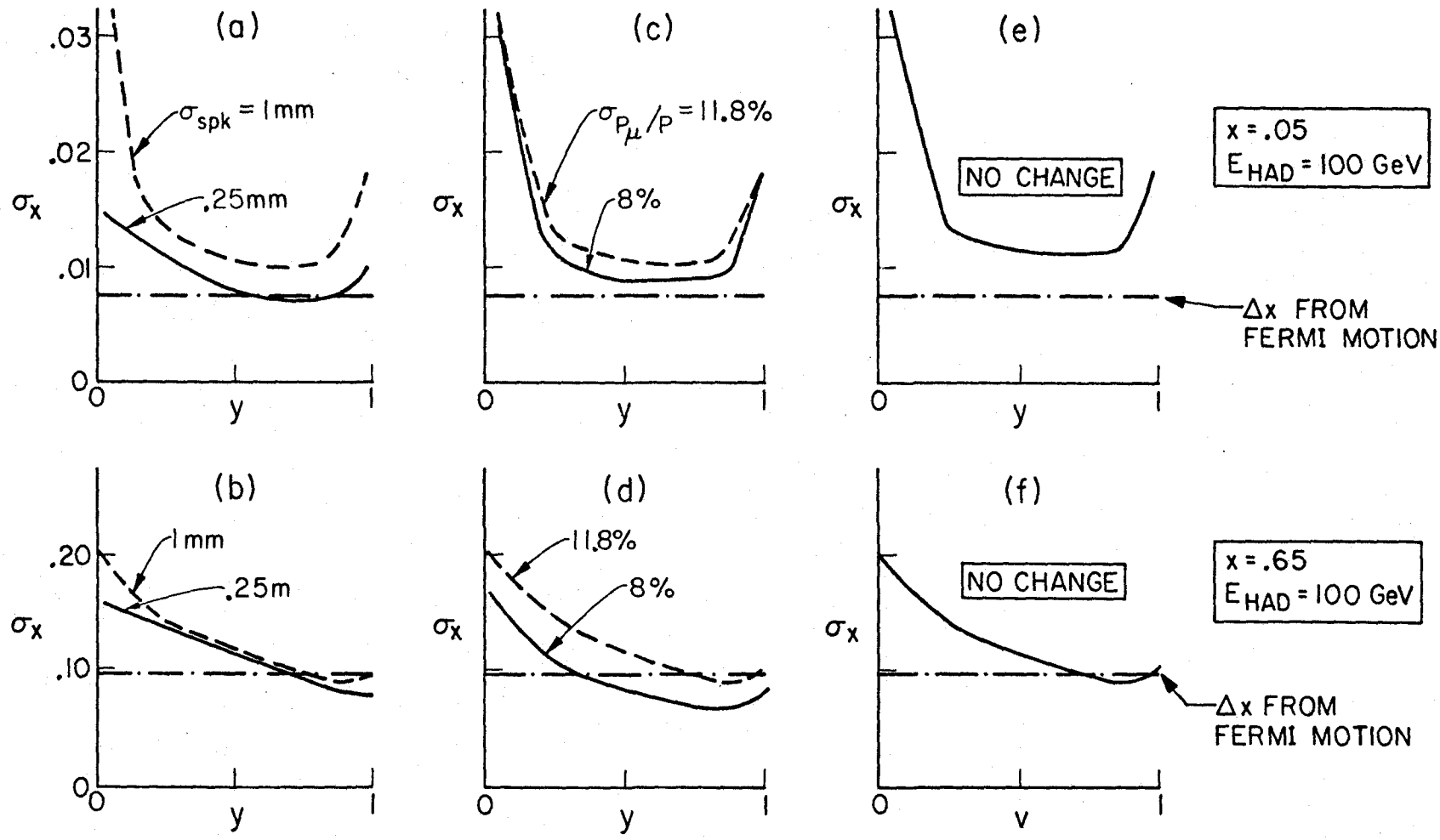

Position error (muon angle) resolution comparison σ_{spk} = 1mm → .25mm

Muon momentum resolution comparison (doubling toroid)

Hadron Energy resolution comparison (doubling number of counters)

Figure 9: Comparison of the x resolution for the present detector (dashed curve and various upgraded detectors (solid curve).

multiple scattering in the magnet steel. The resolution is given by

$$\left(\frac{\Delta P}{P}\right)^2 = .114^2 + (8.33 \times 10^{-5} P_\mu)^2 \qquad P_\mu \text{ in GeV}$$

which indicates that for muon energies up to 600 GeV, the contribution from position measurement error (the second term) is small. Improvements in the momentum measurement can be obtained by lengthening the magnet with corresponding reduction in error being proportional to the square root of the length. Doubling the length of the present magnet will reduce the muon momentum error from 11.4% to 8% and improve the x resolution as shown in Figure 9 (c) and (d). This modification would be expensive and would not change the x resolution substantially.

We conclude that the present detector has adequate precision to extract structure functions at Tevatron energies and we believe that no upgrade specifically aimed at improving resolutions is necessary.

III. Event Rates, Deadtime and Expected Event Sample

The fundamental predictions of QCD are related to changes in the structure functions with Q^2 and precise tests of this theory require measurements over a large Q^2 range. The present data sample of E616 will yield measurements for Q^2 up to ~ 100 GeV^2 with good statistical accuracy. A similar run at the Tevatron will extend these measurements to Q^2 of 500 GeV^2, though in the lower Q^2 region this run would have much larger errors than E616. The combination of these two data samples (E616 and the Tevatron) is a perfect match - E616 giving precise measurements at low Q^2 and the Tevatron experiment at the high Q^2 region. In this section we investigate possible running plans at the Tevatron with the idea of combining the new data with that from E616.

We plan to use the dichromatic beam for this experiment to get a wide range of neutrino energies with good flux normalization and with minimal

systematic errors. The beam has a momentum bite of $\frac{\Delta P}{P} = \pm 9\%$ and an angular resolution of .03 and .07 mR in the horizontal and vertical directions. The neutrino energy for a monochromatic (π,K) beam at energy E_o directed at the center of the detector is given by

$$E_o = \frac{E_o\,(1-m_\mu/m_{\pi,K})^2}{1 + r/r_o}$$

where r is the radius at the detector, and $r_o = D/\gamma$ with $\gamma = E_o/m_{\pi,K}$. (D is the distance from the decay pipe to the detector.) As can be seen from equation 7 and Figure 7, the (anti) neutrinos from kaon decay are higher in energy than those from pion decay for a given beam energy setting. For the study of rates we concentrate on the yield of neutrinos from kaon decay because these give the highest energy and highest Q^2 events.

It is well known that neutrino event rates increase quickly with beam energy. Figure 10 shows the expected neutrino event rate versus dichromatic beam momentum setting for 1000 GeV and 400 GeV primary protons. Comparing the rates for a 600 GeV setting with 1000 GeV primaries to that for a 250 GeV setting and 400 GeV primaries, one observes a factor of six increase for both K^+ and K^- events. This just compensates the extended cycle time (1 cycle/min) expected at the Tevatron and would lead to an approximately equal data accumulation rate, per calendar time, for the Tevatron experiment and E616. At lower beam settings the situation is different; for example, positive beam events with beam energies below 250 GeV have an average rate 2.5 times lower at the Tevatron than that observed in E616. To match the E616 neutrino event sample would require a Tevatron run of seven calendar months. On the other hand, the antineutrino rate is much higher at 250 and 500 GeV; the present antineutrino sample at these two energies could

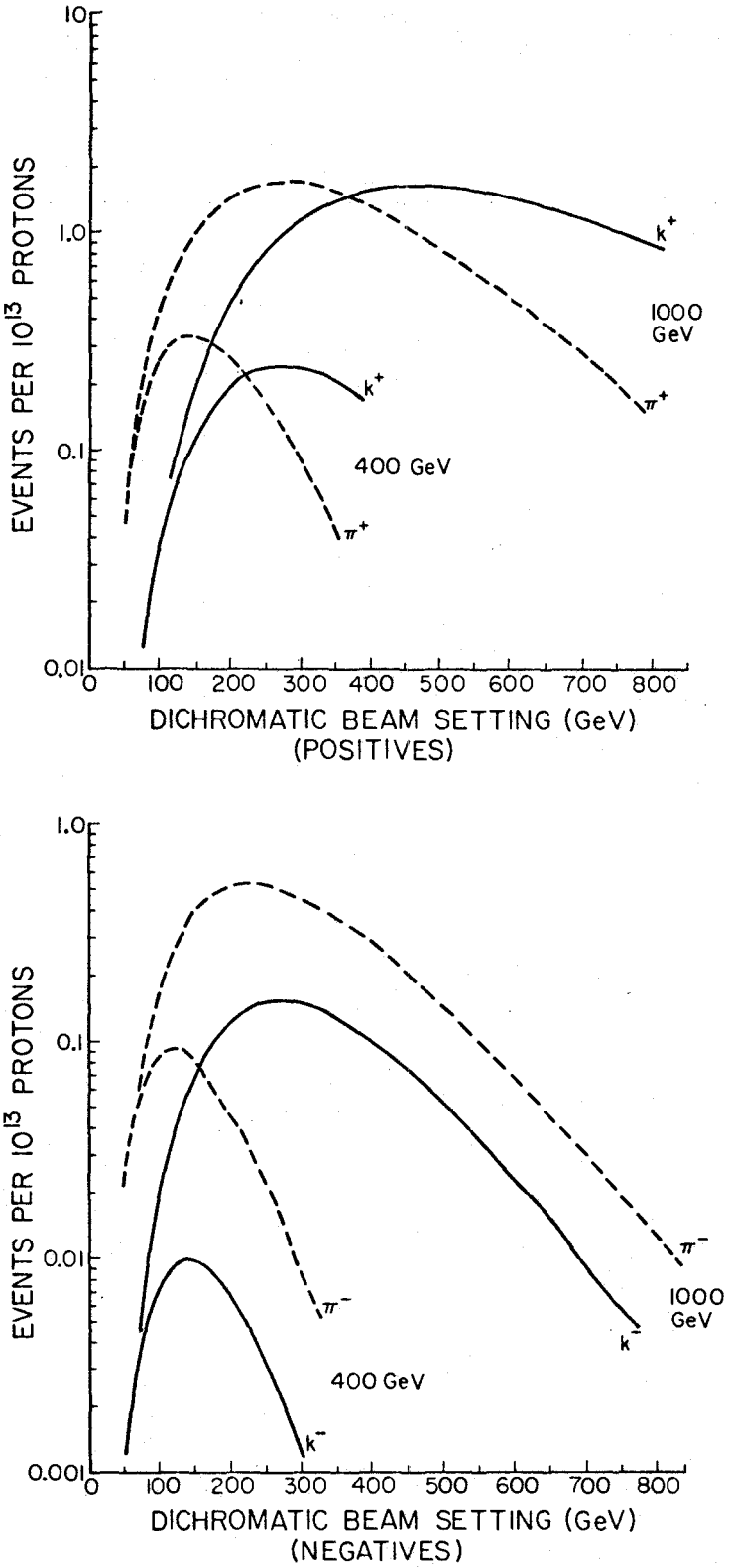

Figure 10: Events per 10^{13} protons vs. dichromatic beam setting. The top (bottom) plot is for neutrino (antineutrino) events with two sets of curves for 400 GeV and 1000 GeV incident protons.

be doubled by a modest two-week Tevatron run. A possible initial running scenario would include an extended run at 600 GeV, equally split between neutrinos and antineutrinos, and a short run for 200-250 GeV antineutrinos. This provides good coverage of the new higher energy regime, as well as supplementing the $\bar{\nu}$ sample at lower energies (See figure 6).

The large instantaneous event rate at the Tevatron will necessitate the running of our experiment in the slow spill or multi-ping extraction mode unless the detector is upgraded with drift chambers and buffered ADC's. During E616, most neutrino running was done using slow spill and, at that time, techniques were developed to minimize cosmic ray triggers, monitor the secondary beam flux, etc. For the early running of the Tevatron, slow spill extraction would be easiest to implement and probably adequate, but for further runs, the multi-ping method would be desirable if a detector upgrade is not implemented.

During the summer 1979 run of E616, we collected about 150,000 events with 1×10^{19} protons on target in six calendar months. As an indication of statistical precision, we combine the above data sample with a comparable (6 month) run at the Tevatron. This new run is assumed to be mostly at a beam setting of 600 GeV with 1.7×10^{18} protons equally split between neutrinos and antineutrinos. The expected number of events is shown in Table 1 and the Q^2 range is given in Figure 11; in subsequent sections, we investigate the precision of $F_2(x,Q^2)$, $F_L(x,Q^2)$, and $F_3(x,Q^2)$ measurements with this sample.

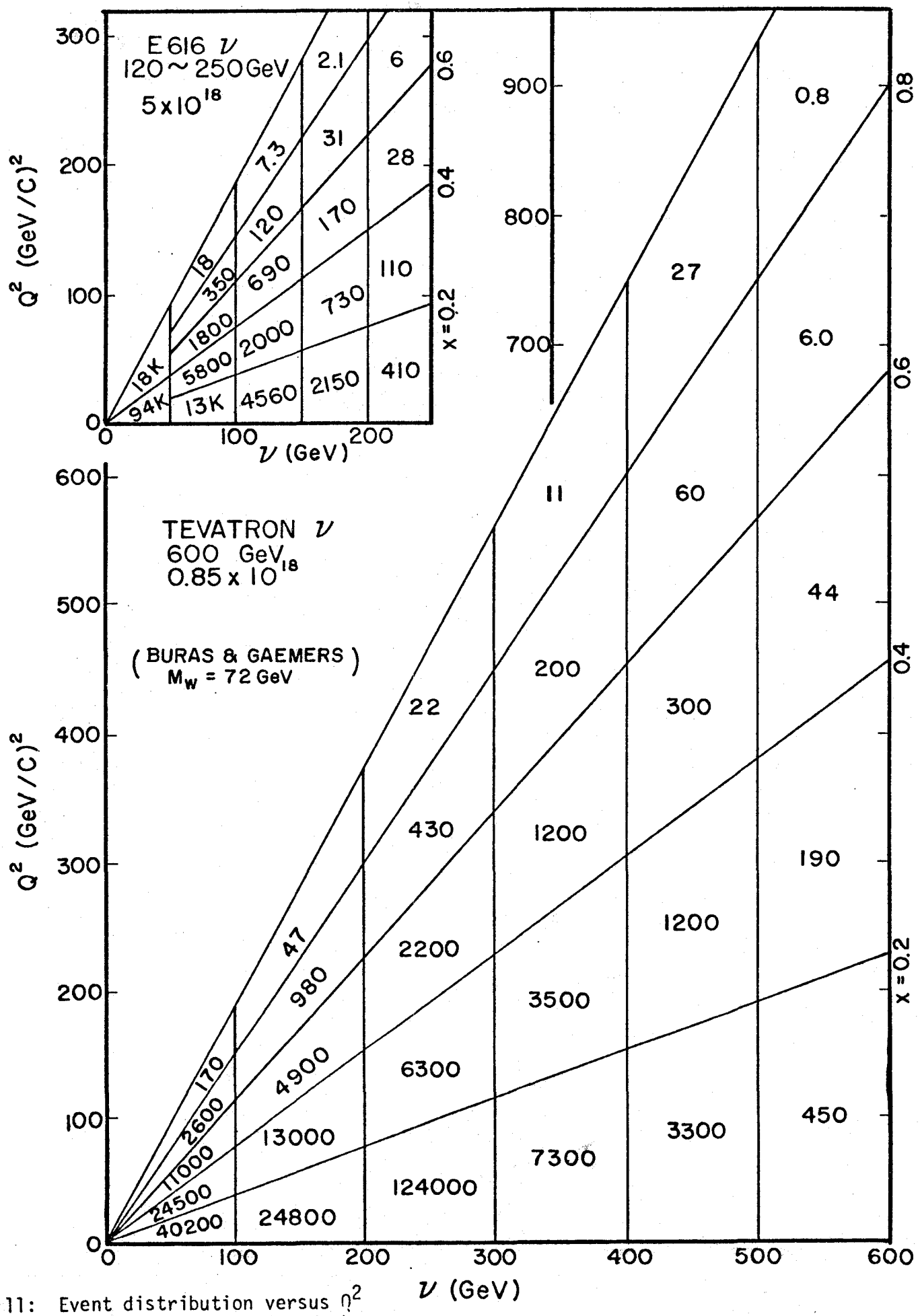

Figure 11: Event distribution versus Q^2 and ν comparing E616 and the Tevatron

	Beam Setting	ν_K energy range	ν_π energy range	Positive running Protons	Positive running $\frac{\nu_\pi}{\nu_K}$ Events	Negative running Protons	Negative running $\frac{\bar{\nu}_\pi}{\bar{\nu}_K}$ Events
E616	250 GeV	170-240 GeV	20-110	3×10^{18}	22,500	3×10^{18}	3,750
					25,500		825
	200 GeV	150-190 GeV	20-88	1×10^{18}	15,000	1×10^{18}	2,950
					10,500		600
	165 GeV	135-160 GeV	23-71	$.5 \times 10^{18}$	12,000	$.5 \times 10^{18}$	3,250
					5,500		500
	140 GeV	118-135 GeV	26-60	$.3 \times 10^{18}$	9,000	$.3 \times 10^{18}$	2,250
					3,150		345
	120 GeV	105-115 GeV	27-51	$.1 \times 10^{18}$	9,000	$.1 \times 10^{18}$	1,700
					2,000		210
Tevatron	600 GeV	120-570 GeV	20-251	$.85 \times 10^{18}$	42,500	$.85 \times 10^{18}$	5,100
					119,000		2,125
	250 GeV	170-240 GeV	20-110	———	———	$.13 \times 10^{18}$	6,500
							1,950
	200 GeV	150-190 GeV	20-88	———	———	$.13 \times 10^{18}$	6,500
							1,560
				TOTAL	275,650		40,115

TABLE 1: Expected Event Sample for Tevatron Data Combined with E616

IV. Measurements of $xF_3(x,Q^2)$ and R

The difference of the neutrino and antineutrino cross section yields a measurement of the xF_3 structure function (see Section I). Figure 12 shows the statistical precision of this measurement with the data of E616 only, and with the combined sample from Table 1. The combined sample

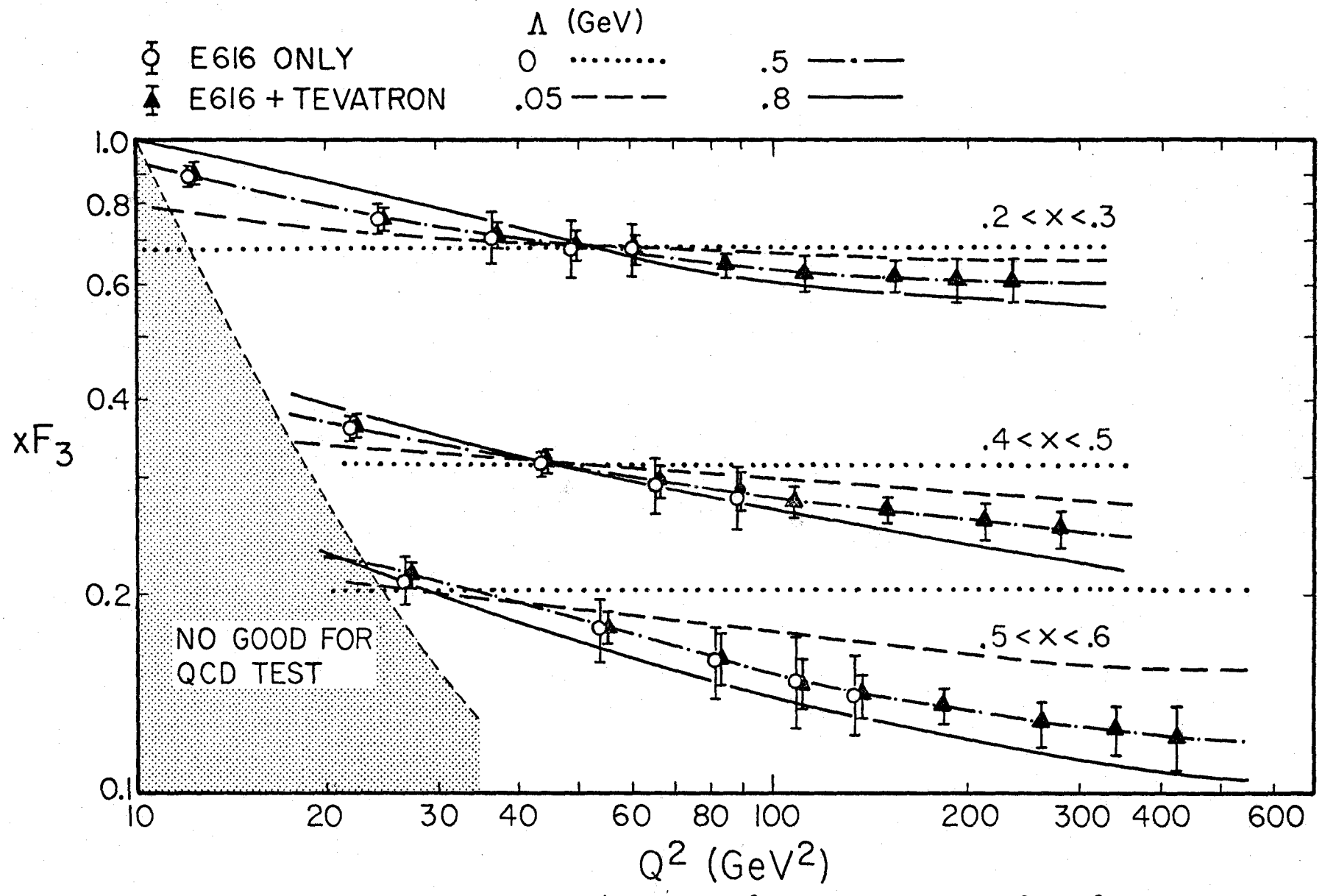

Figure 12: Expected errors for measurements of xF_3 as a function of x and Q^2 for E616 only (open circles) and the combined data of Table I (solid triangles). Also shown are asymtotic QCD predictions of the Q^2 behavior with four values of Λ. The shaded region on the left has large contributions from $1/Q^2$ terms and is unsuitable for comparing with the asymtotic theory.

yields measurements over a much greater range of Q^2, which is extremely important for testing theoretical predictions. Also shown in the figure are theoretical curves from QCD models using various values of Λ, the QCD energy scale parameter. In contrast to other QCD calculations, the theoretical uncertainties for the xF_3 predictions are small; for this calculation, the gluon distributions do not enter (see section I) and the higher order corrections are believed to be small. The strong coupling constant, α_s, is given to first order in terms of Λ as

$$\alpha_s(Q^2) = \frac{12\pi}{25\ \ell n(Q^2/\Lambda^2)}.$$

To first order, a measurement of Λ is also a measure of α_s.

The predicted Q^2 variation for xF_3 is mainly logarithmic and, therefore, a large range of Q^2 is needed for a precise measurement of Λ. The Q^2 range covered by E616 is from 20 - 100 GeV^2, and for the combined data is 20 - 400 GeV^2; the lever arm in $\ell n\ Q^2$ is extended by a factor of two with the Tevatron data. This larger range for the Tevatron is in turn reflected in a far better determination of Λ and α_s. As shown in Table 2 and Figure 13 the error in Λ is reduced by a factor of three for Λ_{input} = .5 GeV. If exact scaling (no Q^2 variation and Λ = 0) is the underlying behavior, E616 will be able to limit Λ to below .3 GeV. The added Tevatron data would lower this limit to .001. The general conclusions of this study are: 1) The E616 data will qualitatively show if QCD scaling violations exist at high Q^2 (> 20 GeV^2). 2) The combined E616, Tevatron sample will be able to measure the scale violation parameter Λ in a quantitative way and allow one to make predictions for other reactions.

At the higher Q^2 values available at the Tevatron, changes in the structure function due to the weak vector boson propagator will be observable if M_W < 100 GeV. The experimental problem is to untangle the propagator

Data Sample	Λ (GeV) Input	Λ (GeV) "Measured"	α_s (50 GeV^2) "Measured"
E616	.5	.70 ± .26	.32 ± .06
E616 + Tevatron	.5	.50 ± .08	.285 ± .015
E616	0	< .3	< .24
E616 + Tevatron	0	< .001	< .08

TABLE 2: Expected statistical errors for measurements of Λ and α_s. The values are obtained by fitting Monte Carlo data generated with the given input Λ's.

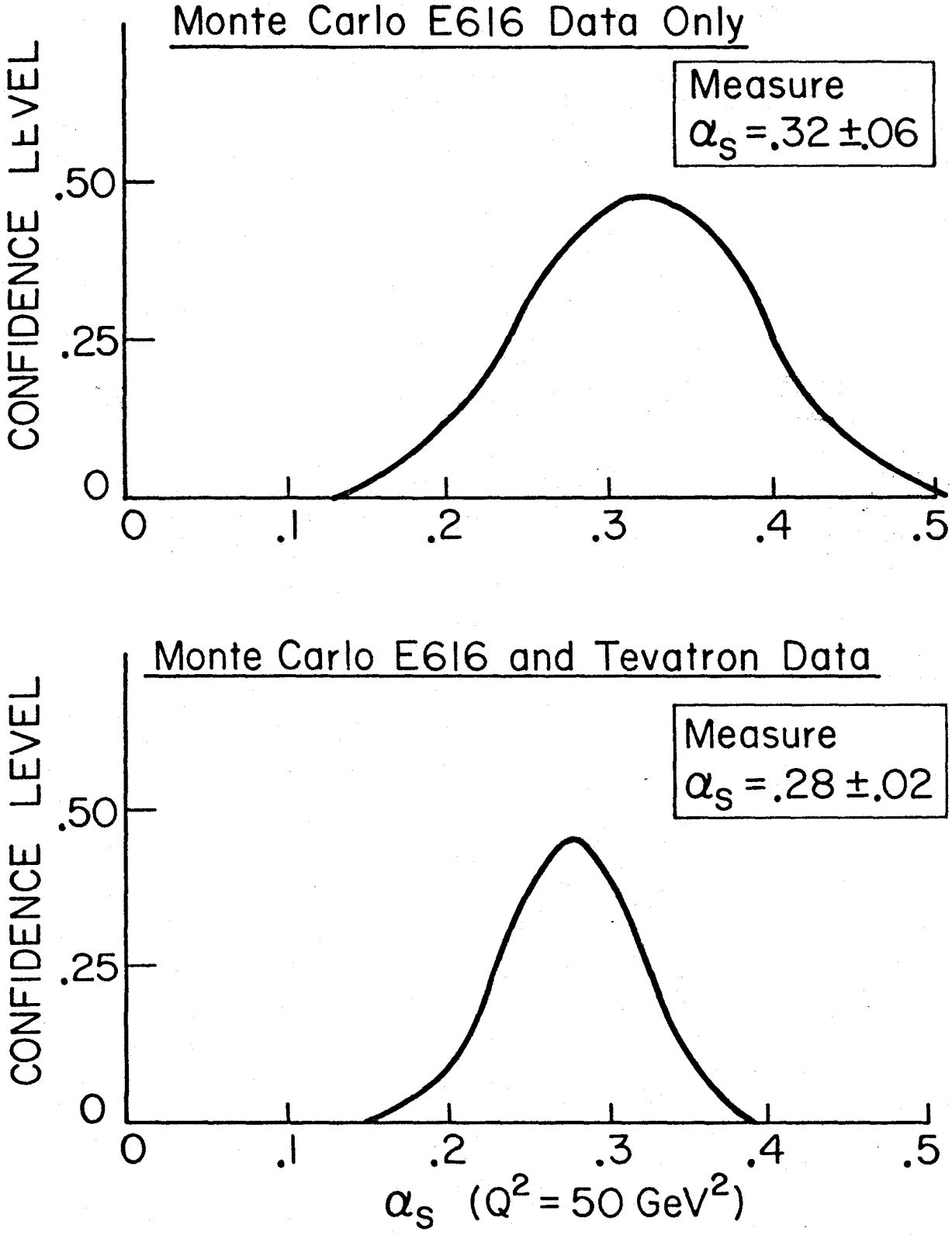

Figure 13: Expected errors for the measurement of the quark-gluon coupling constant (α_s). The value of α_s is obtained by fitting the changes in the xF_3 structure function with Q^2. (The Monte Carlo data was generated with α_s (50 GeV^2) = .28).

behavior from QCD effects. At x = .65, the xF_3 structure function drops, due to QCD effects, logarithmically by 40% over the Q^2 range of 30 - 500 GeV^2 whereas the W propagator term gives a negligible change below 100 GeV^2 and a drop of 20% from 100 - 500 GeV^2. The ability to separate the propagator and QCD behavior depends somewhat on the magnitude of the QCD scaling violation and the weak boson mass, but with the large lever arm in Q^2 available with the combined data set, separating these two effects might be possible.

Extracting $R(x,Q^2)$ (or $F_L(x,Q^2)$) from measurements of neutrino and antineutrino cross sections is difficult but of major theoretical interest. In this case, QCD predicts both the magnitude and change with Q^2. At small x, the theory predicts, for R, large values which have a $1/\ell nQ^2$ behavior; and at large x, R should be close to zero (See Figure 12). In Figure 13 we show the expected errors with the combined data sample of Table 1. The magnitude of R is directly related to α_s (Q^2), and the observed value must be consistent with the value of α_s (Q^2) measured by xF_3. "Higher twist" effects (such as scattering from diquarks in the nucleon) can induce an extra M^2/Q^2 part to the prediction, but these terms fall off rapidly with Q^2. The added Q^2 range provided by the Tevatron data allows an important confrontation between experiment and asymptotic QCD in a region where these extra M^2/Q^2 terms are negligible. (A large value of R at large x and high Q^2 would be contrary to predictions from the current theory and would indicate that our understanding of nucleon structure is wrong even in the asymptotic regime.)

V. Conclusions and Requests

Neutrino-nucleon collisions at high Q^2 provide the most feasible and definitive method for extracting the nucleon inelastic structure functions, whose behavior with Q^2 is predicted by Quantum Chromo-Dynamics. The

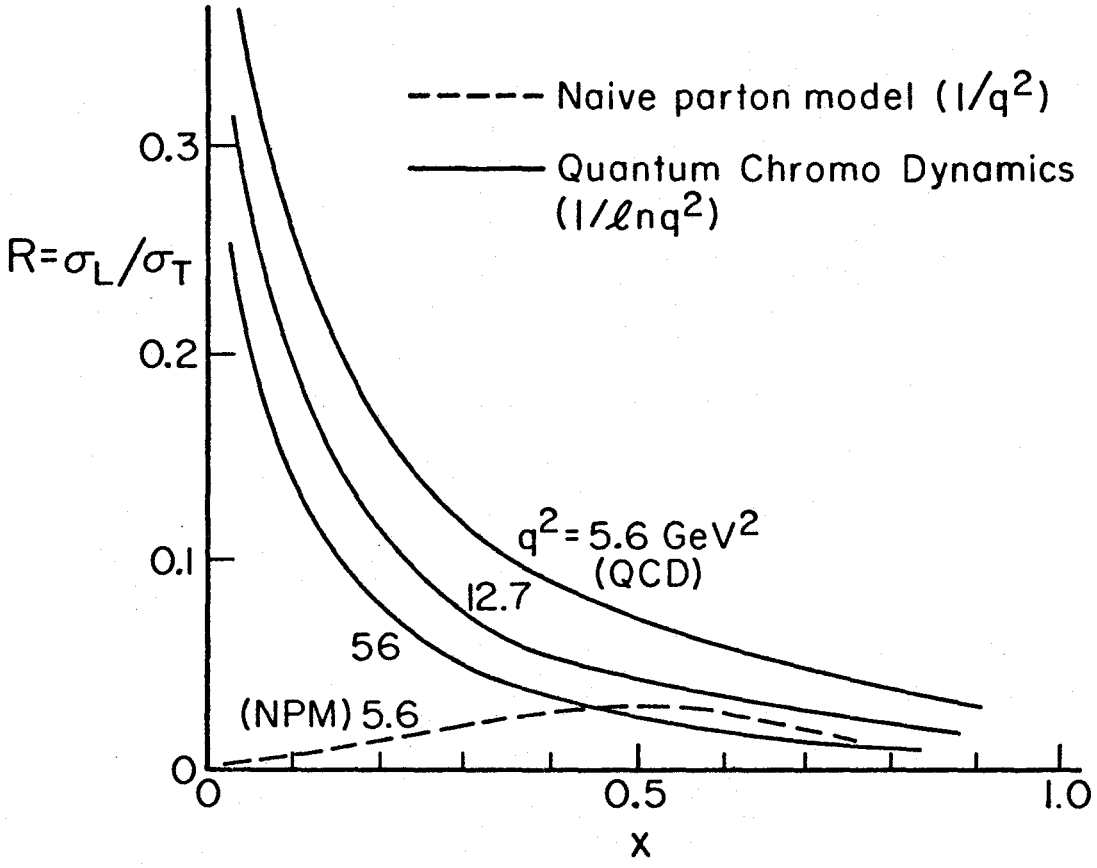

Figure 14: Theoretical prediction for $R = \sigma_L/\sigma_T$

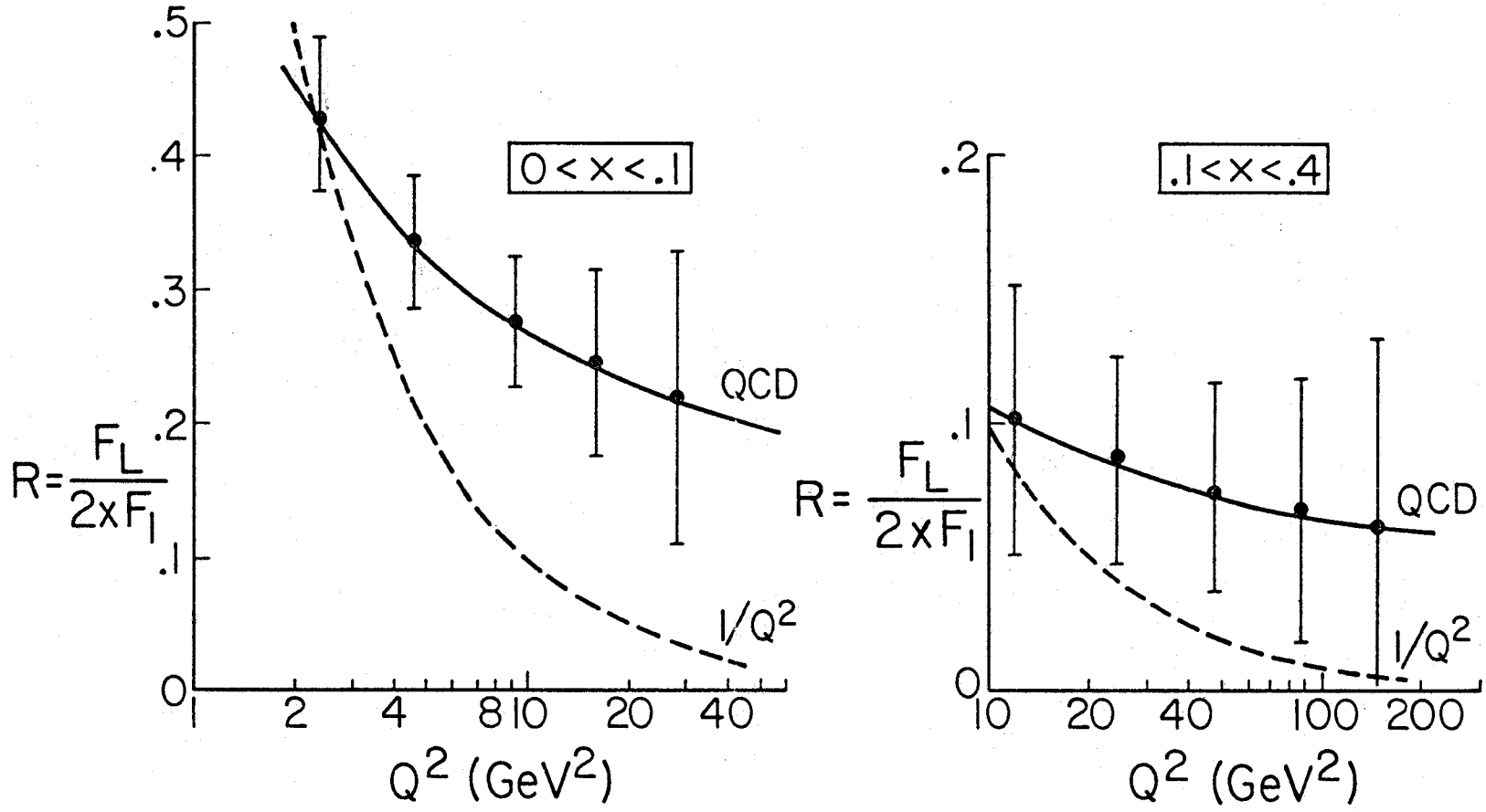

Figure 15: The errors in R for two x bins vs. Q^2 using the combined data sample of Table I. The solid curve is a QCD prediction with Λ = .5 GeV and the dashed curve is a $1/Q^2$ behavior.

existing Lab E detector has just completed a six month run, taking ~ 150,000 events, which will determine whether high Q^2 logarithmic behavior occurs. However, we conclude, a definitive measurement of the quark-gluon coupling constant (α_s) requires either a much greater statistical and systematic accuracy or an extension of the Q^2 range. The former can only occur with several years of constant 400 GeV data-taking; the latter, an extension by a factor of 2 in the useful log Q^2 range, will occur with the first extracted beam at the Tevatron. We anticipate that a 6-month run at the Tevatron, combined with E-616 data, will provide a measurement of α_s which is better than available from our E-616 data alone, by a factor of 3 to 4. Conversely, the use of our E-616 data taken in the same apparatus at the lower end of the available Q^2 range makes the potential Tevatron data enormously more powerful.

We are confident that the experimentally-verified resolutions of the Lab E detector are well-matched to QCD tests in the present energy regime, and are more than adequate for the higher Tevatron energies. The event rates per calendar time will be approximately equal to those presently found. There is no doubt that the verification of asymptotic QCD requires Tevatron neutrino data combined with E-616 data.

We request, therefore, a run with the Lab E apparatus as early as possible with 1000 GeV protons from the Tevatron, for a total illumination of 2×10^{18} protons. This run will utilize the new dichromatic beam tuned to the settings discussed in Table 1 and the E-616 flux monitoring equipment described in Appendix A.

The configuration of Lab E for this run will depend on several factors that will be clarified over the next year. These factors include:

(1) The physics in the present energy and Q^2 region as determined from our E-616 data;

(2) The additional physics potential of any contemplated detector upgrade

(see Appendix A)

(3) The detailed technical and financial questions associated with an upgrade;

(4) The extraction modes (e.g. multi-ping extraction, slow spill, etc.) available in the early and longer-term Tevatron.

Item (1) is being pursued with speed and care. We anticipate early results over this summer on neutrino and anti-neutrino cross-sections, multi-muons, and neutral currents, as well as preliminary results on the xF_3 structure function. Results on all 3 structure functions should be available within a calendar year. Items (2) and (3) are being pursued with Monte Carlo calculations and prototype drift-chamber modules. We specifically request that the laboratory provide some evaluation of item (4) over the next year.

We emphasize that an early run at the Tevatron with our present equipment would result in answers to important scientific questions. Indeed, any upgrade will be motivated more by the anticipated long-term use of the Lab E detector in the neutrino area. Hence, our request for early Tevatron running is specific and definite.

References

1. A.Bodek, Ph.D. Thesis, MIT LNS Report No. COO-3069-116 (1972); J.D.Mestayer, Ph.D.Thesis, SLAC Report No. 214 (1978) and references therein.

2. G.Altarelli and G.Parisi, Nucl. Phys. B126, 298 (1977).

3. J.G.H.deGroot et al., Phys. Letters 82B, 456 (1979); A.J.Buras and K.J.F.Gaemers, Nucl. Phys. B132, 249 (1978).

4. R.D.Field, CALT-68-739 (1979).

APPENDICES

APPENDIX A: Amplitude Readout Drift Chambers

This appendix discusses the feasibility of instrumenting the present Lab E neutrino detector with amplitude readout drift chambers to measure the energy flow of the hadronic shower.

In itself, the conversion of the present Lab E neutrino detector from spark chambers to drift chambers with the usual TDC readout system has several nice advantages. Drift chambers would give the detector multi-trigger capability during the 1 millisecond spill. They also offer the potential for better precision in measuring muon trajectories. Drift chambers are reliable and should give fewer maintenance problems than the currently used spark chambers.

If the drift chamber electronics include a pulse amplitude readout system in addition to conventional time digitization, there is the possibility that the energy flow of the hadronic shower can be measured. This would yield another variable, θ_H, in the neutrino interactions allowing one to get better precision on the quantity x in charged current interactions. In neutral current interactions, x distributions would be measurable, and there exists the possibility of a tau neutrino search using the missing transverse momentum technique[1].

As an upgrade of the present Lab E detector, measurement of this hadronic energy flow would be with an iron target having fairly high density. Previous neutrino detectors that measured energy flow have used less dense material such as aluminum, marble[2], sand and shot[3], or scintillator. The simplest energy flow detector can be envisioned as a target consisting of a collection of slabs between which one inserts a probe to measure the properties of the shower. Figure A1 shows such a

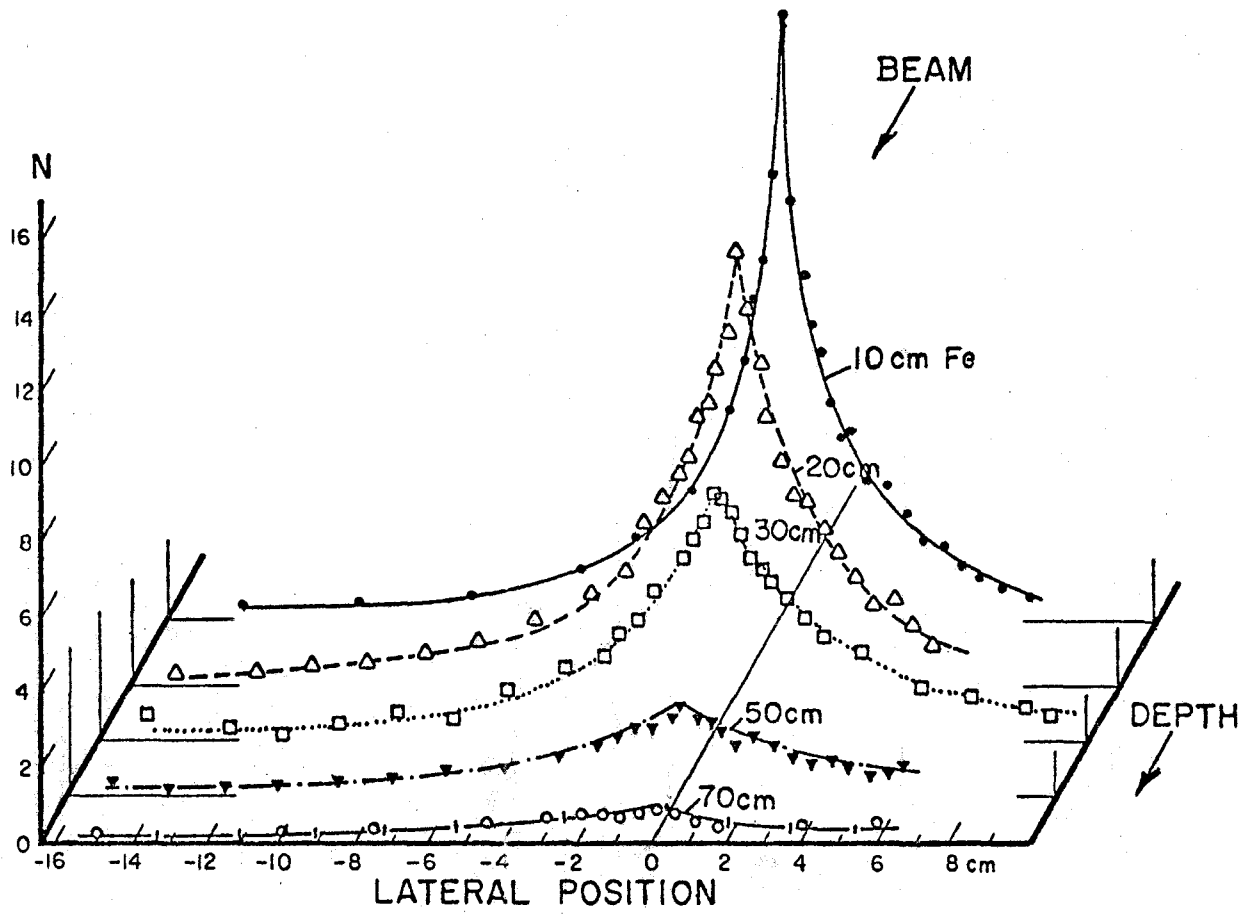

Figure A1: Lateral energy distributions of showers induced by 10 GeV/c π^-, measured at 10, 20, 30, 50, and 70 cm depth in Fe

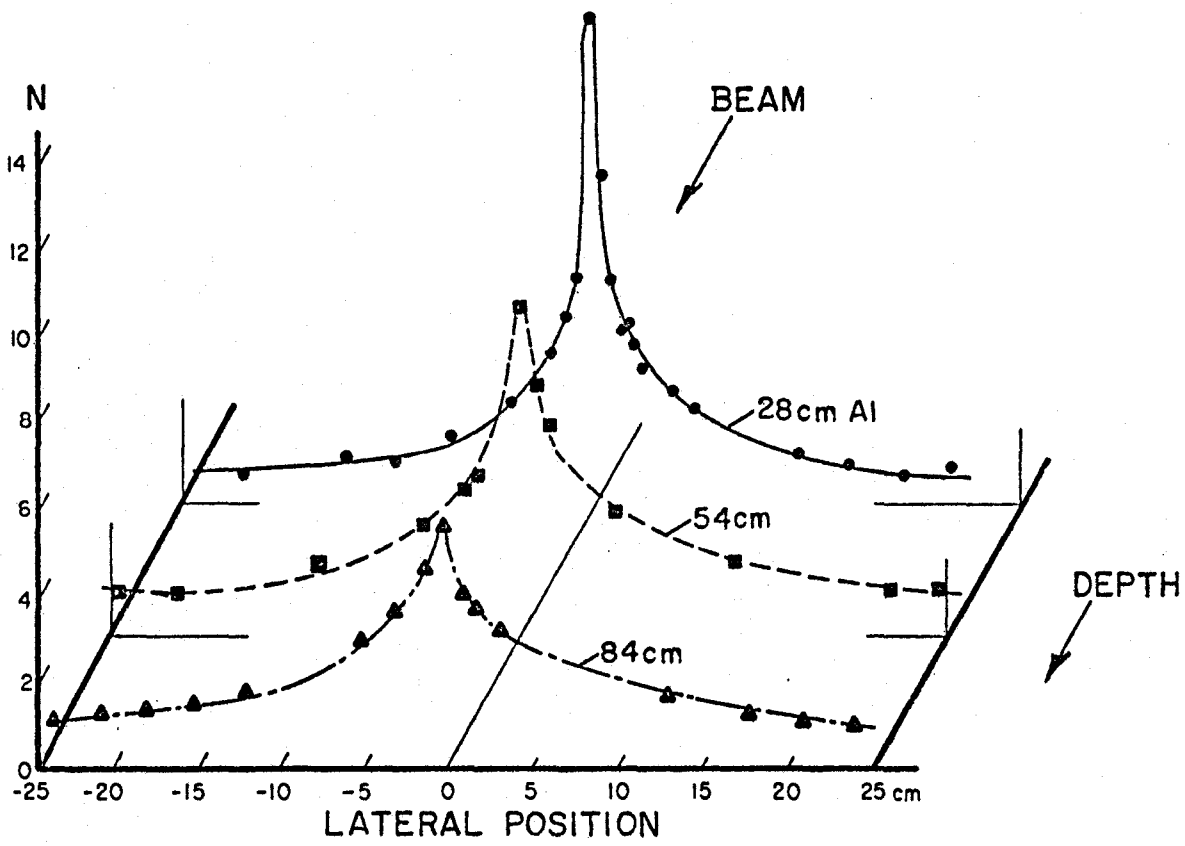

Figure A2: Lateral energy distributions of showers induced by 10 GeV/c protons, measured at 28, 56, and 84 cm depth in Al.

measurement[4] of 10 GeV/c π^- induced shower in a stack of iron plates. Figure A2 shows the same measurement in aluminum. The cusplike behavior near the beam axis is due to surviving beam particles and to elastic and inelastic diffraction scattering. The long tails are due to secondary, tertiary, etc. interactions. The direction of energy flow is calculated by fitting each lateral distribution to determine its center and deviation, then connecting these measurements back to the origin to determine the shower direction. The shower in aluminum is physically larger than in iron. However, when the two measurements are scaled with density, the showers are surprisingly similar. Figure A3 shows how the shower width (full width at half maximum) develops as a function of absorber depth expressed in a scale of length x density. The main difference between iron and aluminun targets is the granularity of the sampling, and therefore, iron requires a more frequent sampling in real space to give the same precision.

Another calculation[2] compares the precision of hadron energy flow in iron to aluminum as a function of sampling step, both in longitudinal and transverse dimensions. Figure A4 shows the calculated angular resolution of a hadronic shower induced by 100 GeV/c particles as a function of sampling step in the longitudinal direction, expressed in terms of grams/cm^2. Both aluminum and iron behave similarly. In Figure A5 the angular resolution is calculated as a function of sampling width in terms of gram/cm^2. This figure clarifies the reason that less dense materials are chosen to measure energy flow. In iron it is necessary to have a sampling width of less than 1cm to obtain comparable resolution with aluminum using a 3cm sampling width.

In considering improvements of the Lab E detector, we conclude that:

1. If adequately instrumented, an iron target can measure hadronic energy flow as well as an aluminun target.
2. The transverse dimension of the sampling is more critical than

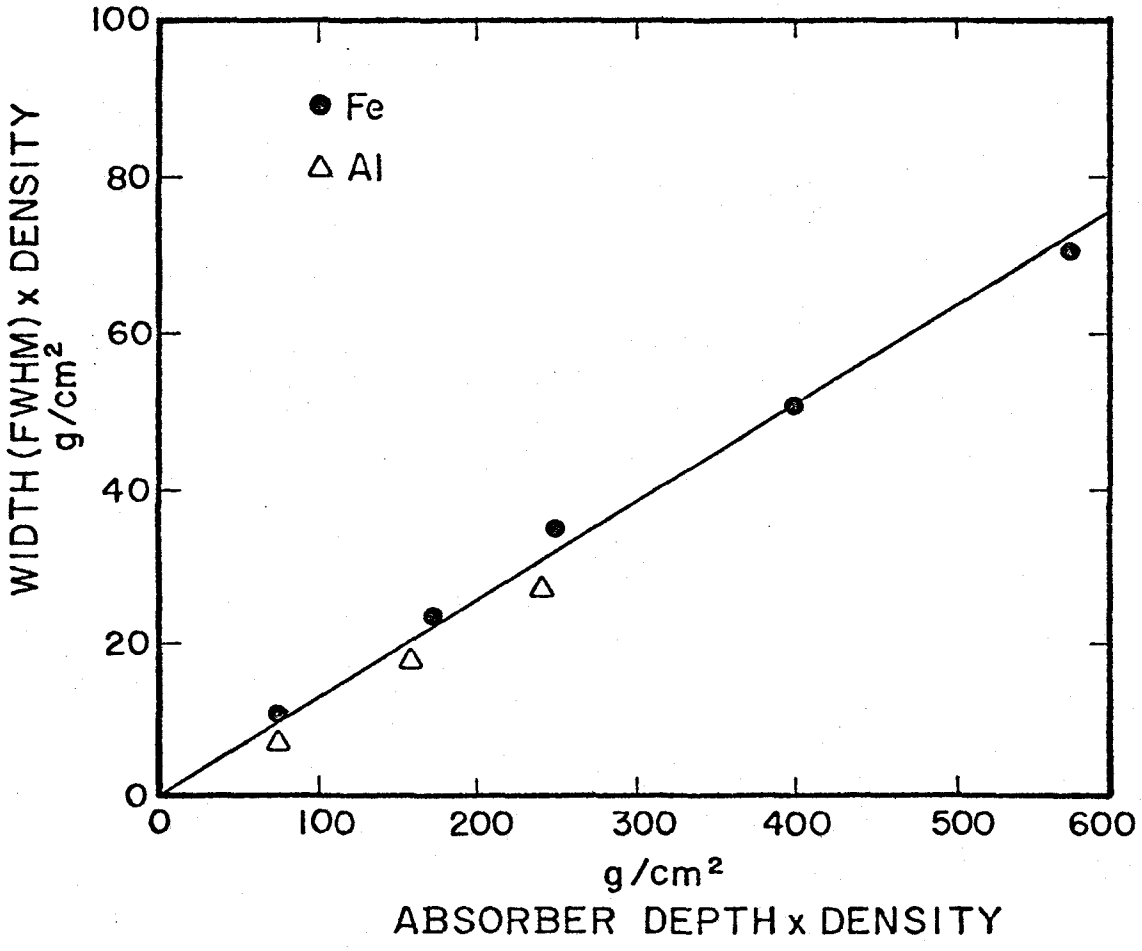

Figure A3: Shower width (fwhm) as a function of depth in absorber measured in units of length x density. There is approximate scaling with the density.

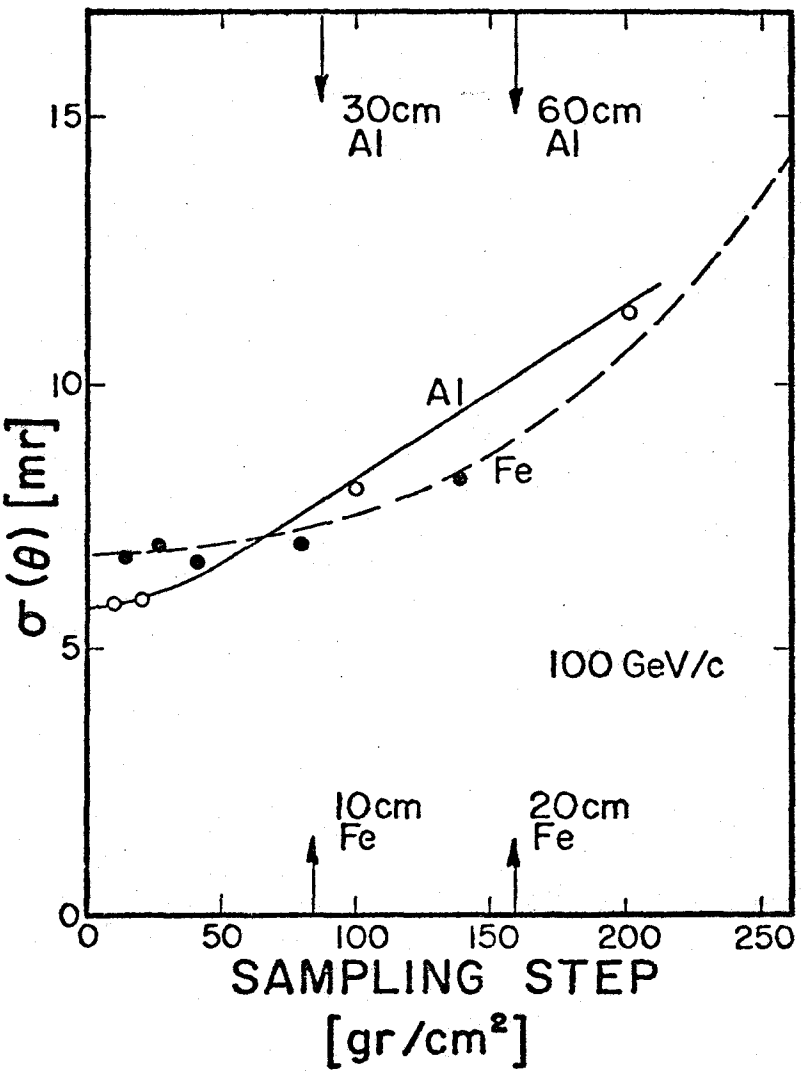

Figure A4: Resolution $\sigma(\theta_H)$ on the hadron shower direction for Fe and Al as a function of longitudinal sampling step expressed in units of density x sampling thickness for a 100 GeV/c hadron shower.

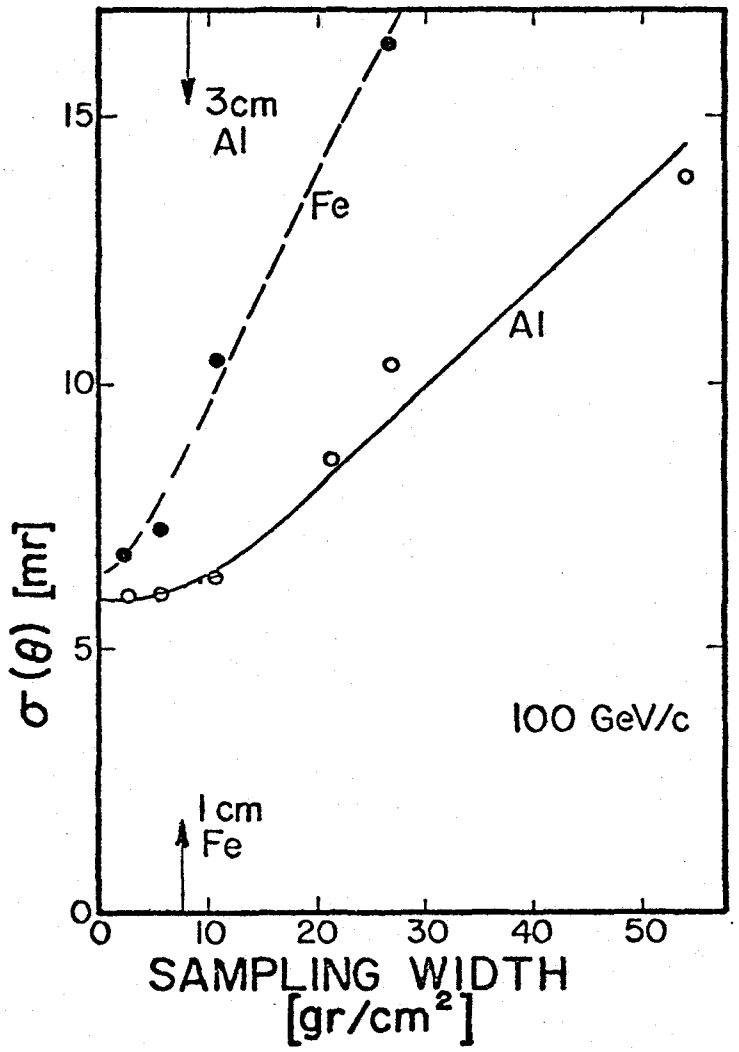

Figure A5: Resolution $\sigma(\theta_H)$ of the hadron shower direction for Fe and Al (assuming the apex position is known) as a function of the width of the sampling elements expressed in units of density x width for a 100 GeV/c shower.

the longitudinal sampling (for iron this should be as small as 5mm).

3. In order to achieve this small transverse sampling size, we propose to use amplitude readout drift chambers similar to those used in JADE[5] and UA-1[6] except that we would apply it on a shower in a calorimeter instead of individual particles.

Calculations and measurements, carried out at other energies, indicate the energy dependence of this angular resolution is of the form[7], [8]:

$$\sigma(\theta_x) = a + \frac{b}{E_H}$$

where a is 3.5 to 5.5 mrad and b is 350 to 450 mrad-GeV. For purpose of calculation we assume:

$$\sigma(\theta_x) = 4.5 + \frac{450}{E_H} \quad \text{for iron.}$$

A possible basic drift cell configuration is shown in Figure A6. A two-wire anode eliminates left-right ambiguities, and cathode strips shape the electric field to assure uniform drift velocity over the entire area. Using I-beams for structural reinforcement[9], crossed planes of these cells can be constructed thin enough to fit within the 3 inch gaps presently occupied by the spark chambers in the Lab E detector. The pulse shape[10] on the anode wire from a similar drift chamber measuring a single incident particle is shown in Figure A7. It is a well-behaved pulse 30-40 nsec wide with no afterpulses. A hadronic shower would manifest itself as a superposition of many such pulses in both space and time. If the current collected by the anode wire were integrated for 60 nsec, the effective sampling width would be 3mm.

A block diagram of the proposed electronics of a single channel is shown in Figure A8. It is a charge and time digitizer using a flash ADC[11]. A 16 MHz clock advances the address counter and causes the flash

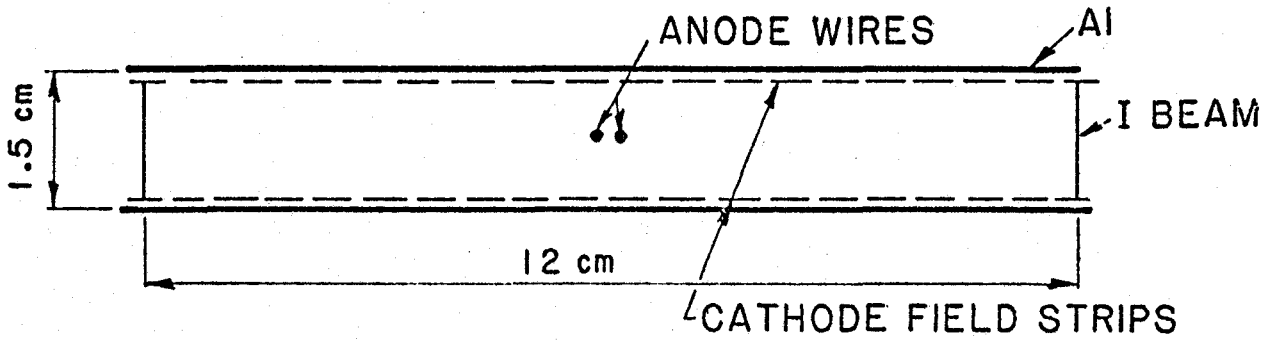

BASIC DRIFT CELL

Figure A6: Schematic diagram of a possible drift cell structure with two-wire anode, cathode field strips, and I-beam reinforcements.

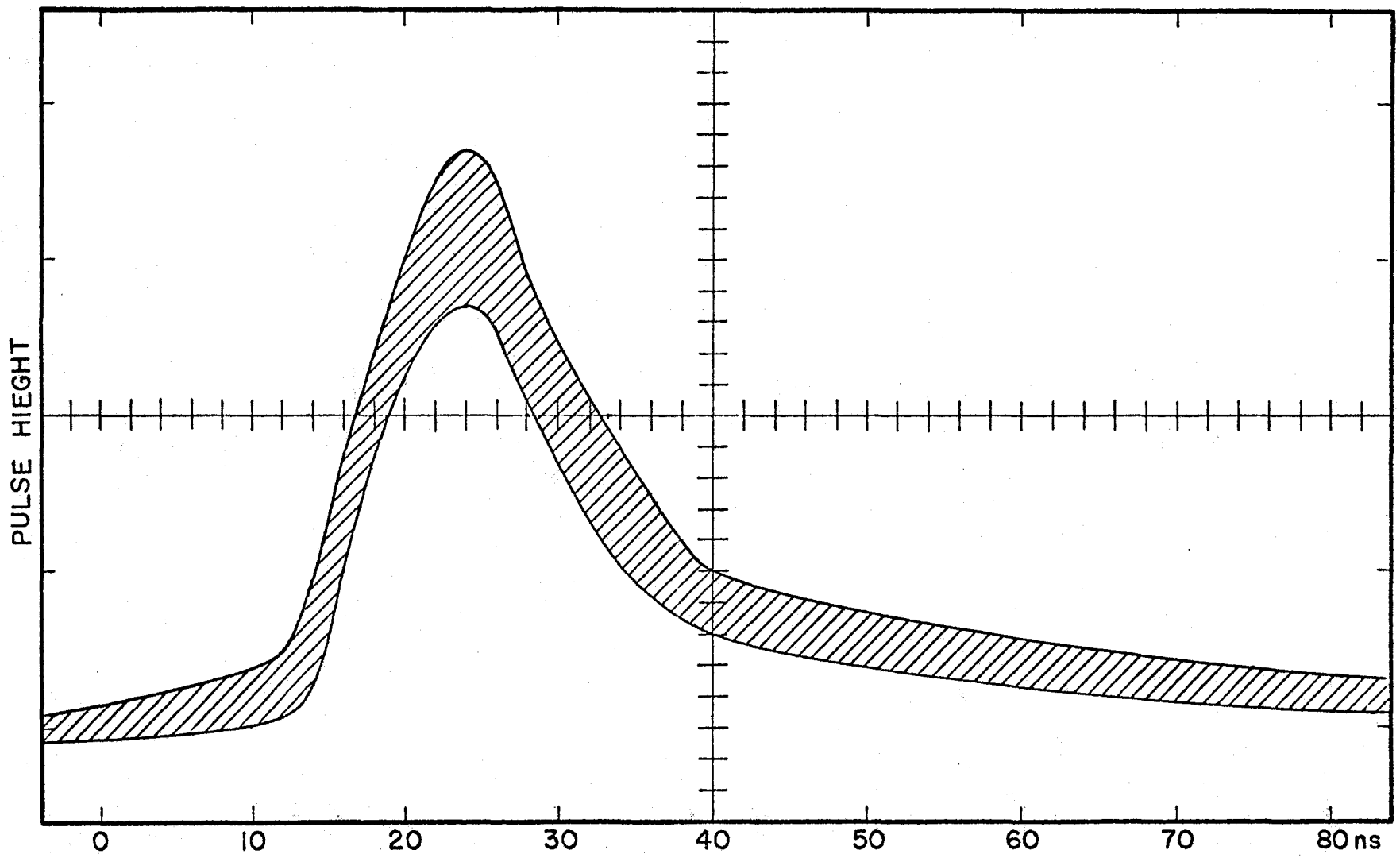

Figure A7: Expected anode current pulse from a single particle incident on a drift chamber with cathode field strips.

BLOCK DIAGRAM OF ELECTRONICS

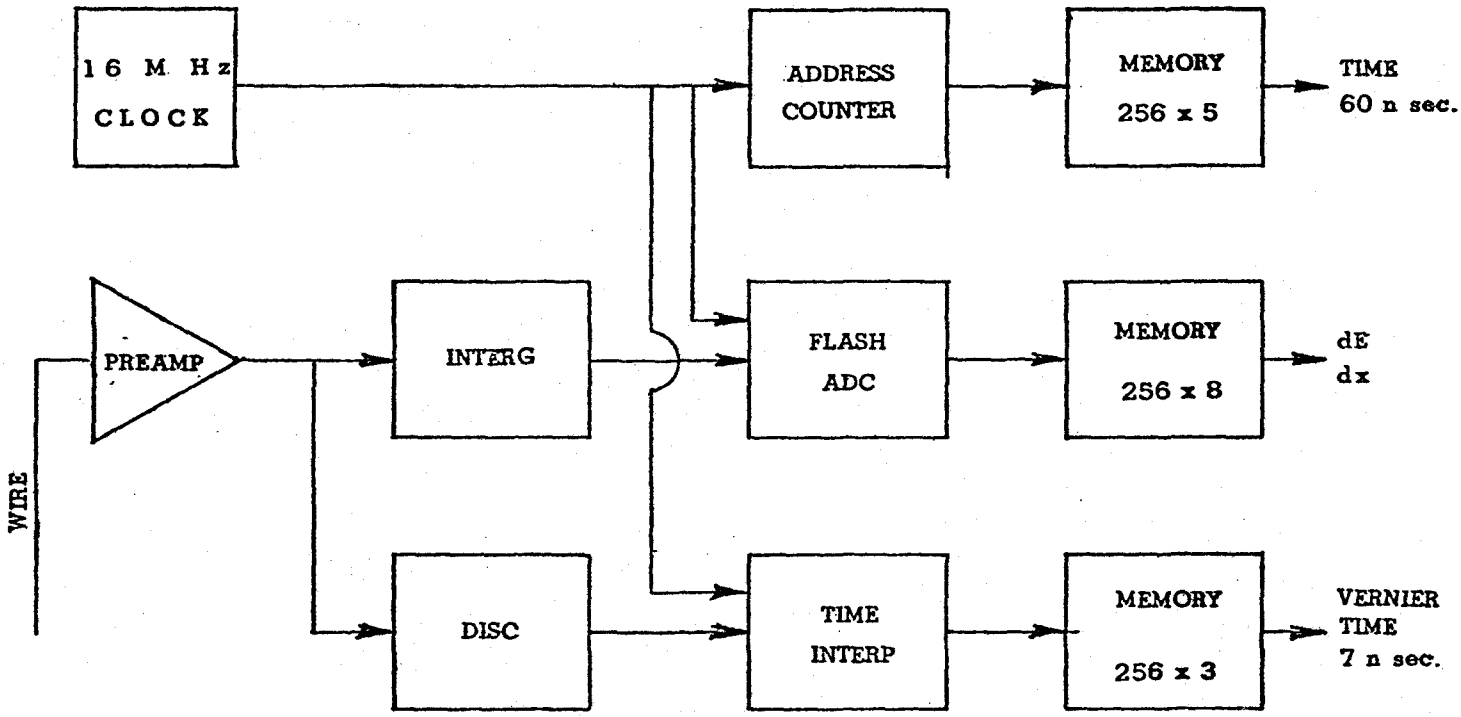

Figure A8: Block diagram of a charge and time digitizer with flash ADC's.

ADC to digitize the charge collected during the previous 60 nsec. Parallel to the integrator-flash ADC system is a conventional time-digitizing system for a drift chamber with a spatial resolution of 200μ for locating the muon track. Stored in the random access memory (RAM) for every 60-nsec-time-slice are three numbers: (1) the cycle count which gives 3mm spatial resolution, (2) the charge collected for hadronic dE/dx, and (3) the vernier time for the first particle firing the discriminator within the cycle period. The proposed 6cm drift length of the cell is a 1.2 μsec drift-time interval which, at a 16 MHz digitizing rate, equals 20 bins of 3mm width. The RAM's can store up to 12 triggers with no deadtime during the beam spill. After the beam spill is finished, the contents of the RAM's would be pre-analyzed by a microprocessor and transferred to the data acquisition computer.

A flash ADC is a fully parallel multi-threshold A/D converter designed for TV applications. A single chip contains 255 comparators, and some can be programmed with a nonlinear response to increase their dynamic range.

Such a system as proposed in Figure A8 would presently cost approximately $200/channel. However, the cost/channel two years from now is projected to be $125-$150. To project this cost/channel number into a cost estimate for the upgrade of the Lab E neutrino detector is extremely difficult at this time, but is probably in the $1M to $2M range. This involves 42 chambers in the target requiring approximately 2100 channels of amplitude readout electronics and a smaller number of chambers in the toroids using conventional TDC's.

There are further questions to be worked out relating to optimization of chamber dimensions, the dynamic range to be covered, and the resolution effects of low energy particles and ion loading in a gas counter. A literature search reveals no absolute barriers to success; but these questions are best

answered with a small test detector. We propose to prototype a few channels of the electronics this summer to settle parameters. We would then want to instrument and run a small test calorimeter of 400 channels next year. If everything works out as we expect and the PAC approves, full scale production could begin and the system would be operational by the fall of 1983.

TABLE I: Costs of Test System

Initial development costs	10K
400 channels @ $200 ea.	80K
16 - 1m x 1m drift chambers	10K
	$100K

References for Appendix A

1. "Signals for Tau Neutrino Interactions in a Beam Dump Experiment", H.Albright and R.E.Shrock, Phys. Let. 84B, 123 (1979); C.H.Albright, R.E.Shrock, and J.Smith, Int. Conf. Neutrino '79, Bergen, 1979.
2. "Proposal for a Study of High Energy Neutrino Interactions Using Counter Techniques", K.Winter, et. al., CERN Proposal SPSC/p. 49, 1975.
3. "The Construction and Performance of Large Flash Chambers", F.E.Taylor, et. al., IEEE, NS-27, 30 (1980).
4. "Measurements of Energy Flow Distributions of 10 GeV/c Hadronic Showers in Iron and in Aluminum", B.Friend, et. al., NIM 136, 505 (1976).
5. "Drift Chamber Electronics for Time and Pulse Height Measurements with Multiple Hit Capacity", W.Farr and J.Heintze, NIM 156, 301 (1976).
6. "A 4π Solid Angle Detector for the SPS Used as a Proton-Antiproton Collider at a Center of Mass Energy of 540 GeV, C.Rubbia, et. al., CERN Proposal SPSC/p. 92, 1978.
7. "Study of the Use of Hadron Calorimeters for the Measurement of the Momentum of Hadron Showers", A.Barovcelli, Calorimetry Workshop Proceedings, Fermilab, 1975.
8. "A Monte Carlo Simulation of an Actual Segmented Calorimeter; A Study of Calorimeter Performance and High Energies", M.S.Goodman, et. al., IEEE, NS-27, 46 (1980).
9. "Very Large Proportional Drift Chambers with High Spatial and Time Resolutions", D.C.Cheng, et. al., NIM, 117 157 (1974).
10. "Drift Chambers and Recent Developments", J.Heintze, NIM, 156, 227 (1978).
11. "New Developments in Time and Pulse Height Digitizers", B.Hallgren and H.Verweij, IEEE Sci, NS-27, 333 (1980).

APPENDIX B: LAB E APPARATUS

(From FNAL Proposal 616)

The general layout of the apparatus located in Lab E is shown in Fig. B1. It consists of a 688 ton steel target with scintillation counters and position detectors interspersed to measure hadron energy and identify the trajectories of muons followed by a 404 ton instrumented toroidal magnet spectrometer which also serves as a magnetized target for neutrino interactions.

Target

The Lab E target-calorimeter consists of six modules mounted on wheeled carts. These modules move into the N5 hadron beam for calibration. Normally they reside on the N0 line for neutrino data running. As shown in Fig. B2, each target module contains 28 steel plates 10' by 10' by 2" which serve as a target and medium for hadron shower development, 14 calorimetry counters with a 10' by 10' active area to sample hadron shower development and record the presence of individual muons, and six magnetostrictive spark chambers with a 10' by 10' active area to localize the interaction vertex and trace muon trajectories through the apparatus.

Target Counters

The 10' by 10' counter planes are plexiglas tanks containing a 1" thick layer of liquid scintillator mixed with mineral oil. Wavelength shifter bars on the four sides of each counter are viewed at the corners by RCA 6342A photomultiplier tubes. The four tubes on each plane are individually pulse height analyzed to provide hadron energy. For minimum ionizing particles the four

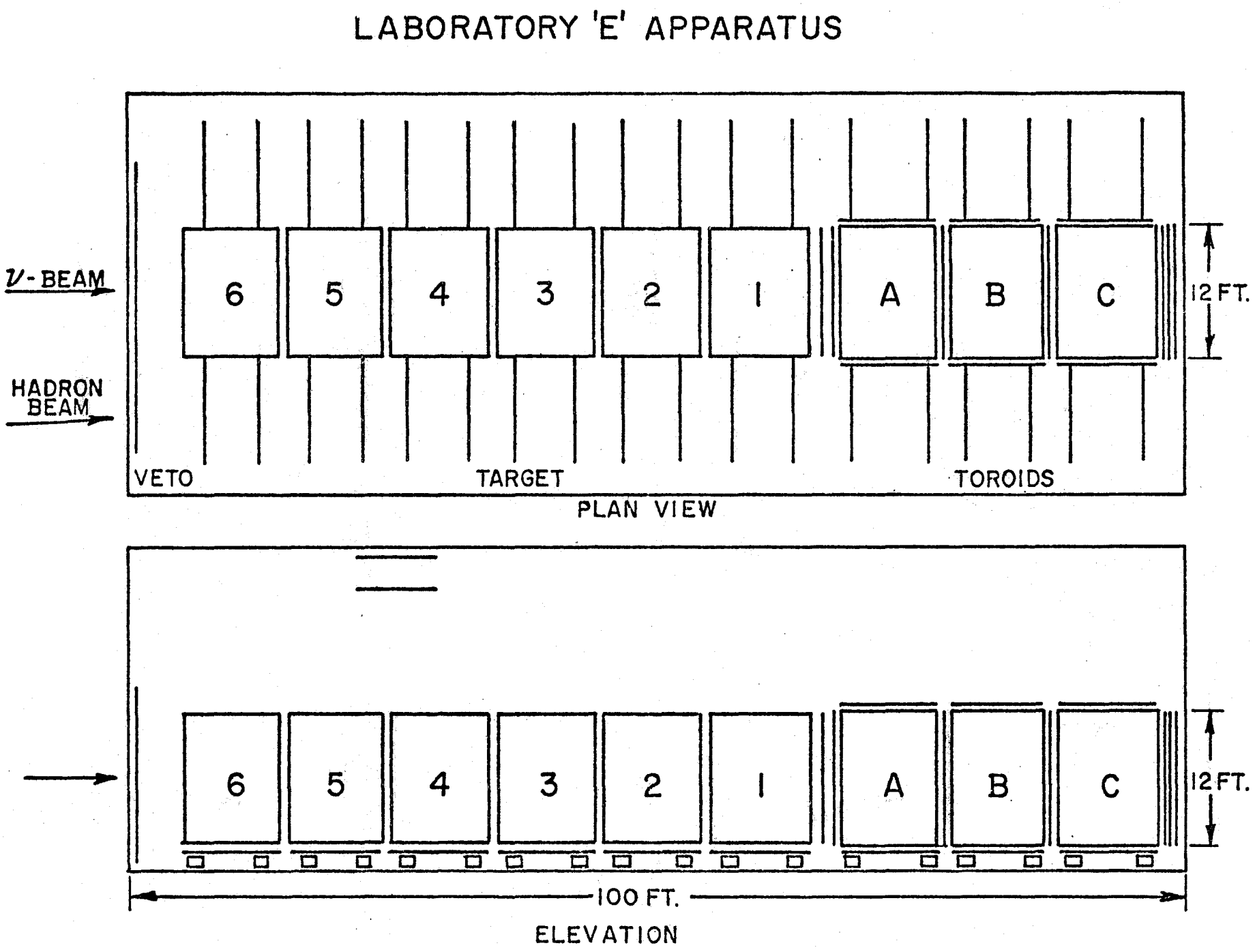

Figure B1
Lab E apparatus

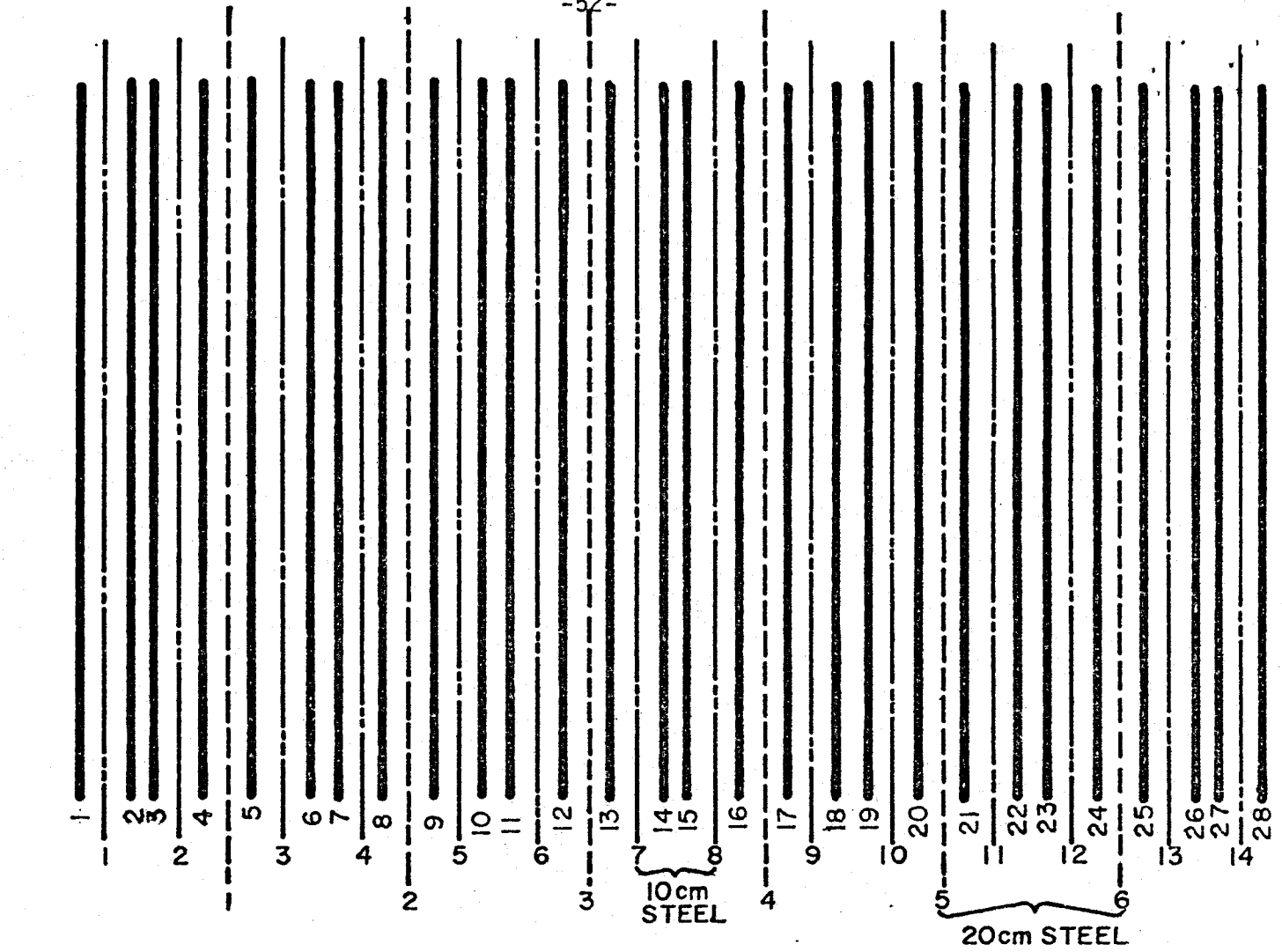

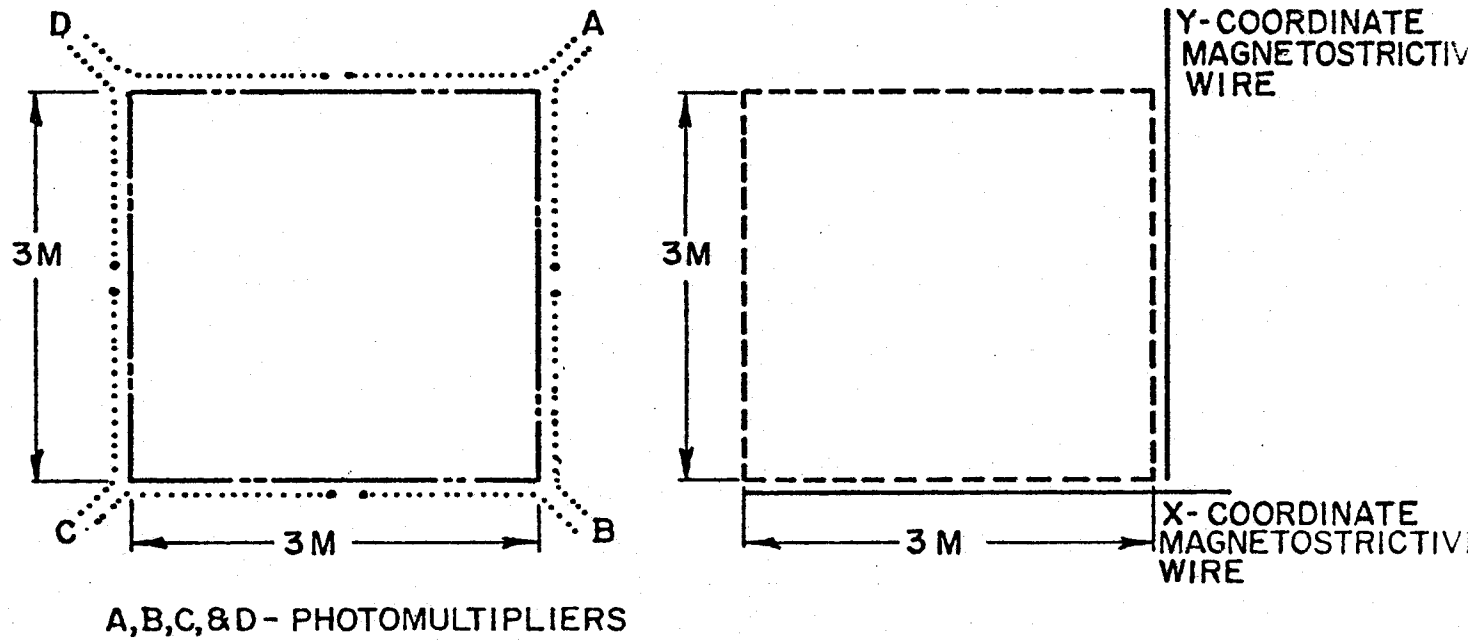

TARGET CART

Figure B2
Target Cart Counter Arrangement

PM's are amplified by 10 and summed. Typical response to a muon through the center of the counter is 16 photoelectrons. The stability and balance for the PM's on each plane are monitored and maintained by a light flasher system. Filtered light from a spark gap is piped via a light fiber to a white dot at the center of each counter. The white dot disperses the light and allows the gain and balance to be monitored on an interspill basis. Appendix D on Calorimetry discusses linearity and resolution of the counters as a function of energy.

Target Spark Chambers

The 10' by 10' spark chambers are made from two 1" thick Hexcel aluminum clad panels with mylar-backed wires bonded to the inside. The readout is magnetostrictive. Each magnetostrictive wand contains a X3 preamplifier powered by the same coaxial cable that connects it to the readout electronics. The electronics consists of a spark chamber interface module for pulse center finding and multitime digitizers to record clock counts for the x and y maglines. Each chamber is pulsed by a separate low impedance, high voltage pulser which applies a 5 kV pulse of duration 200 ns. The HV pulse is derived from switching energy stored on 24 parallel HV cables via a thyratron (E.E.V.CX1164) switch to the chamber. This insures good multitrack efficiency as is demonstrated in Fig. B3 which shows a trimuon event from our Summer 1978 run.

Toroid Spectrometer

The spectrometer assembly consists of three iron ion core magnets instrumented with a total of 36 5' x 10' magnetostrictive

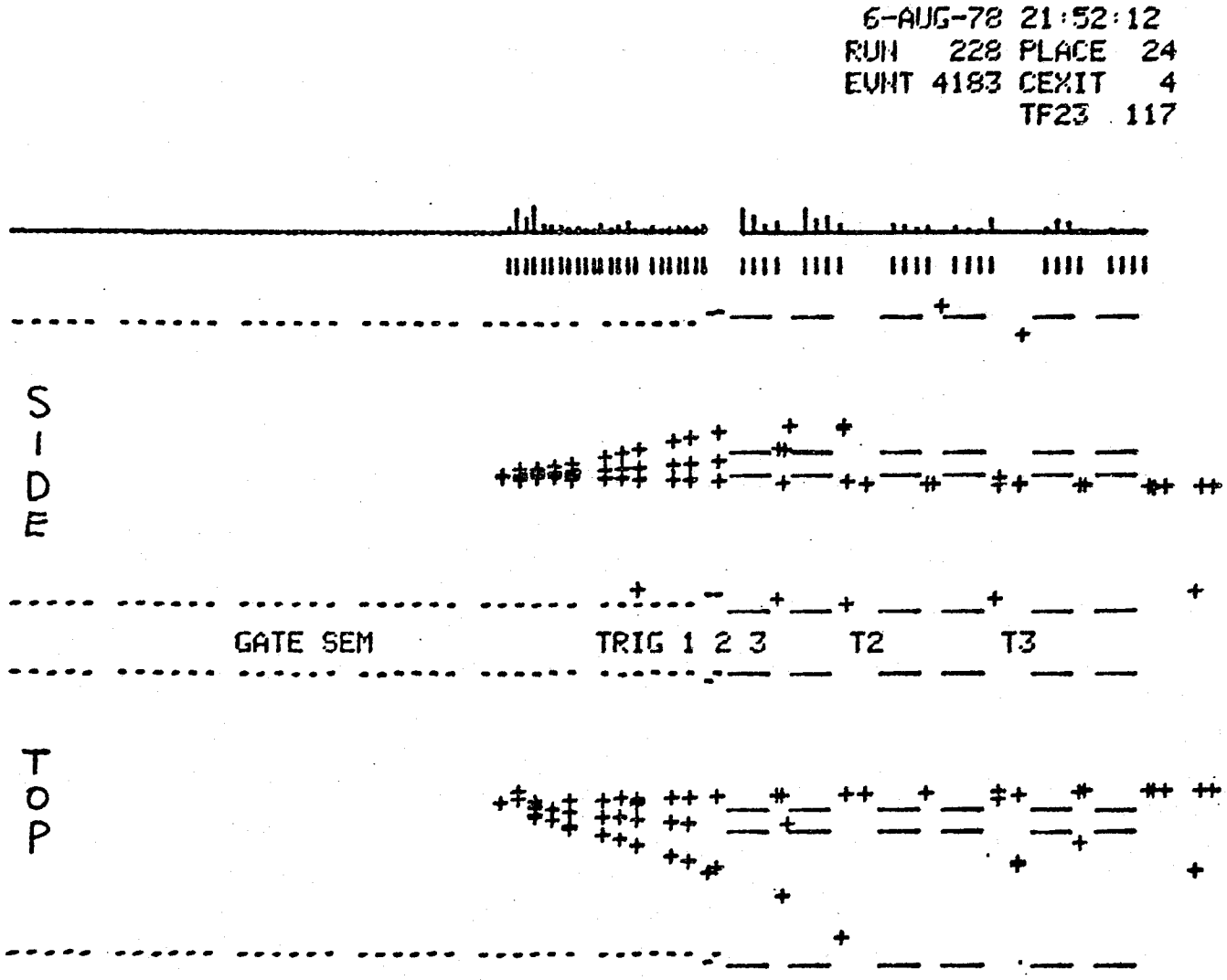

Figure B3

Tri-Muon Event

TOROIDS

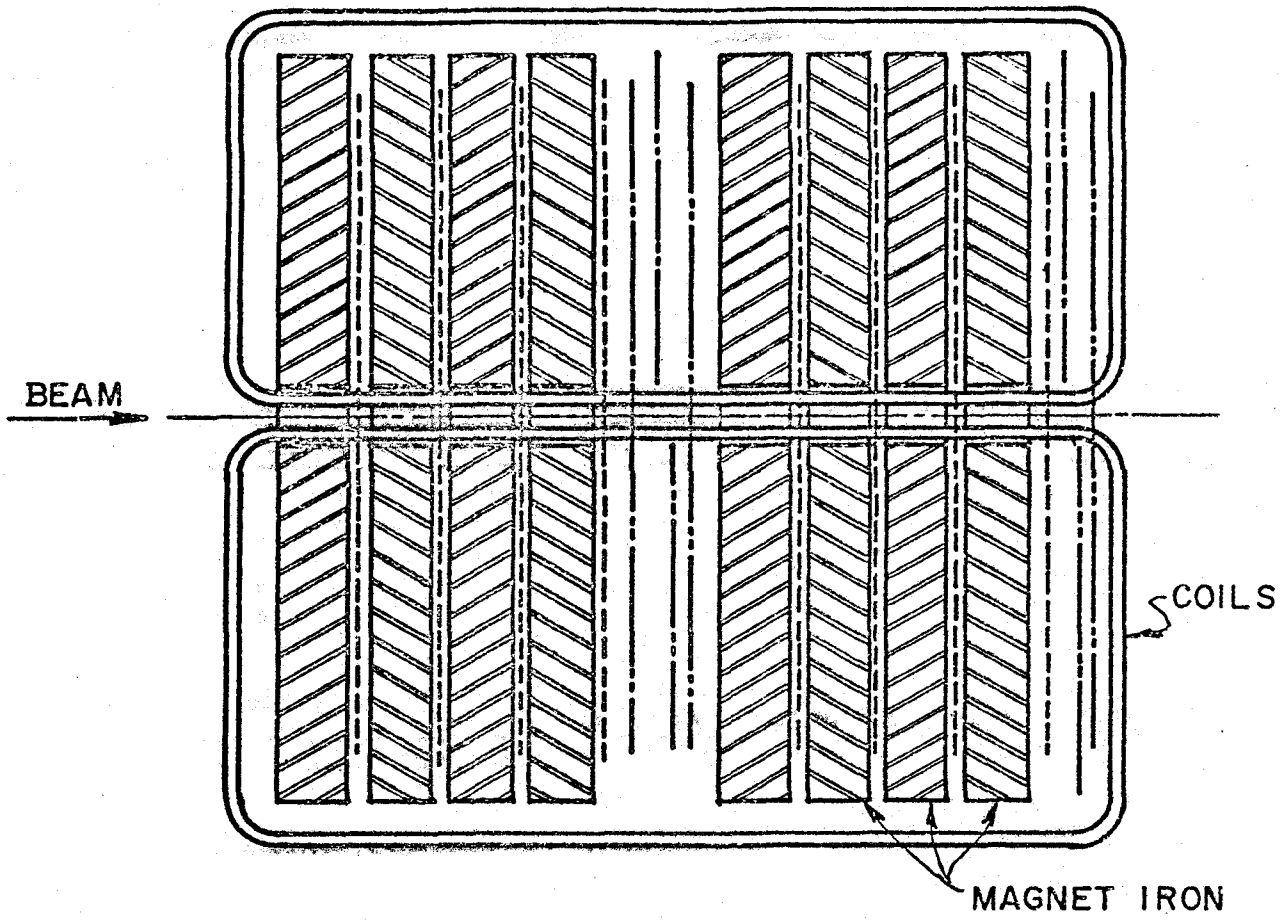

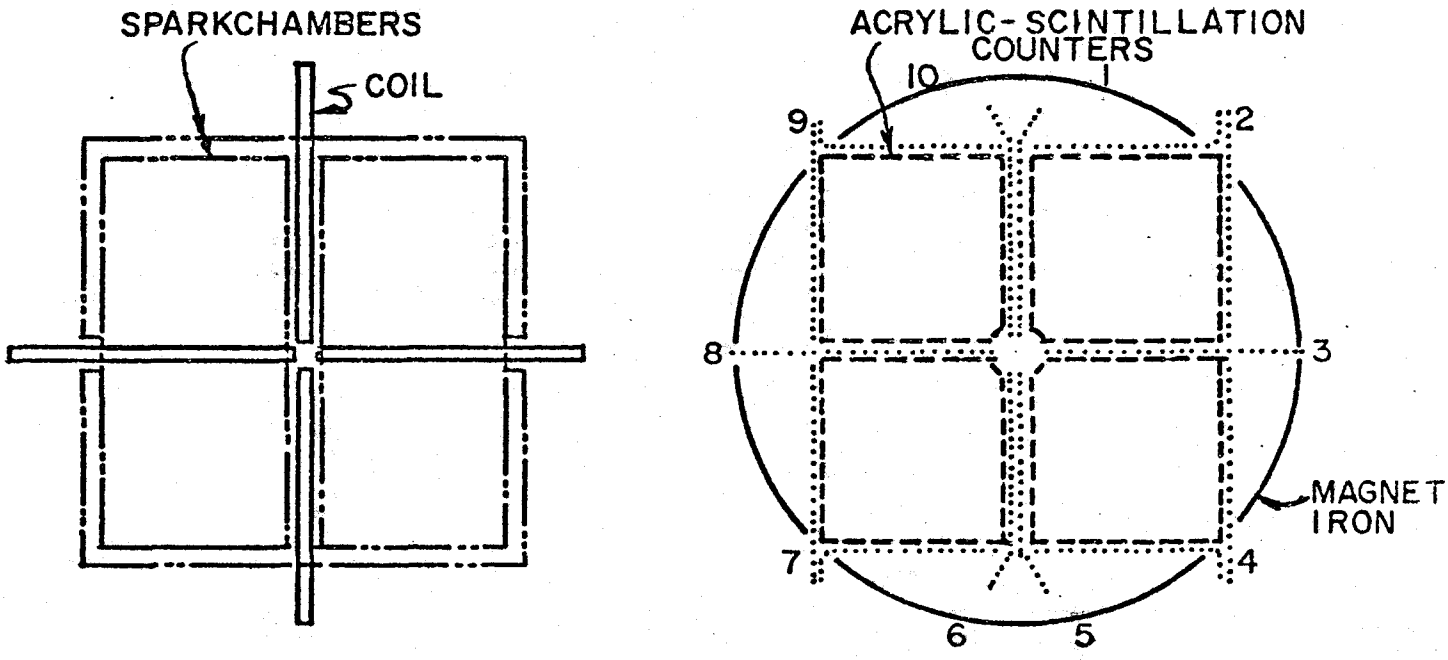

Figure B4
Toroid counter arrangement

spark chambers and 24 planes of acrylic counters doped with scintillator (Fig. B4). Each of the three spectrometer magnets can be independently translated into the hadron beam for calibration. The 11.5' diameter toroids are made of eight donut slabs of 8" thick steel. There is a 10" diameter hole in the center of the steel for the four sets of coils which power the magnets and the top and bottom halves of the steel are separated by a 3/8" air gap to facilitate field measurement. The average field of 17 Kg over the 16' length of the three toroids provides a total transverse momentum kick of 2.45 GeV/c. As discussed in Appendix C the multiple scattering in the steel gives a muon momentum resolution slightly greater than 10.5%. A very small fraction of the muons interact in the steel (i.e., deep inelastic muon scattering, high energy delta rays, etc.) leaving behind a significant amount of energy. Events of this type are easily recognized by measuring the muon with wire spark chambers which are interspersed between various sections of the 8" thick steel slabs and by pulse height in the counters which are located after every 8" of steel. The arrangement of counters, spark chambers, and steel also allows the toroids to be used as a magnetized target for neutrino interactions.

Toroid Counters

The 24 toroid counter planes each consist of two half planes (Fig. B4). A half plane contains two 5' x 5' acrylic counters and associated wavelength shifter bars (Ref. D1). Five photomultipliers collect light from the wavelength shifter bars on each half plane resulting in 10 PM's per plane. As in the case of the target,

the toroid counters have been calibrated with hadrons. The energy resolution is about a factor of two larger than for the target and is given approximately as: $\sigma E_H/E_H = 2.0/\sqrt{E_H}$. The segmented counters in the toroids allow considerable flexibility in triggering, especially relative to multimuons.

Triggers

For triggering purposes there are two arrays of counters between the toroids called T2 and T3 (Fig. B3). There is also a veto counter at the front of the building to reject triggers from muons made in neutrino interactions upstream of Lab E. There are presently five types of triggers generically labeled: (1) muon, (2) hadron energy, (3) penetration, (4) multimuon and (5) straight-throughs.

The last category is muons which enter the veto counter and pass through the trigger counters between the toroid modules. They are prescaled to limit the rate at which they are collected and are generally useful for calibration and monitoring of the equipment. The muon trigger events originate in the target and then pass through T2 and/or T3. This trigger implies a muon has reached the toroid spectrometer. The penetration trigger requires particles to pass through several consecutive counters (at least minimum ionizing) and also requires some modest energy deposition in the calorimeter. It does not require any particles in the magnet. Typically the penetration requirement is 14 counters. The hadron energy trigger requires approximately 10 GeV of energy deposition in the target but makes no demand on penetration in the target or

the magnet. This trigger provides neutral current data and frequently satisfies other trigger requirements. The multimuon trigger requires greater than 1.5 times minimum in the downstream section of the target and can also be satisfied by various quadrant combinations in the toroids.

Since there is very little logic overlap in these triggers, they are rather complimentary in the regions of scaling variables which they cover. In fact there is considerable kinematical overlap and this allows for very good trigger efficiency.

Appendix C (From FNAL Proposal 616)

Position Detection

Measurement of the muon angle (θ_μ) and energy (E_μ) is accomplished using an array of spark chambers and toroidal iron magnets. The muon angle is measured by magnetostrictive readout spark chambers located inside the steel target every 20 cm of iron. These chambers are pulsed by a charge line system that gives very good multi-spark efficiency and are read out by a system allowing up to sixteen sparks per chamber. The resolution is limited by multiple scattering and by setting error in the spark chambers. One very important feature of this apparatus is the ability to track the muon close to the vertex, even in the presence of energetic hadron showers. Figure C1 shows, from a random sample of events taken with 300 GeV neutrino running, a spark can be found one chamber from the vertex half the time and in the next chamber over 3/4 of the time.

The angular resolution, then can be seen in Figure C2. An appropriate parameterization is given by:

$$\sigma_\theta^{proj} \text{ (mrad)} \approx 0.3 + 68 \text{ (GeV)}/E_\mu \qquad \text{(C1)}$$

It should be noted that, in an apparatus in which the spacing of position detectors were 2-1/2 times larger, and a magnetic field were present, the standard deviation for the angular measurement would be more than twice as large as Equation (C1) over most of the energy range.

The muon energy is measured by observing magnetic deflection in traversing the toroid spectrometer. For example, the curvature fit to the track in figure C3 gives a momentum of 149 GeV. The spectrometer system consists of 24 iron discs 20 cm thick interspersed with acrylic

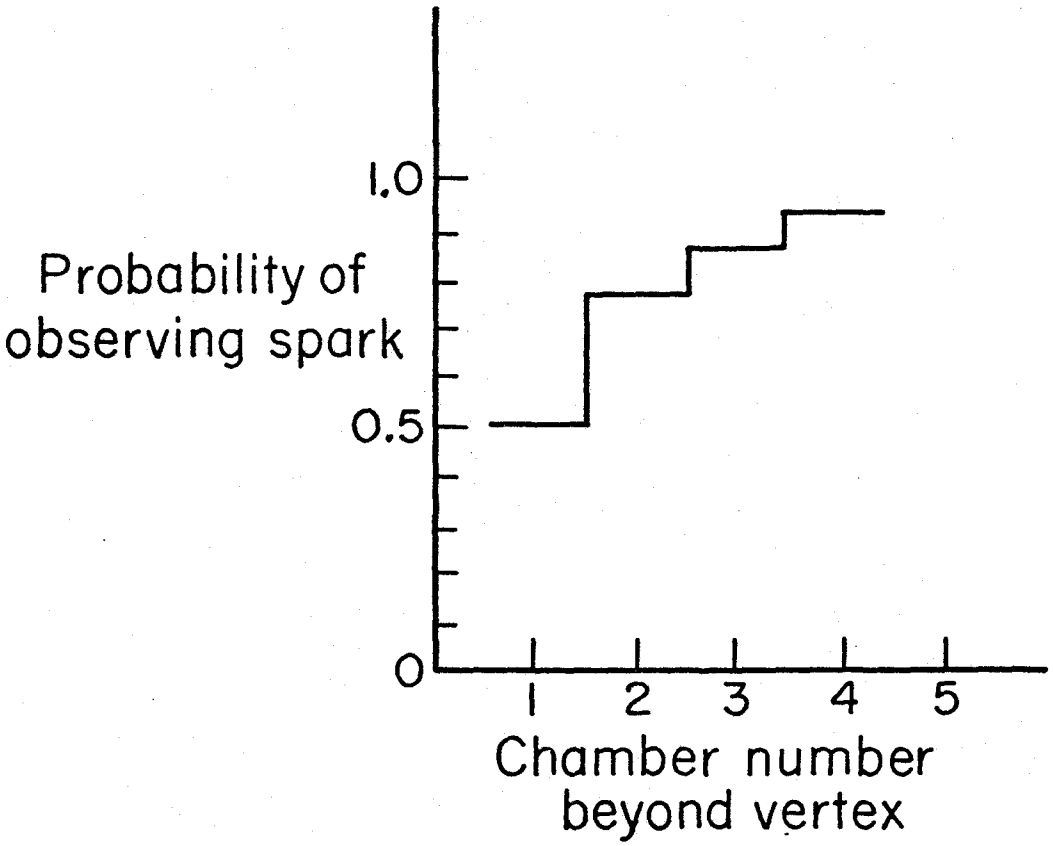

Figure C1

Experimental determination of spark presence on muon tracks near interaction vertex.

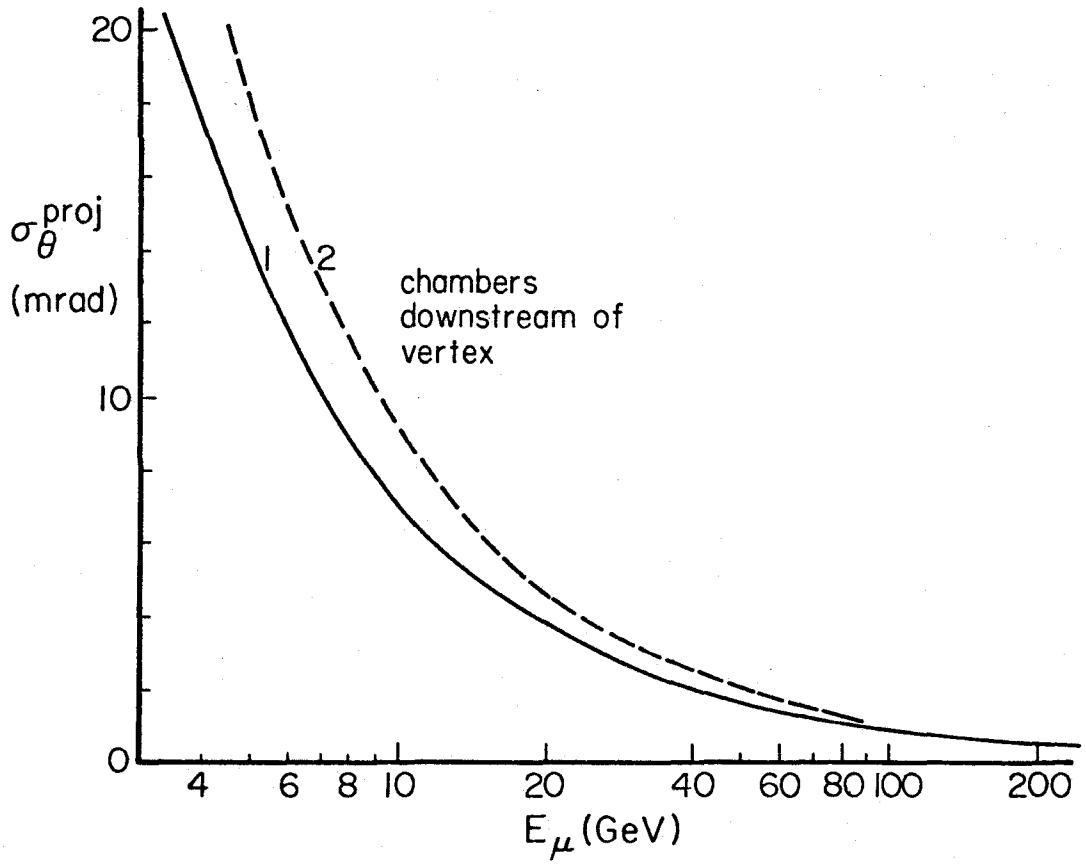

Figure C2

Projected angle error vs. muon energy for geometry of spark chambers in this experiment. Curves are shown for the first spark observed at the first (1) and second (2) chambers, respectively, from the vertex.

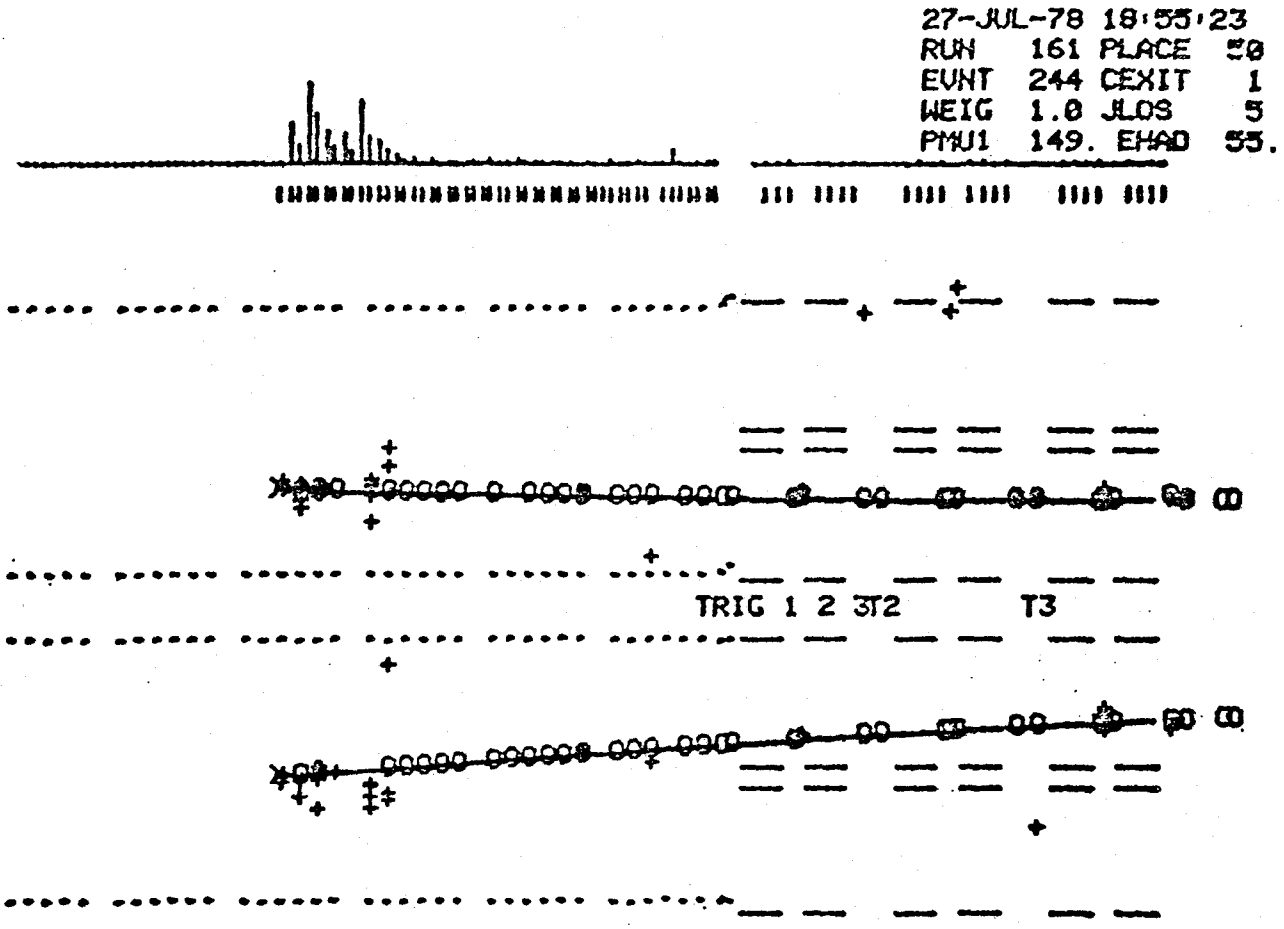

FIGURE C3

Figure C3: Typical event.

scintillation counters every 20 cm and magnetostrictive readout spark chambers every 80 cm. Events with large muon energy loss due to deep inelastic scattering or delta-ray production are sensed by detecting large pulse heights in the scintillation counters. For muon energies below 200 GeV, the momentum resolution is dominated by multiple scattering of the muon in the toroid steel. The total $\int Bdz$ of the magnets is 80 Kg-m, corresponding to a radial momentum kick of 2.4 GeV/c and a momentum resolution of 10.5%. At very high momentum, the resolution becomes limited by the setting error in the spark chambers and the measurement lever arm.

APPENDIX D: CALORIMETRY

(From FNAL Proposal 616)

This section concentrates on the performance of the liquid scintillation counters in the target carts. A detailed description of these counters can be found elsewhere (Ref. D1).

Measurement of the hadron energy in a neutrino interaction is obtained from the 10' x 10' liquid scintillation counters positioned every 10 cm of steel in the target calorimeter. The light produced in these counters is collected by 8 wavelength shifter bars located on the sides of the counters. Shifter bar light is then guided into four photomultipliers at the corners of each plane. In total, there are 82 such counters in the target calorimeter arranged on six carts as described in Appendix B.

Extensive studies have been made in the N5 hadron beam line to study the response of these counters to muons and to hadron showers of known energy. Initially all counters were adjusted to give a balanced response by means of the light flasher system. Then muons were directed through the system and all counters had their absolute gain measured. For a minimum ionizing particle traversing the center of the counter, a yield of 16 photoelectrons is obtained when the pulse height of the four photomultipliers is summed. A typical pulse height distribution is shown in Fig. D1. We have investigated the linearity of response, the resolution, and the position dependence of these quantities for the entire target calorimeter as a function of energy. The pulse height distribution for 100 GeV hadrons is shown in Fig. D2. To obtain this distribution, the outputs of 56 phototubes were summed.

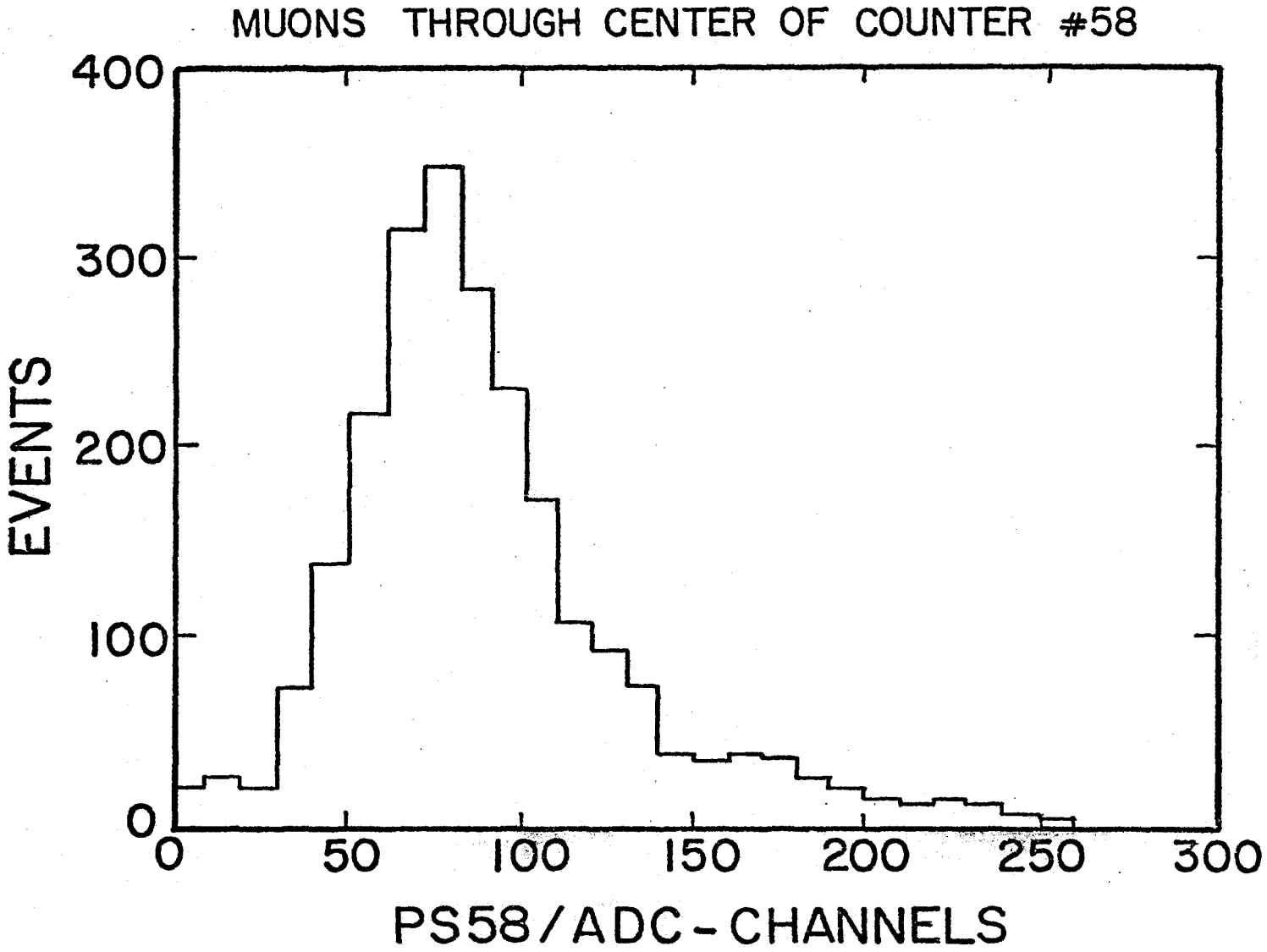

Figure D1

Pulse height distribution for muons traversing the center of a counter.

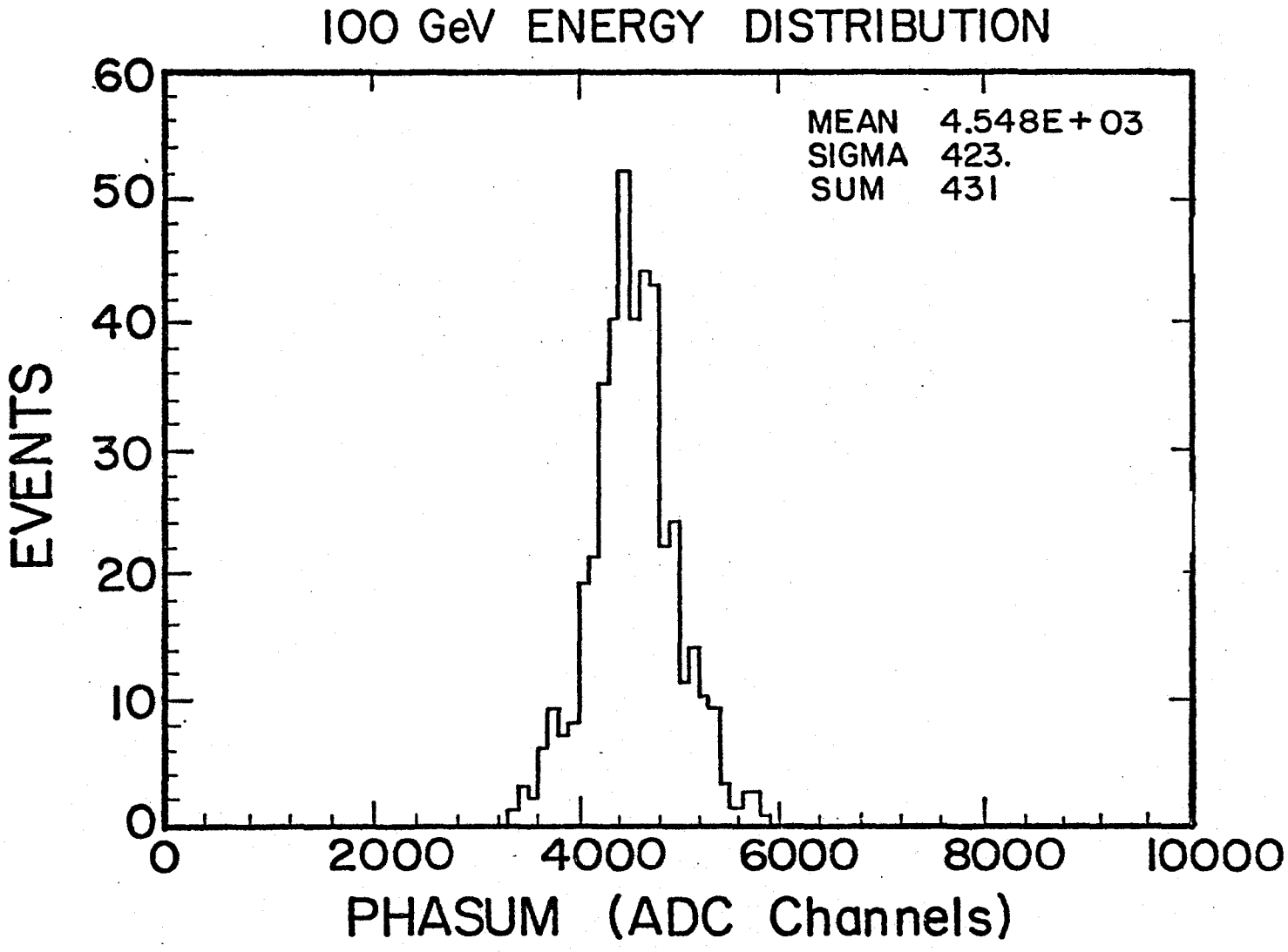

Figure D2

Pulse height distribution for 100 GeV hadrons in the center of a cart. The pulse height is summed up over 14 planes (1 cart).

The pulse height linearity between 25 and 300 GeV is shown in Fig. D3. A best fit for the response is:

Pulse Height (min. ionizing) = 4.7 x Energy (GeV).

To obtain this measurement the pulse heights of 14 counters, sampling 1.4 m of steel, were summed to avoid leakage problems. The pulse height for each plane was divided by the pulse height a muon would have at the location of the shower. The result is given in number of equivalent minimum ionizing particles. The horizontal errors shown correspond to an uncertainty of 2% in the beam energy.

The energy resolution over the region of 25 GeV to 300 GeV is shown in Fig. D4. The best fit is:

$$\sigma\,(\text{GeV}) = 0.93 * \sqrt{E_H} \text{ where } E_H \text{ is given in GeV.}$$

It should be noted this resolution function is the result of on-line analysis taken with different target carts in two calibration runs separated in time by six months. It was reproducible to about 2%. In a more detailed off-line analysis, we may be able to improve the resolution further.

The dependence of pulse height on the position of the shower is shown in Figures D5a and D5b. In Fig. D5a the variation for a single photomultiplier is shown. In Fig. D5b the variation for the sum of the four photomultipliers in a given plane is listed. The sum varies by roughly a factor of 2 between a shower created in the center of the counter and one near the corner. This variation in response can be corrected by using the counter maps derived from muons.

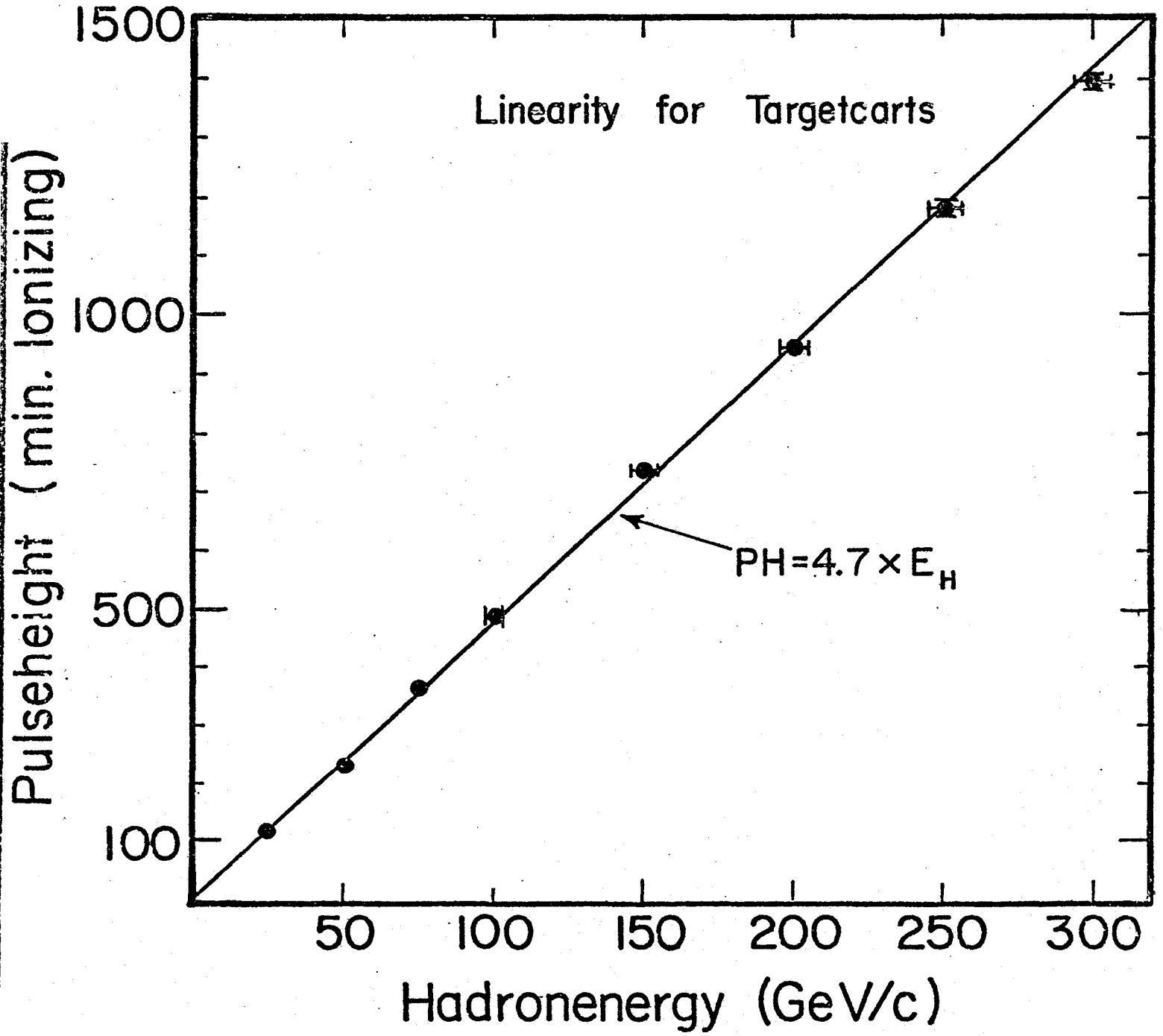

Figure D3

Linearity curve: Pulse height versus hadron shower energy.

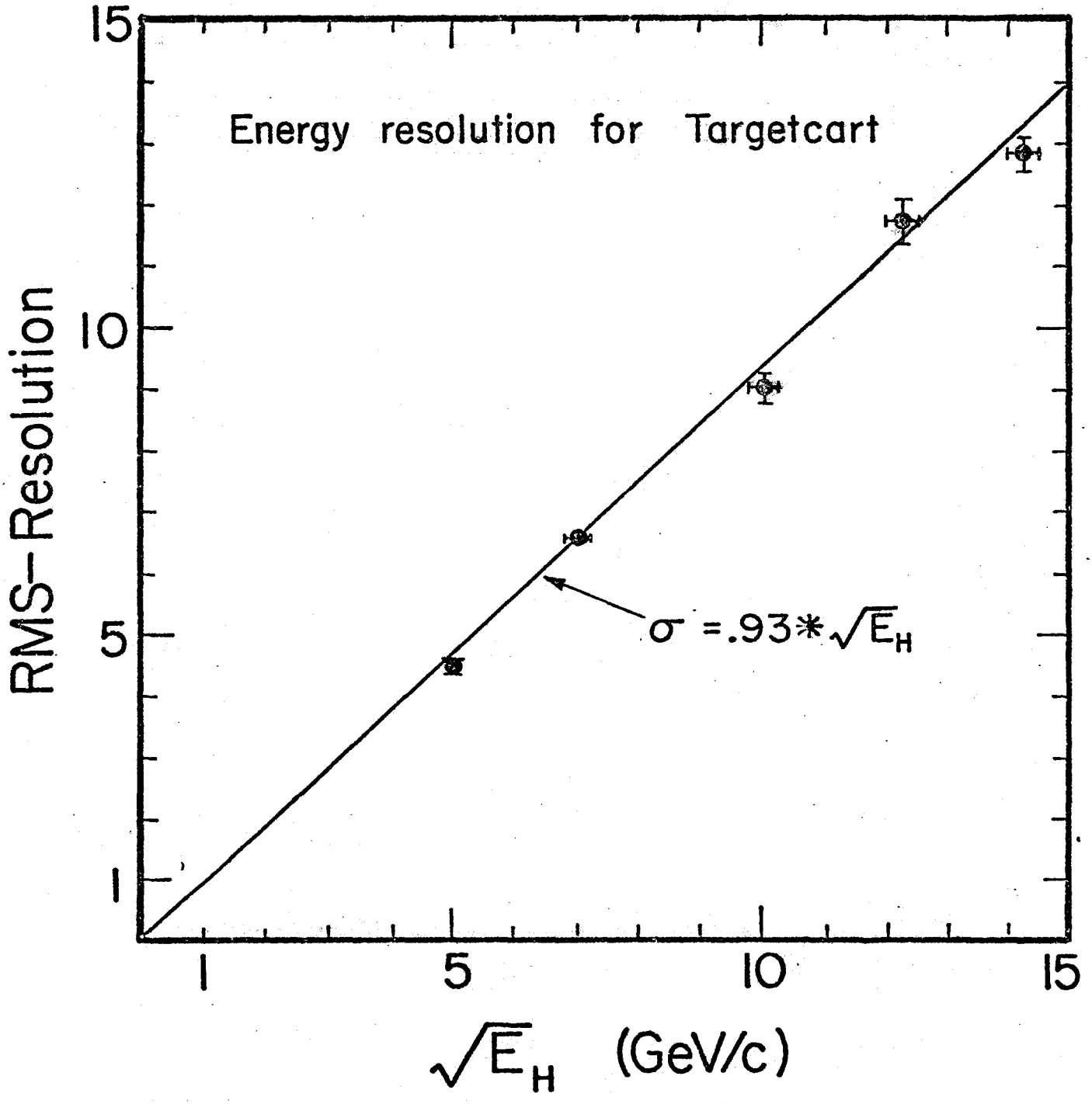

Figure D4

Energy resolution for hadron showers.

Pulseheight versus Position

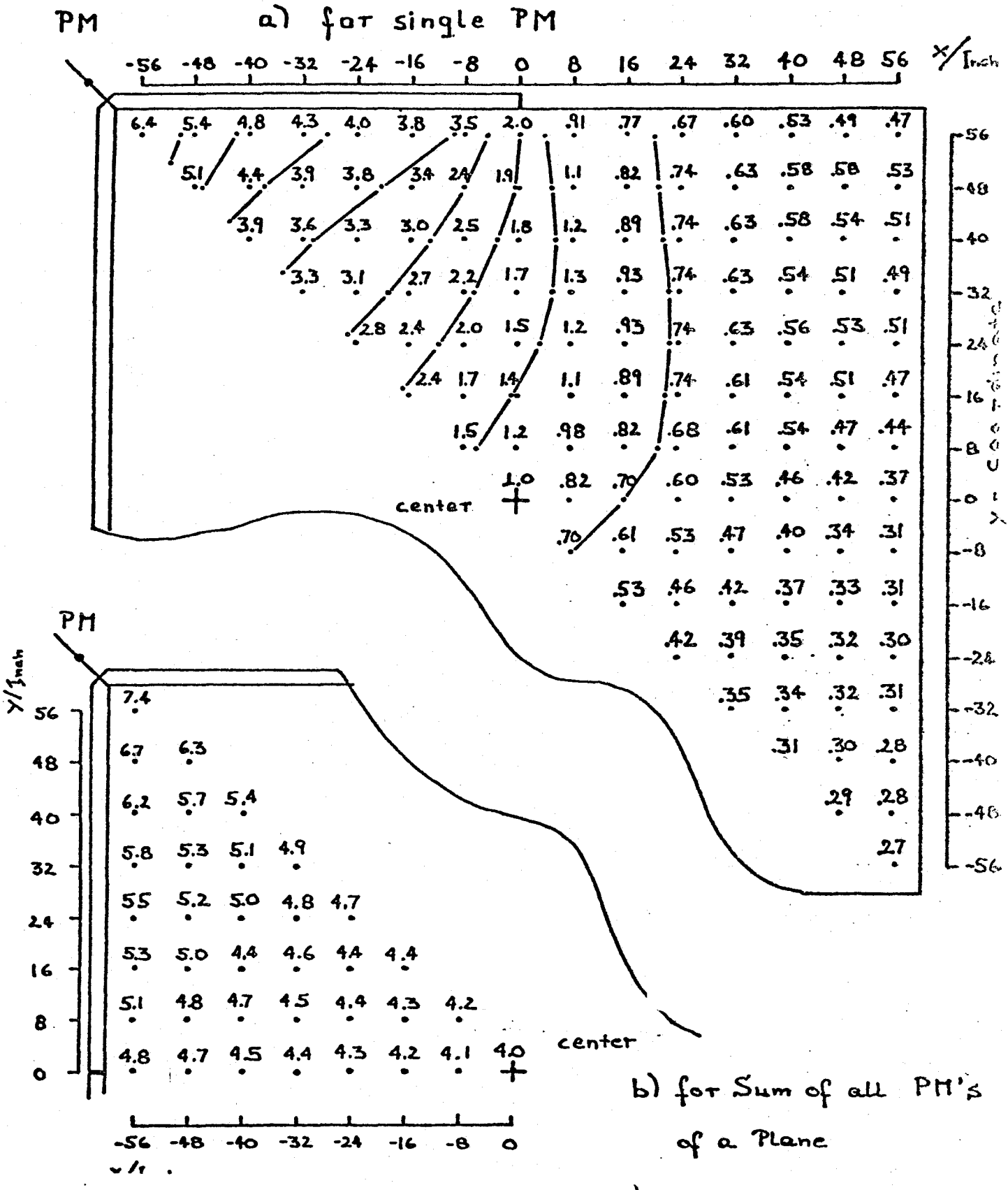

Figure D5

Variation of pulse height with position.

When all the corrections are made, the hadron energy, determined by these counters, and the muon energy, determined by the toroid spectrometer system, are combined to give the observed neutrino energy. Since 98% of the neutrino flux is due to two-body decays, the neutrino energy can be inferred from the initial hadron decay angle, which in turn, is determined by the beam geometry and the radial displacement of the event from the beam axis. This energy is, of course, subject to the two-fold ambiguity of the neutrino parent. However, the favorable geometry of the Fermilab dichromatic neutrino beam combined with the good resolution of the Lab E apparatus give the precision to make an unambiguous choice as to the initial ν energy. Figure D6 shows preliminary results on the mean observed total energy versus radius for events obtained during the initial run of E356 with the beam tuned to 300 GeV. The solid lines are a Monte Carlo calculation of the energy spectrum for the dichromatic beam using realistic beam divergences and spot sizes. The points are obtained from the measured events. The horizontal error bars show the width of the bins chosen; the vertical error bars are set at 5% although the statistical errors are smaller. There has been no shifting of energy in either the calculation of the beam energy or in the calibration of the hadron calorimeter or muon spectrometer. This graph confirms the absolute calibration of our measurements and clearly demonstrates the dichromatic nature of the beam. The deviation of measured values from calculated values at large radii, for the pion neutrinos, is due to wide-band background at low energy. This background is related to difficulties in dumping the proton beam at high positive tunes and should be corrected for our next run.

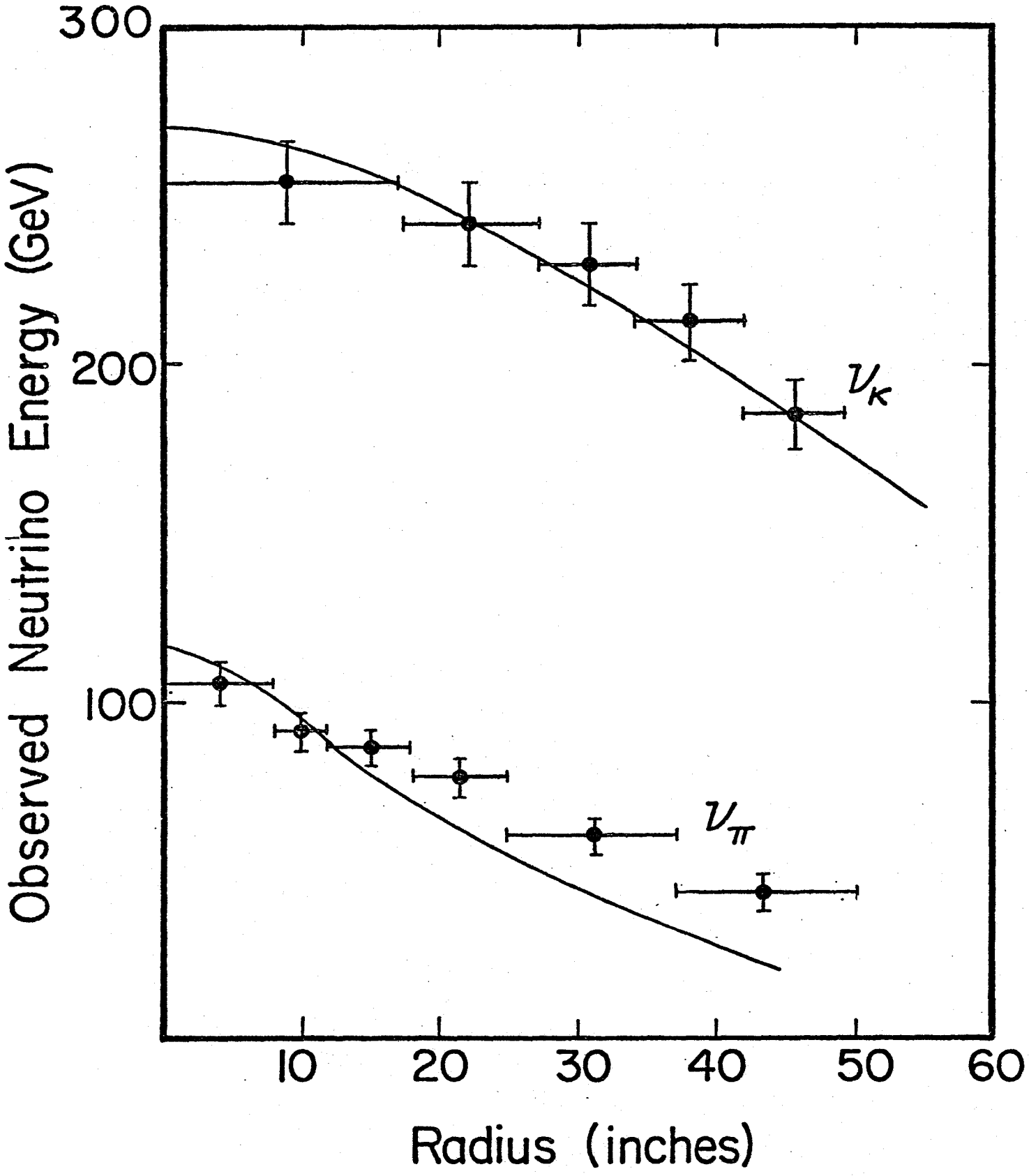

Figure D6
Observed neutrino energy versus Radius

REFERENCES

D1 B. C. Barish et al., Very Large Area Scintillation Counters for Hadron Calorimetery.
IEEE Transactions on Nuclear Science NS-25 (1978) 532.

Appendix E: Comparison of this experiment with its European Counterpart
(From FNAL Proposal 616)

In proposing this experiment, we are vaguely aware of a comparable experimental apparatus presently operating on the mainland of Europe. It is inevitable that the question will pose itself as to the relative strengths and weaknesses of the two devices for doing the physics described in this proposal. Though such questions contain a certain inherent tackiness, we anticipate them and shall attempt to respond with our customary restraint, humility, and objectivity. Table E1 shows a comparison of the general features of the two set-ups.

The total mass(item 1) of the two set-ups are similar. The Lab E modules have built-in capabilities for horizontal rearrangement. (Note that some vertical rearrangement has occurred in the Alpine device to partially compensate the Emmentaler effect (see below).) A detailed comparison of the calorimeters(item 2) shows that the Lab E set-up has a more massive fine resolution section. This section is also uniform and un-magnetized, without the very serious complications arising from the hole and coils(Emmentaler effect) in the Swiss target calorimeters, which double as toroids. It should be noted that the Fermilab target has twice the steel thickness(10 cm) between scintillation counters of its counterpart(5 cm), a major factor in total cost, and yet has an almost identical experimentally established energy resolution.

The CERN apparatus has a larger crude sampling calorimeter; however, when the fiducial cuts are made[8] the actual usable target volume is not appreciably larger than the Fermilab apparatus.

The obvious advantage of choosing a totally magnetized calorimeter system (European Plan) over the separated function target-calorimeter and muon spectrometer(American Plan) is that of acceptance, particularly at large x and y. Figure E1 shows the calculated acceptance of the fine target portion of the Fermilab apparatus at various x-values. Note that at the typical mean

Table E1: Comparison of this Experimental Apparatus with its European Counterpart

CFRR	CDHS
1. Weight Movable = 1100 tons	Weight Fixed = 1380 tons
2. Calorimeter Instrumentation	
10 cm spacing	5 cm spacing
680 tons Uniform Calorimeter $\Delta E/E = 0.93/\sqrt{E}$	510 tons 30 cm hole on axis $\Delta E/E \sim .9/\sqrt{E}$
20 cm spacing	15 cm spacing
420 tons 25 cm hole on axis $\Delta E/E \approx 2/\sqrt{E}$	580 tons 30 cm hole on axis $\Delta E/E \sim 1.8/\sqrt{E}$
	290 tons Uninstrumented
3. Position Detection	
Spark Chambers	Drift Chambers
Every 20 cm of steel	Every 75 cm of steel
Uniform target	30 cm hole on axis
Not magnetized	Magnetized
Recognize spark $\geq$ 1 chamber from vertex (ie after 20 cm)	Recognize spark $\geq$ 2 chambers from vertex (ie after 150 cm Fe)
$\Delta\theta_\mu \approx 0.1/p_\mu$	$\Delta\theta_\mu \sim 0.3/p_\mu$
$\Delta p/p \approx 10\%$	$\Delta p/p \approx 9\%$
4. PR poor	PR excellent

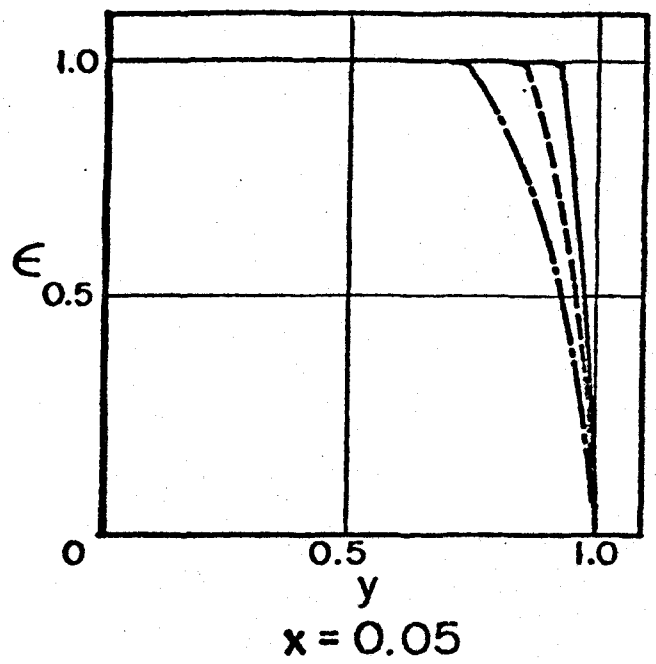

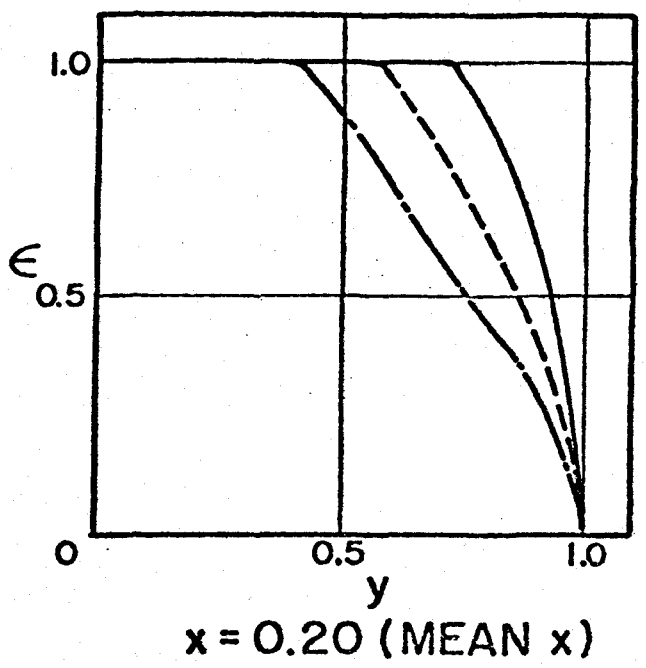

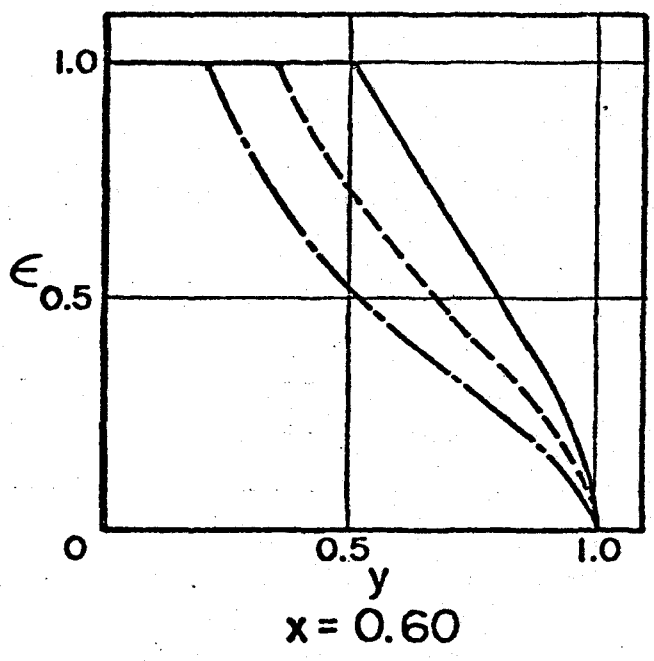

LEGEND

50 GeV
100 GeV
200 GeV

Figure E1
Typical acceptance at fixed x values for CFRR apparatus

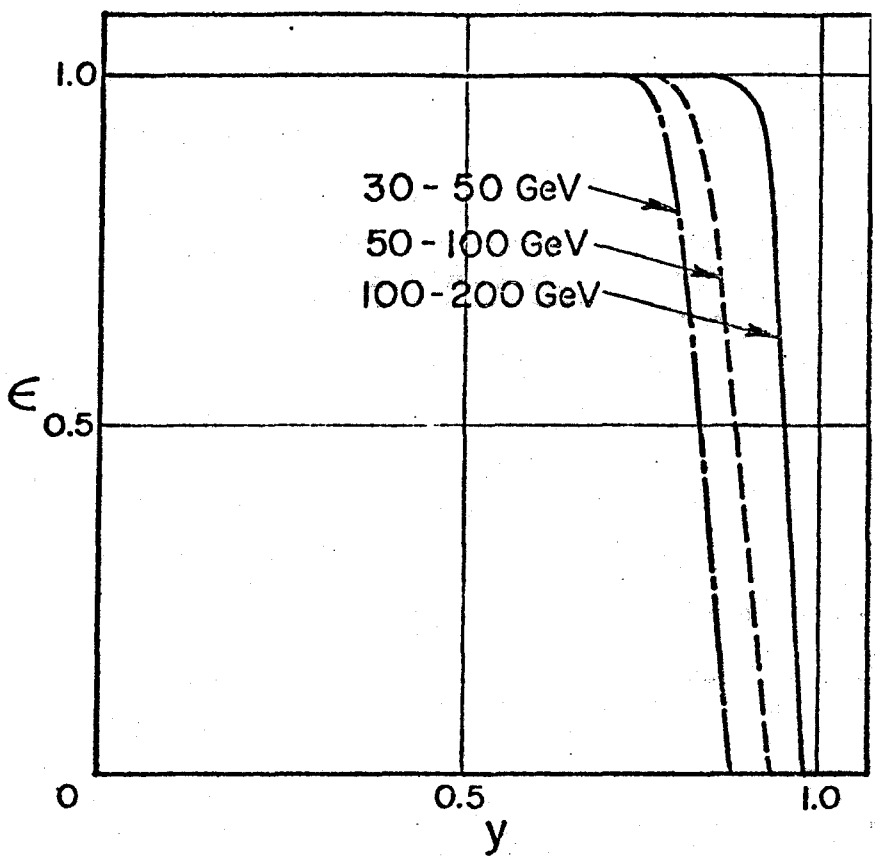

Figure E2
CDHS acceptance

value of x = 0.2, the acceptance compares favorably with the published average acceptance of the CDHS apparatus, shown in Figure E2. The acceptance of the Fermilab system is very large at small values of x where the predicted value of R is expected to be quite large. (Note also that as E_ν becomes large, the differences become even smaller.) This comparison has not assumed use of the muon spectrometer portion of the Fermilab set-up as target, which would boost the event rate at large y. Since large y corresponds to large E_ν and small E_μ, this region will provide events with little compromise in resolution.

For this proposed experiment, the smaller acceptance at large x of the Fermilab apparatus will not be very important, unless it turns out that R is large in this region(see Figure 1 for prediction). If this happens to be the case, the apparatus can be trivially reconfigured to substantially boost the acceptance at very large x, by translating the toroids transversely with respect to the target. The modular and flexible nature of the Lab E set-up allows response to such physics problems with minimal cost and difficulty.

In position detection(item 3), different choices were made on the technology to apply and on the spacing of the detectors. Our choices were motivated in part to provide better angular resolution by more than a factor of 3(see below). The Fermilab apparatus utilizes magnetostrictive spark chambers located every 20 cm of steel; the CERN apparatus incorporates drift chambers placed every 75 cm of steel. The magnetostrictive chambers are limited to one event per fast spill; however, the requested mode of operation for the dichromatic beam is to have multiple fast spills with the intensity chosen to be consistent with the trigger rate. The magnetostrictive chambers can easily run for multiple events on slow spill, but this mode of operation will increase the cosmic ray background and eliminate the possibility of studying neutral currents. The CERN drift chambers have the possibility of handling multiple events in a single fast pulse. This capacity is primarily useful

for the wide band horn neutrino beam running and is not as important in the dichromatic neutrino beam mode where the trigger rate is typically 1 event/10^{13} protons.

The operation of the magnetostrictive target chambers has been superb. The chambers have extremely good multi-spark capability, and permit the muon to be tracked back to the vertex in a large number of cases(see Appendix C). This, combined with other factors, is very important in the accurate determination of muon angles.

The other major considerations in measuring muon angle are (1) the use of an unmagnetized target so that the angle can be determined with as few as three position coordinates near the vertex, and (2) more frequent position sampling, so that less steel is traversed before angles are measured. Figure E3 shows a calculation of the projected-angle resolution(rms) in our experiment with 40 cm spacing(containing 20 cm steel) between chambers versus inverse momentum. The calculation includes a correct treatment of multiple scattering for the angle determination. The curves for the observed track in the first (n_s=1) or the second (n_s=2) chamber downstream of the vertex are shown. For comparison, we show typical curves for an apparatus with 103 cm spacing(60 cm steel) magnetized target. The difference in angular resolution is of order a factor of 3.

The muon angle resolution is the determining factor in x resolution at small x (see Section VII and Figure 10). For example, for E_h= 25 GeV, σ_x= 0.015 at x = 0.05 with our resolutions. Clearly, a factor of 3 worse precision in the angle determination would create problems in this region. For large values of R at small x(see Figure 1), this resolution directly affects the physics of this proposal. Another physics question related to angle resolution is the Gross-Llewellyn-Smith sum rule:

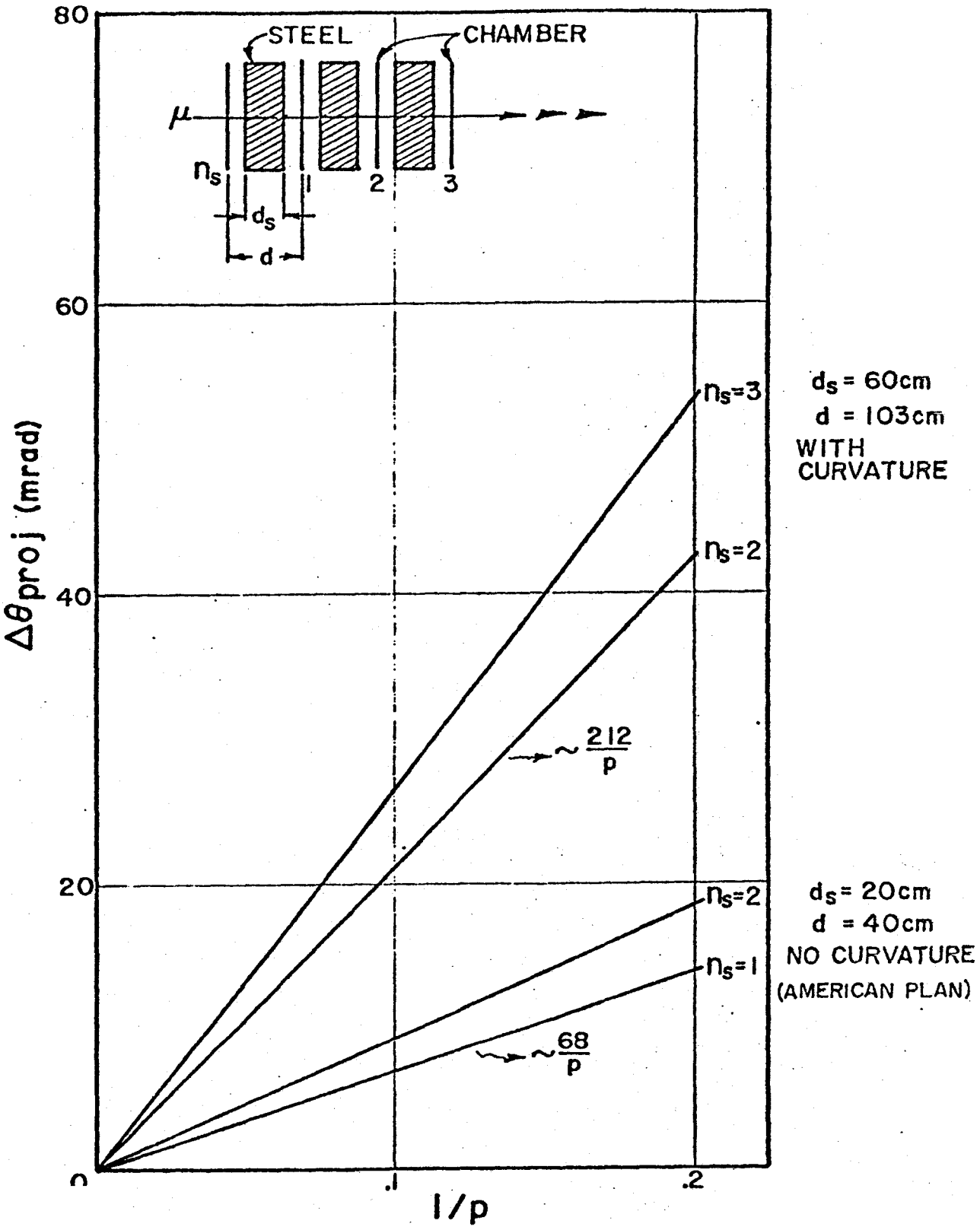

Figure E3
Angular resolution with two different approaches to position detection

$$\lim_{x_{im}\to 0} \int_{x_{min}}^{1} \frac{xF_3}{x}\, dx = 3$$

which requires x_{min} as small as possible. This experimental test obviously requires good x-measurements at small x. At small x, the resolution is given by

$$\Delta x = \Delta\theta \sqrt{\frac{2E}{M}\,\frac{1-y}{y}}\,\sqrt{x}$$

Below some critical x value, x_c, the error becomes larger than the x-value ($\Delta x \simeq x$ at $x = x_c$), and clearly

$$x_c \propto (\Delta\theta)^2$$

It makes little sense to take x_{min} smaller than x_c. Hence, a factor of 3 improvement in angular resolution is worth an order-of-magnitude in the lower limit of the x-integration for checking this important sum rule.

The overall impression which one receives from these comparisons is one of equality with slight differences in emphasis relating to certain physics topics. For the physics of this proposal the Fermilab apparatus has some major advantages; namely, a larger high resolution target and greater precision on measurements of x.

We conclude with a parting comment on item(4) of Table E1 which is a clear difficulty given the necessity of this appendix. It is to be hoped that this proposal contains some factual information rectifying this situation. If this proposal is not approved, we have clearly not succeeded in turning this situation around. In that event, it will be important to open lines of communication with groups more talented in this regard and to find applications which will provide good use for the existing apparatus. (One line of thought is in studying communication via neutrino beams, a group which has recently demonstrated great talent as regards to item 4.)

APPENDIX F: FLUX MONITORING

1) Introduction

The flux monitoring system used in E-616 is shown in Fig. F1. The extracted proton beam flux is measured with a SEM, a toroid, and RF cavities located upstream of the proton target. The proton beam position and angle at the target are measured with two SWICs(Segmented Wire Ion Chambers).

The total number of hadrons traversing the decay pipe (see figure F1) is measured using charge sensitive integrating devices (RF cavity and ion chambers) at two locations in the decay pipe: the expansion port and the target manhole. Split plate ion chambers and SWIC's at these two locations monitor the beam positions and profiles. The π/K/P fractions are determined with an integrating Cerenkov counter situated in the decay pipe manhole. The measured π and K fluxes are then used to calculate the neutrino flux from known quantities, such as the π and K lifetimes, the π and K decay angular distributions, the measured secondary beam phase space, and the Lab E detector geometry.

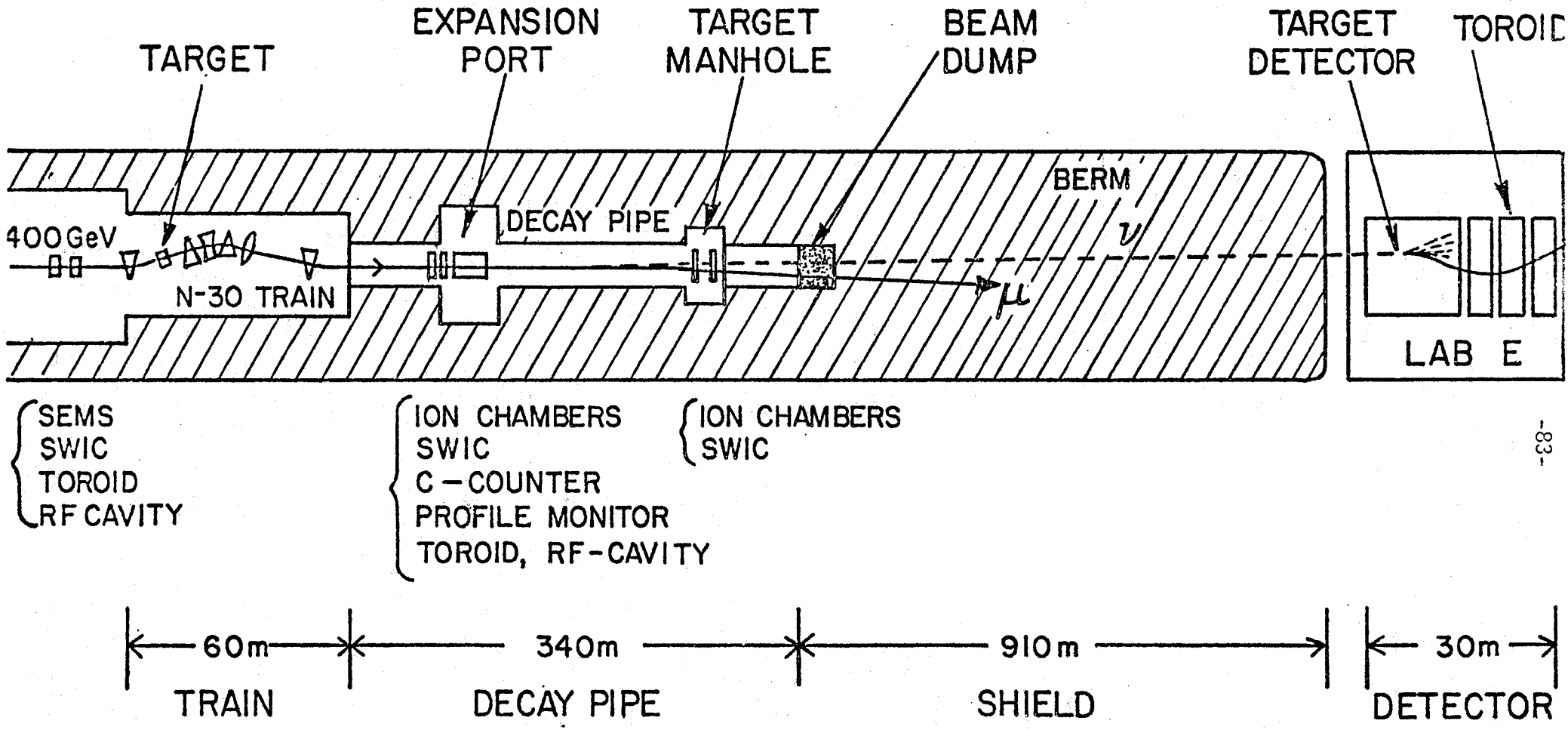

Figure F1
Neutrino Beam Line for E356

The problems associated with measuring neutrino fluxes at the desired 2-4% level are very difficult chiefly because of the high instantaneous rate of secondary particles ($\sim 10^{10}$/ms) and the large momentum bite of the dichromatic train (± 9%). Based mostly on past experience, we have developed a flux monitoring system which is achieving this goal. The system has a high degree of redundancy for two reasons: 1) different monitors have different systematics, and 2) redundancy demonstrates the accuracy that is achieved. For example, the ion chamber is sensitive to velocity dependent ionization corrections, while toroids and RF cavities are not. The toroid has a small signal level which makes it difficult to measure low intensity fluxes while the RF cavity is subject to RF beam structure effects at the few percent level. The muon SWIC (App. Sect. F5) serves to cross check both the Cerenkov counter and the total flux measuring devices since it directly measures the muons from π and K decay. An absolute calibration for the different monitors can be established using different techniques in each case. This allows a sensitive check on the overall flux normalization.

The neutrino energy spectrum at a given point in the target calorimeter depends on the secondary beam angular divergence and beam size. These quantities are measured with a scanning scintillation counter and two SWIC's located in the decay pipe. Because there is a

strong correlation between event location in the Lab E detector and neutrino energy, it is important for the beam steering to be very stable. This is especially true for the interactions of neutrinos originating from π decay since they will occur within a radius of about 9" for a 600 GeV/c secondary beam.

2) Flux Monitoring and Steering

The hadron flux is continually monitored with thin plate ion chambers. These chambers have linear responses over the range of fluxes encountered in the experiment. Figure F2 shows a plot of the expansion port ion chamber response vs. the incident proton beam SEM. From this and similar evidence involving different devices, the ion chamber linearity is known to better than 1% over the range of 5×10^9 to 1.5×10^{11} particles per pulse.

The ion chamber time stability is checked by comparing the response from the expansion port ion chamber with that from the target manhole ion chamber over the time period of our data run and by comparing the E-356 absolute ion chamber calibration with the E-616 ion chamber calibration. Both of these comparisons agree at the 1-2% level.

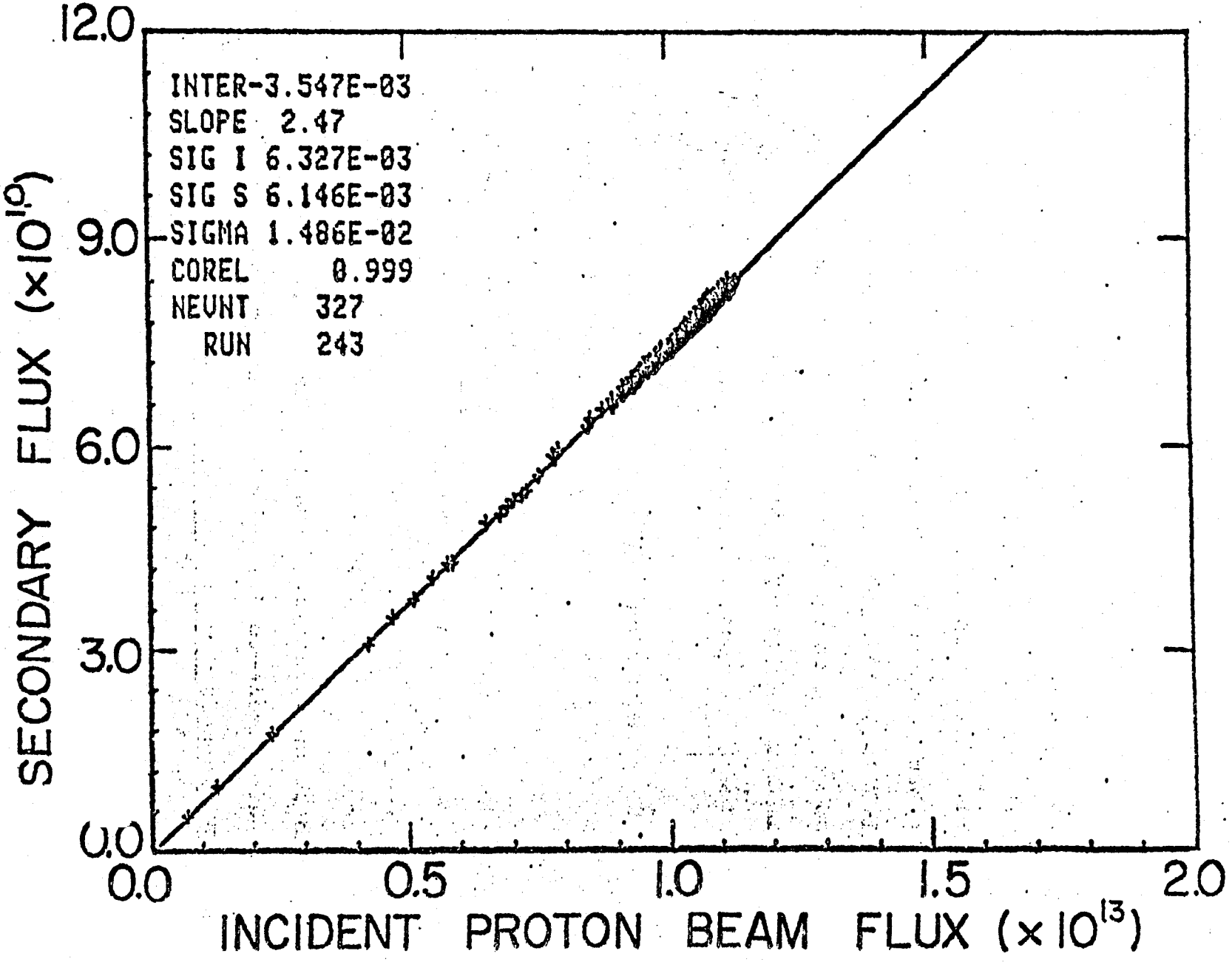

Figure F 2
Linearity of Ion Chamber response

The direction of the secondary beam is monitored on a pulse-by-pulse basis with two split plate ion chambers in the decay pipe. With the output from these chambers, the beam centroid can be stably positioned at the neutrino detector to better than one inch. Figure F3 shows the transverse profiles for ν_{π} events observed in the E-356 run.

3) Absolute Flux Calibration

An absolute calibration for hadron intensity is done by running a monoenergetic 200 GeV/c proton beam through the dichromatic train into the ion chambers and a copper foil. A foil-activation analysis provides the absolute calibration. This calibration is compared with the one done during the E-21 run in which individual particles passing through the ion chamber were counted. The E-21 calibration agreed with the foil activiation analyses at the 5% level. The agreement between the E-616 and E-21 calibrations is better than 5%. The present ion chambers will be calibrated using the particle counting method in the near future.

An independent absolute hadron calibration has been established for the E-616 RF cavity located at the expansion port. Data on tape must be analyzed before a systematic error can be stated. This will be done soon

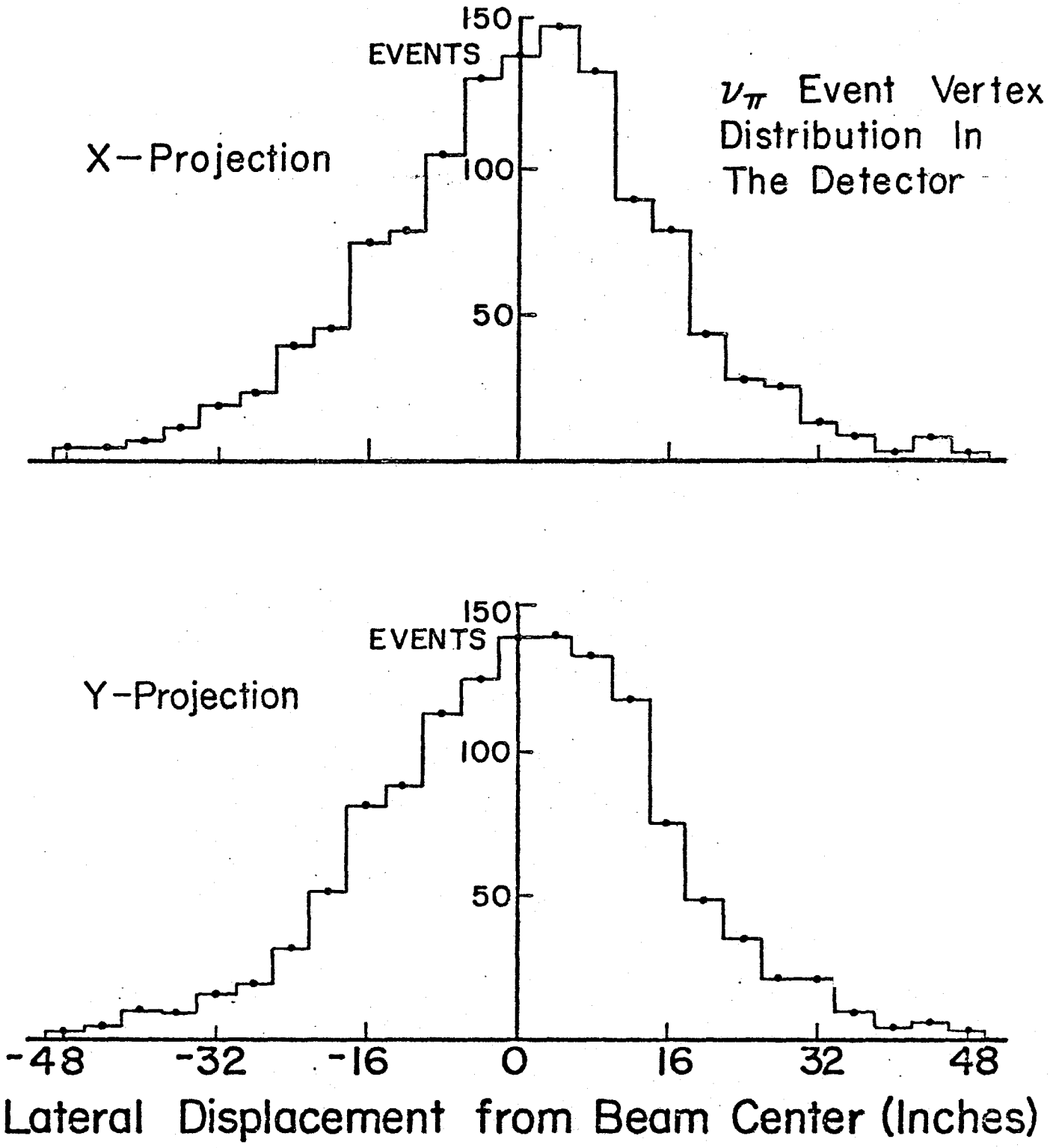

Figure F 3

ν_π Event vertex distribution in the detector

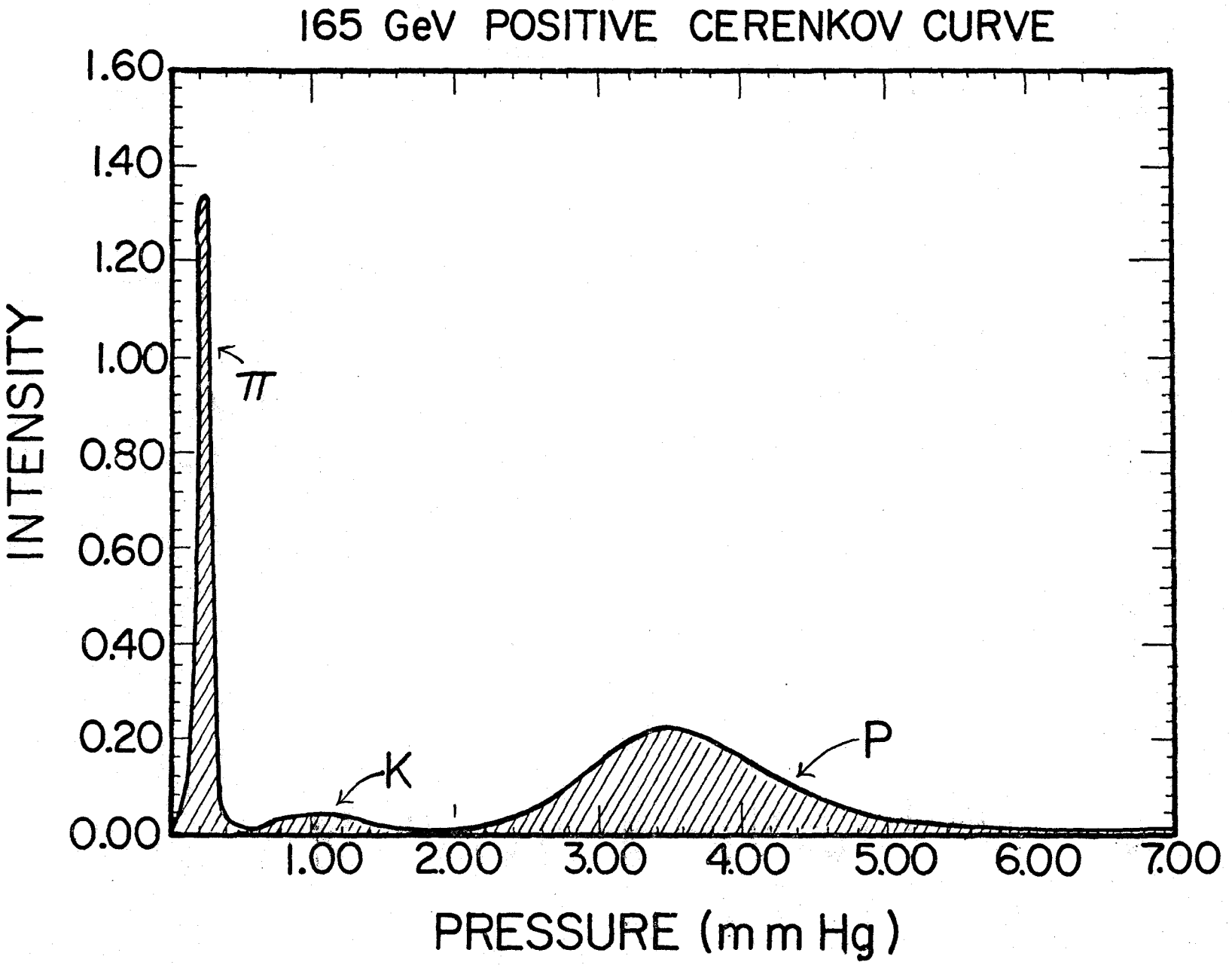

Figure F4: Cerenkov Curve for 165 GeV Positive Beam

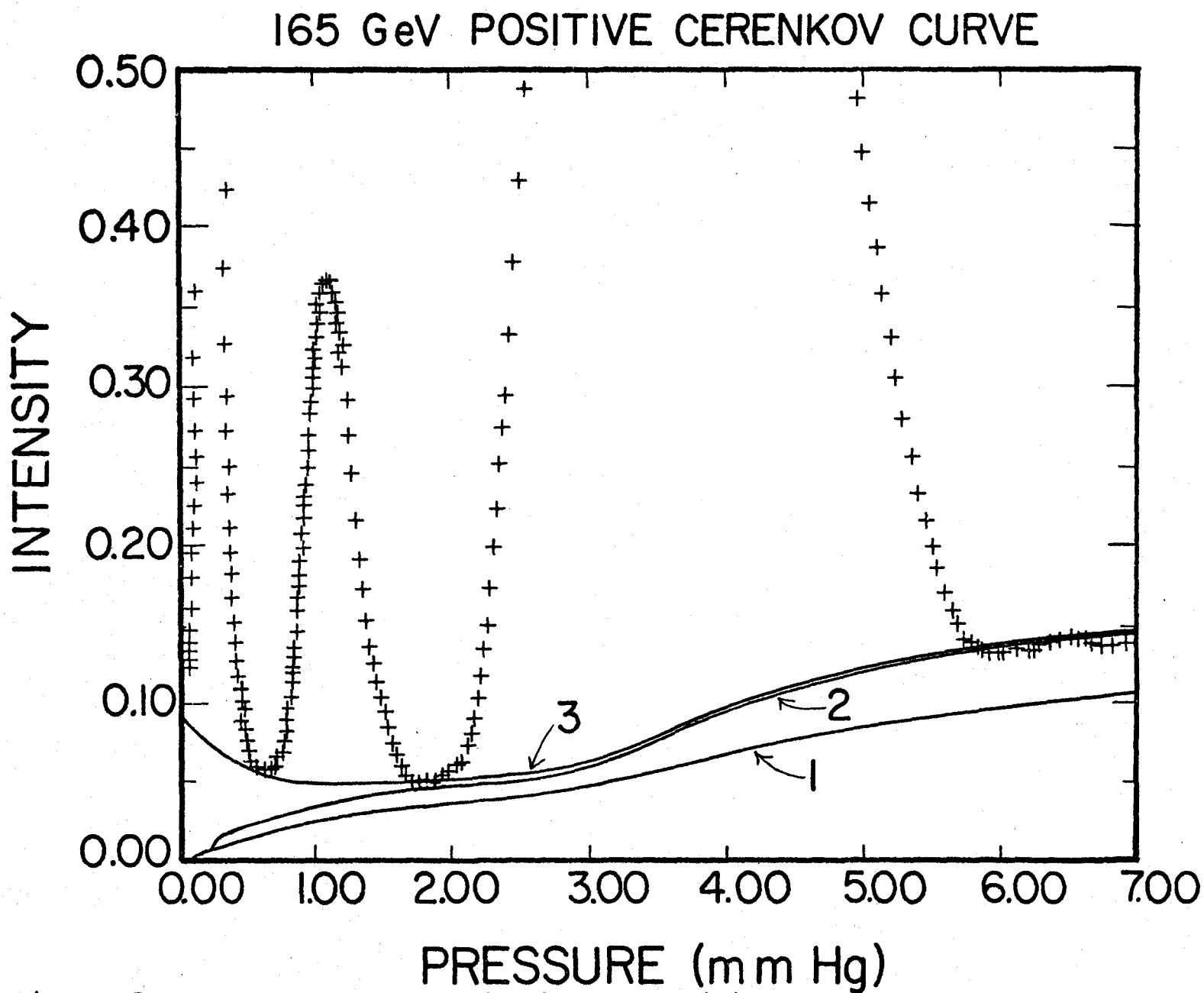

Figure F5: Cerenkov Curve for 165 GeV Positive Beam.
Curve 1 - Background from Particle Interactions
Curve 2 - Sum of (1) and of Light Scattering Background
Curve 3 - Sum of (1) and (2) and Background from Interactions in the Counter Vacuum Vessel

and may provide the most accurate absolute flux measurement. The muon SWIC (Appendix F5) will also provide a cross check on this calibration.

4) The Cerenkov Counter

The $\pi/K/P$ particle fractions are determined with an integrating Cerenkov counter. The counter now enables us to measure the particle fractions accurately enough to determine electron content in the beam (below 100 GeV) and $\bar{p}$ fractions up to 200 GeV.

Figure F4 shows a Cerenkov counter curve for +165 GeV/c beam. A measured baseline, created by Cerenkov light in the phototube and glass optics, has been subtracted. This background is measured by closing a shutter which keeps out light made by particles in the gas volume. Figure F4 shows a very small residual background above the proton signal.

The nature of this residual background is further illustrated when the vertical scale is magnified by a factor of 32 (Fig. F5). This background was measured with 200 GeV/c primary protons and secondaries at different momenta, both with and without additional material upstream of the counter. Analysis of the data enables us to determine the pressure and momentum dependence of the backgrounds. We find that the backgrounds fall into three categories. The backgrounds which result

from: 1) particle interactions in the material upstream of the counter (e.g., two titanium windows); 2) Cerenkov light scattering off the optical surfaces; and 3) a background which rapidly falls with pressure, probably due to particle interactions in the walls of the pressure vessel. These backgrounds, shown summed together in Fig. F5, can be reliably subtracted to provide π fractions to 1-2% and K fractions to 2-4% for the E-616 data.

An additional background that exists only under the π's is due to electrons in the beam. The electron fraction at lower energies is measured by taking differential Cerenkov curves, and at higher energies an upper limit is set by taking integral Cerenkov curves below the π threshold. At high energies (e.g. 600 GeV/c) the expected electron fraction is $\leq$ 1/2%.

5) The Muon SWIC

An important check on both the particle flux, as obtained by the ion chambers in the decay pipe, and the particle fractions, as determined by the Cerenkov counter, is provided by the muon SWIC which is located downstream of the secondary hadron beam dump.

Figure F6a shows an example of the muon SWIC data taken for +250 GeV/c secondaries tranversing the decay pipe, while FIg. F 6b shows the muon background induced by

a) Muon Profiles Obtained at + 250 GeV

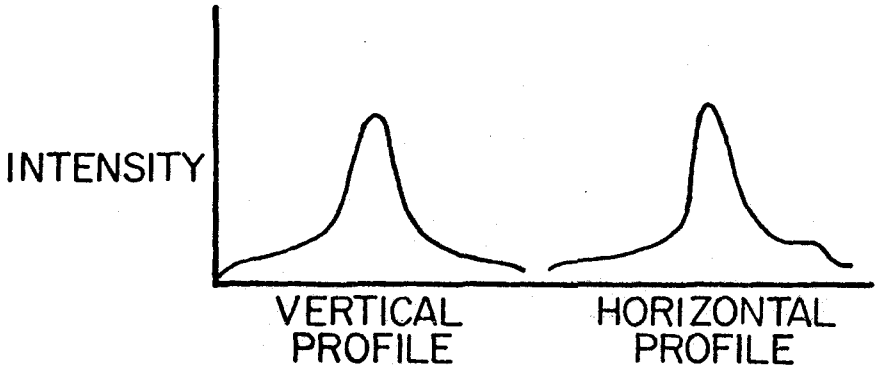

b) Muons from hadron interactions in the Dump (Scaled up by a factor of 128 with respect to a)).

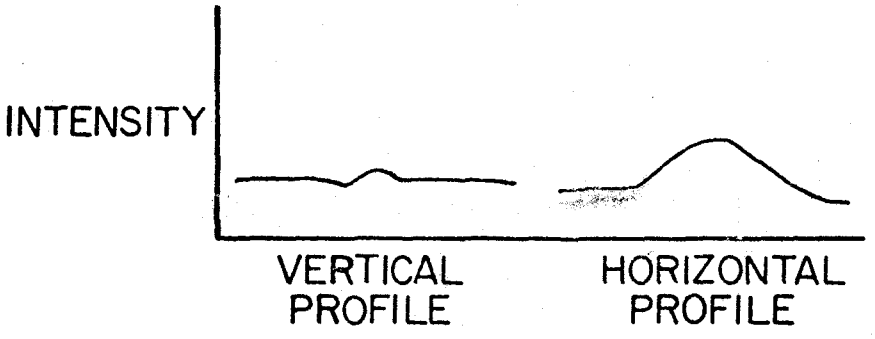

c) Illustration of the Contributions to the Signal from the Different Sources.

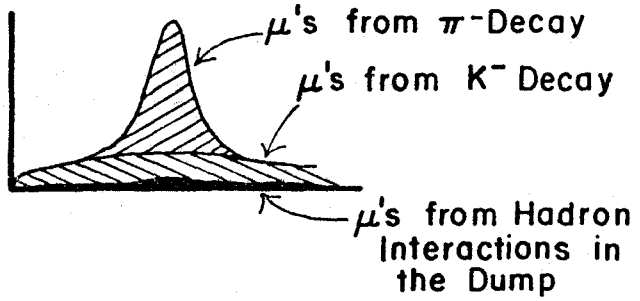

Figure F6: Determination of the Pion Flux from the Muon SWIC.

200 GeV/c protons in the dump. Fig. F 6b is scaled up by a factor of 128 relative to Fig. F6a. The separate π and K decay contributions to the muon signal seen in Fig. A6a are illustrated in Fig. F6c.

A comparison of the π^- flux obtained from a preliminary analysis of this muon SWIC data and the π^- flux as obtained from the ion chambers and Cerenkov counter is shown in Fig. F7. Since the muon SWIC has not been absolutely calibrated yet, the muon SWIC data has been normalized at 140 GeV to the π^- flux obtained from the upstream monitors. We see, even at this early stage of the data analysis, the agreement is good to ±3%.

In summary the monitoring techniques developed for E-616 enable us to measure absolute neutrino fluxes to an accuracy of 1-2% for pions and 2-4% for kaons.

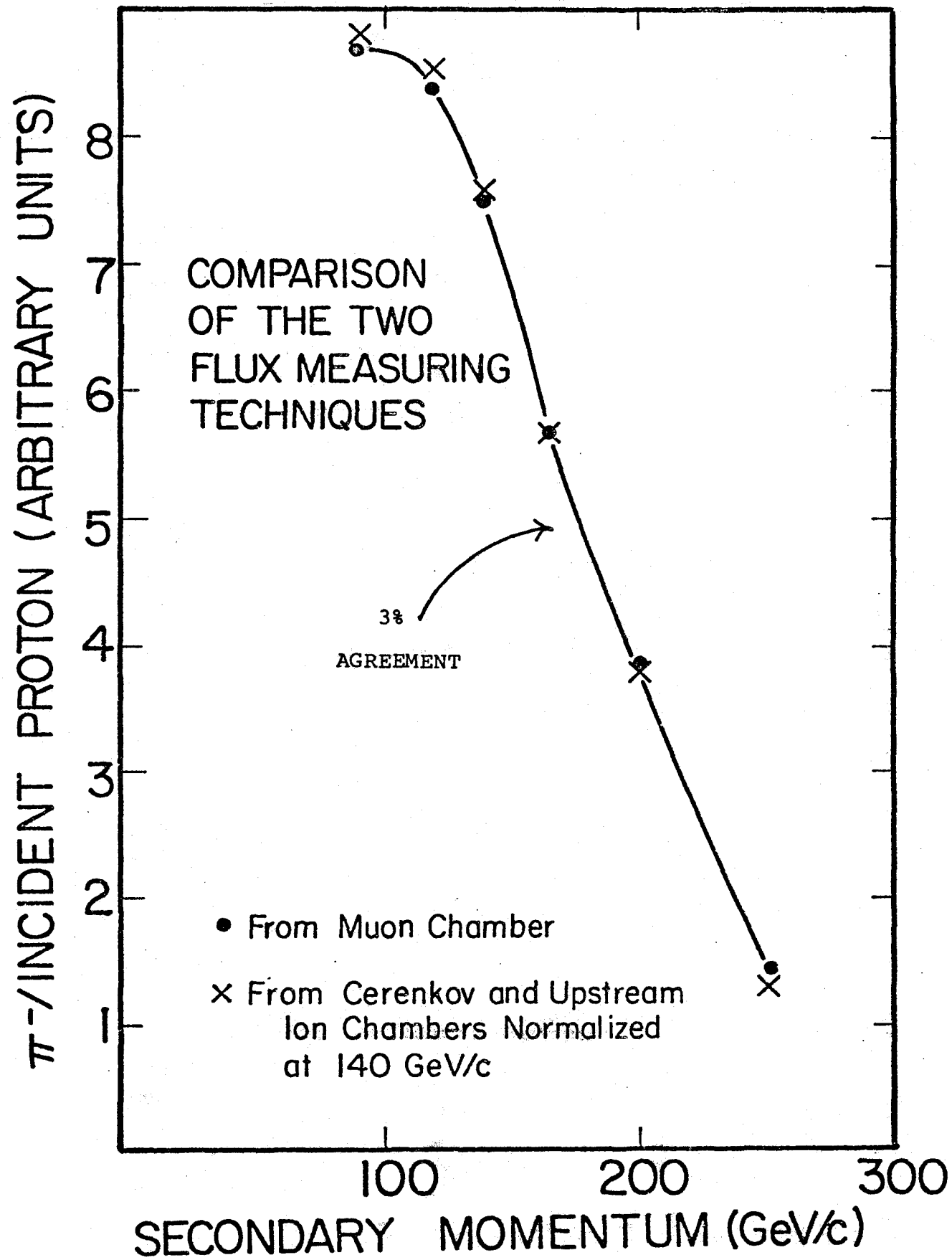

Figure F7: Comparison of Flux Measurements using the Muon Chamber with those using the Cerenkov Counter.

APPENDIX G

MULTIMUON PRODUCTION

1. Opposite Sign Dimuon Events

It is generally accepted that the predominant source of opposite sign dimuon events in neutrino-nucleon interactions is the production and subsequent decay of charmed particles. For the production of opposite sign dimuons, the GIM mechanism leads to the following prediction for an isoscalar target:[1]

$$\frac{d\sigma^{\nu}_{\mu^+\mu^-}}{dx\,dy} \propto \{ (d + u) \sin^2\theta_c + 2s \cos^2\theta_c \}$$

and

$$\frac{d\sigma^{\bar{\nu}}_{\mu^+\mu^-}}{dx\,dy} \propto \{ 2\bar{s} \cos^2\theta_c \} ,$$

where we have neglected the Cabbibo-suppressed part of the production of charm from the nucleon's quark-antiquark sea. Because of the strange quark contribution to these cross sections, the study of dilepton production in neutrino scattering is an excellent way to study the strange sea.

Since the y distribution for charm production by either ν or $\bar{\nu}$ is flat (except for kinematic effects associated with charmed quark mass, i.e., slow rescaling), we may determine the relative amount of the strange sea in the nucleon by forming the ratio:

$$\eta = \frac{2\bar{s}}{u + d} = \tan^2\theta_c \left\{ \frac{\sigma^{\bar{\nu}}_{\mu^+\mu^-} / \sigma^{\nu}_{\mu^+\mu^-}}{1 - \sigma^{\bar{\nu}}_{\mu^+\mu^-} / \sigma^{\nu}_{\mu^+\mu^-}} \right\} ,$$

where $\sigma^{\nu}_{\mu^+\mu^-}$ and $\sigma^{\bar{\nu}}_{\mu^+\mu^-}$ are the integrals over y of the differential cross section. In general, the extraction of the strange sea will be energy dependent, since one is dealing with the transition from a light to a heavy quark, and the appropriate variable is the slow rescaling variable[2] $\xi = x(1 + M_c^2/Q^2)$. More significantly, η is expected to increase with Q^2, following the general trend for sea quarks predicted by QCD.[3] Figure G1 shows a QCD calculation[4] for η as a function of Q^2. It should be noted that the Q^2 dependence of η is predominantly logarithmic in Q^2 and requires a large range of Q^2 to accurately measure such a variation.

There are two major experimental difficulties in measuring η. The first consists of background contributions from non-prompt π and K decays. The second is due to the requirement that the second muon penetrate a minimum length of steel before it is distinguished from a penetrating hadron. This results in a biased sample of events that must be efficiency corrected.

Figure G2 illustrates these considerations for the case of the production of opposite sign dimuons by neutrinos as a function of the neutrino energy. The upper part of the figure shows the relative rate for charm production and detection including both the effects of the charmed quark threshold and the minimum momentum requirement for the second muon. At the higher neutrino energies a significantly larger fraction of charm induced events is detected, reducing the uncertainty due to model dependent calculations of the efficiency.

The lower half of the figure illustrates the results of two empirical approaches to obtaining the background due to π and K

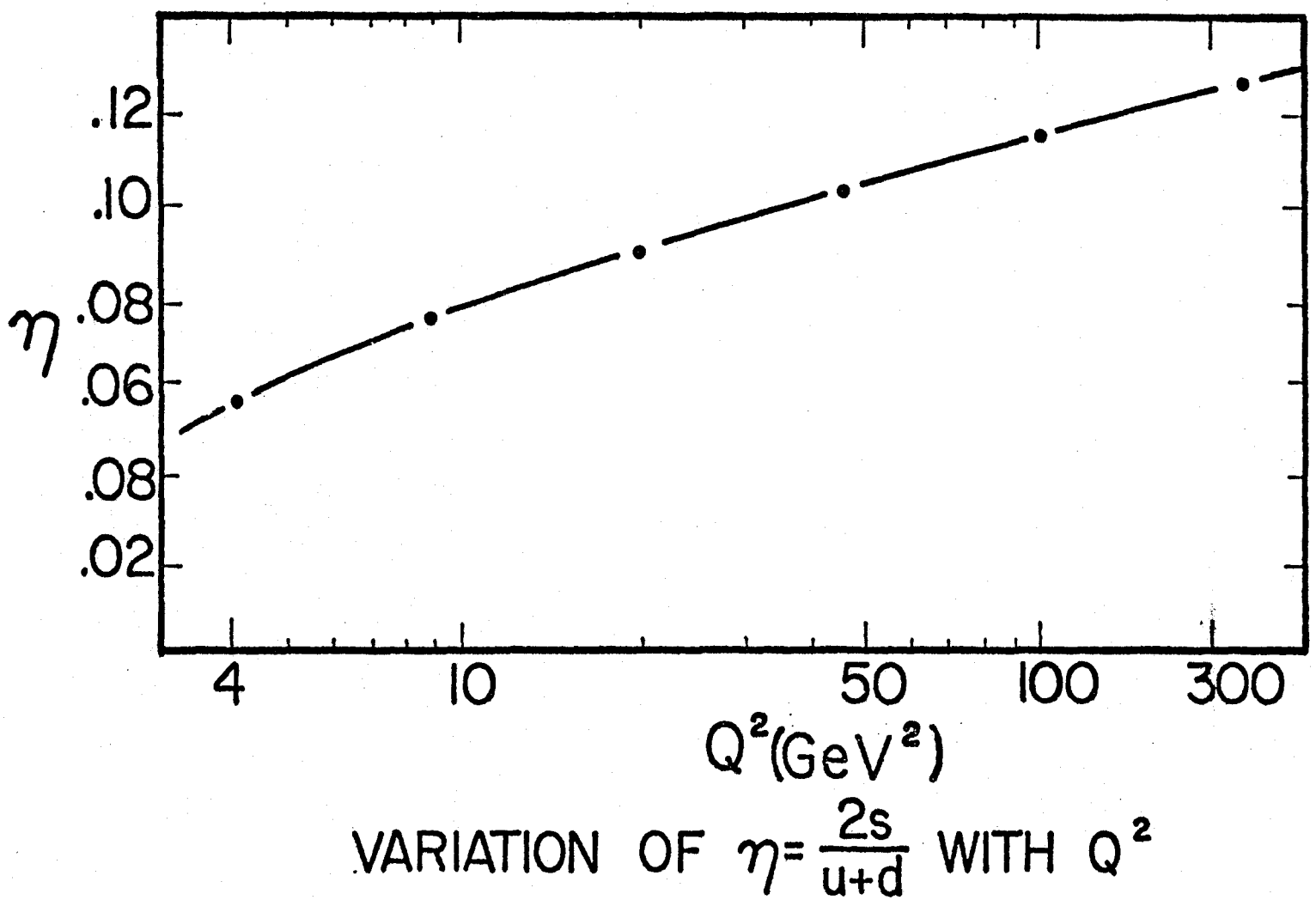

Figure G1 : Results of a QCD calculation[4] on the dependence of the strange sea on Q^2.

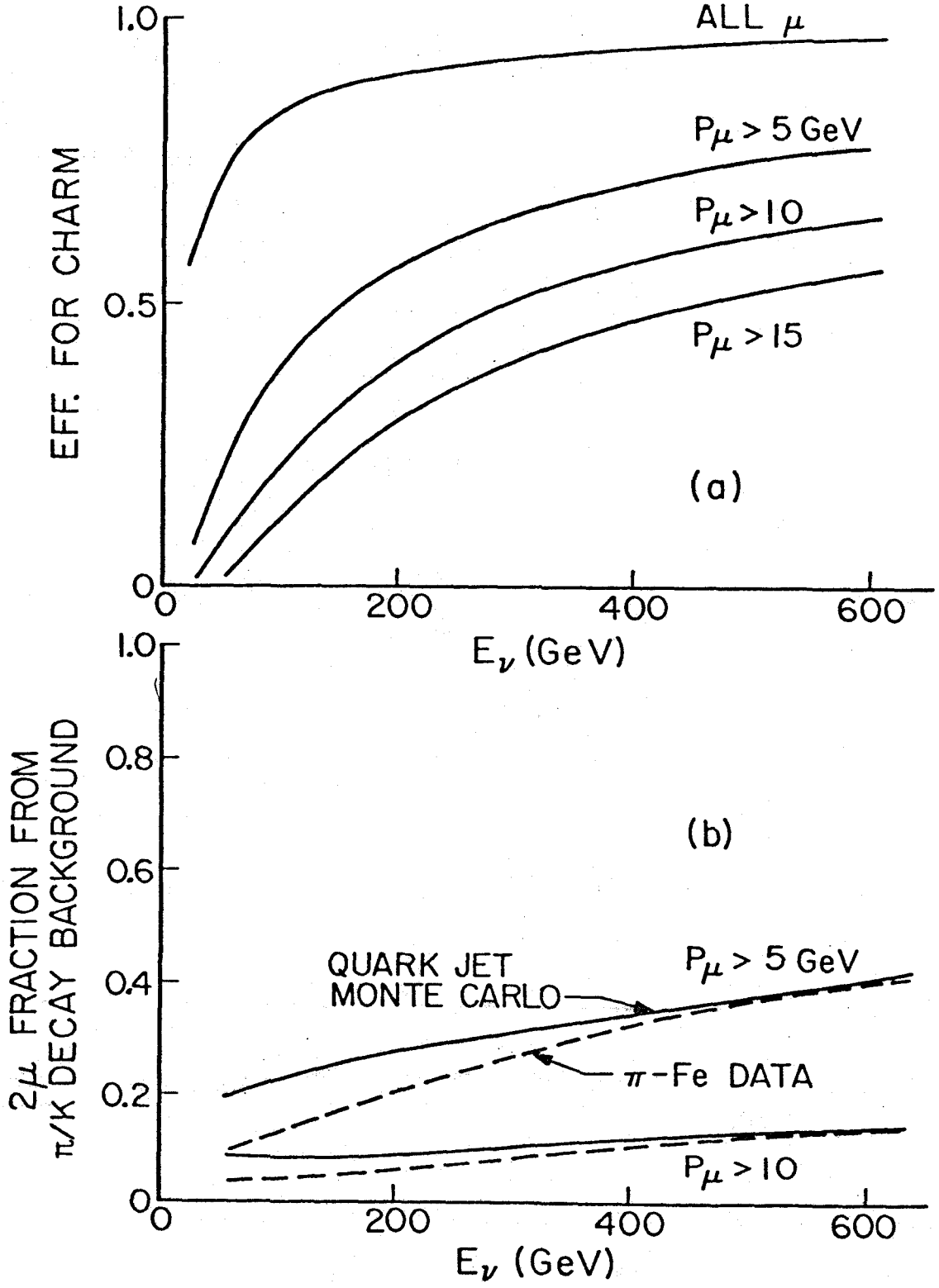

Figure G2 : (a) Efficiency for observing charm induced opposite sign dimuon events versus the incident neutrino energy. The various curves correspond to different momentum requirements for the second muon.

(b) Background for opposite sign dimuon events from π and K decay. The two sets of curves correspond to different momentum requirements for the second muon. The two different ways of estimating this background are described in the text.

decay. The first method assumes that the non-prompt muon background in ν-nucleon collisions is the same as the one in π-nucleon collisions at the same center-of-mass energy. The non-prompt muon rate in π-nucleon collisions has been measured[5] in E379 at FNAL. The second method utilizes Feynman-Field fits[6] to bubble chamber data[7] to determine the multiplicity and the energy distribution of hadrons produced at the primary neutrino interaction. These distributions are used to determine the muon rate due to hadron decay before interaction. Subsequent interactions of these hadrons are treated as in the first method. The two approaches differ by as much as a factor of two for neutrino energies below 200 GeV leading to a systematic error of 10% in determining the strange sea in this region. Furthermore, these calculations indicate that at higher neutrino energies it is necessary to require a correspondingly higher momentum for the second muon to avoid intolerable contamination from the non-prompt background.

The proposed Tevatron data will increase the amount of dimuon data by approximately a factor of four for energies greater than 150 GeV where our efficiency is reasonably high. One can imagine a scenario in which data from this energy range will be used to restrict the production parameters for charm production enough so that a suitable model will exist to correct the data at lower neutrino energies.

2. Same Sign Dimuon Events

Same sign dimuons produced in neutrino-nucleon collisions have been recently observed in a number of experiments[8]. Within the present limited statistics the results from various experiments are consistent amongst themselves, after allowing for the different beam energies. One possible mechanism for dimuon production is feed-down from trimuons (see Section 3), where the energy of one of the muons is too low to satisfy the range criterion; however, this process has too small a rate to account for the observed signal. A more likely mechanism is associated charm production, the QCD process where a struck quark bremsstrahlungs a gluon which then dissociates into a $c\bar{c}$ pair. Calculations[9] of the rate of same sign dimuon production due to this process predict a rate roughly two orders of magnitude lower than the observed one. However, these calculations are sensitive to second order corrections. In addition, the BNL-COL bubble chamber group does not observe the expected enhancement in the V^o rate associated with same sign dilepton events at lower Neutrino energies. At present, the origin of same sign dilepton events is not understood.

Figure G3 shows the $\frac{\mu^-\mu^-}{\mu^-}$ rates observed by our group (E482 at FNAL) versus the visible neutrino energy. Also shown for comparison is a QCD prediction for associated production of charm. The calculated π/K background is 3 events whereas 12 events are observed. The probability that the 12 events are all due to background is less than 10^{-5}. The azimuthal angle distribution observed for the second muon indicates that the events are associated with the hadronic vertex. Most striking, however, is the sharp dependence of the same sign event rate upon the neutrino energy. Clearly higher neutrino energies will be important to understand the source of the same sign dimuon events.

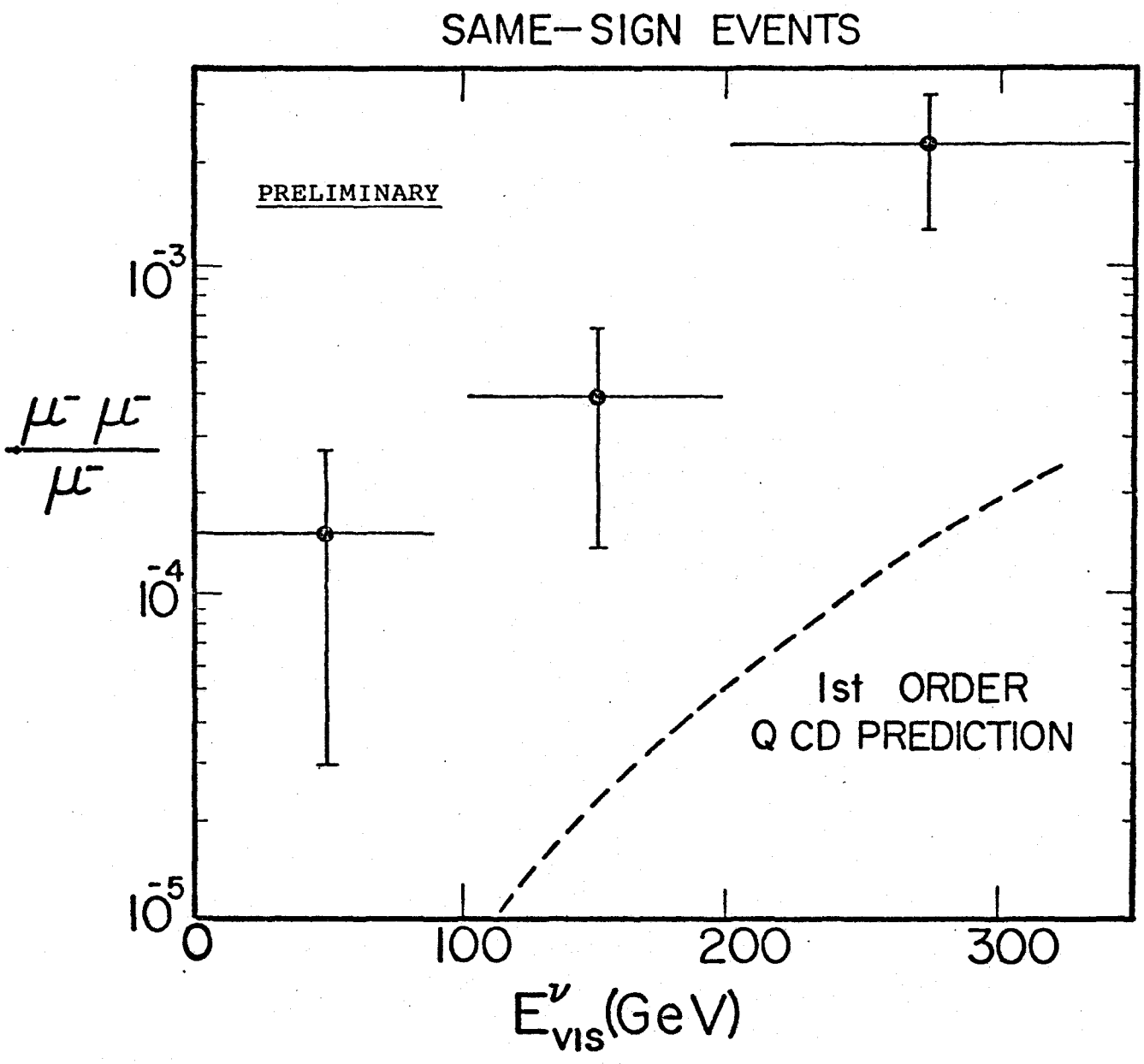

Figure G3 : Rate for producing same sign dimuon events normalized to the single muon production rate for charged current neutrino interactions versus the visible neutrino energy. The data are from experiment E-482 .

3. Production of New Heavy Flavor Particles

The production of new heavy flavored particles in neutrino-nucleon collisions is another process that can be investigated through the study of multimuon final states.[10] Top and bottom quarks may be produced off the valence (u,d) quarks and off the strange sea, but the rate for such a process may be rather small due to the small mixing angles in the "standard" six-quark mechanism of Kobayashi and Maskawa. On the other hand, bottom production off the charmed sea may be sizable since the relevant mixing angle may be large.

The most spectacular manifestation of the production of a new flavor may be the observation of quatro-muon events like:

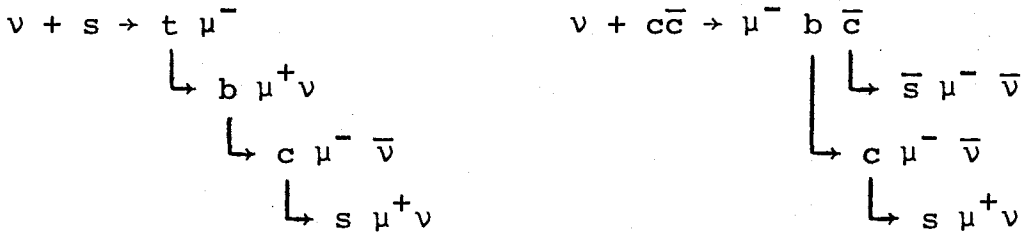

Care must be taken in the analysis of such events to account for all the backgrounds due to more conventional sources (e.g. hadron decay, Bethe-Heitler muon pair production) in a manner similar to the one described in the previous sections. A more reliable, and more pedestrian, search for the production of new heavy quarks would utilize the fact that the muons produced in the semi-leptonic decay of such quarks are expected to have a larger transverse momentum than the muons from more conventional sources (e.g. from charm decay). The energy dependence of a signal of high-p_t muons and the observation of any threshold effects would allow one to estimate the mass of the heavy quarks.

All of the above is highly speculative; the mitigating fact that allows its presentation is the historical precedent: the first indication for charm production was the observation of dimuon events in neutrino-nucleon scattering!

REFERENCES

1. S. L. Glashow, J. Iliopoulos and L. Maiani, Phys. Rev. D 2, 1285 (1970).
2. R. M. Barnett, Phys. Rev. Lett. 36, 1163 (1976).
3. See, for example, R. Field, Applications of Quantum Chromodynamics, CALT-68-696.
4. R. Field and G. Fox, private communication.
5. M. Shaevitz, private communication.
6. R. Field, private communication.
7. T. H. Burnett et al., Phys. Lett 77B, 443 (1978); Bierge et al., Fermilab-Pub 78/43-EXP (1978).
8. See, for example, the review of M. Murtaugh in the Proceedings of the 1979 International Symposium on Lepton and Photon Interactions at High Energies, Fermilab, Batavia, Illinois, 1980.
9. B. L. Young, T. F. Walsh and T. C. Yang, Phys. Lett. 74B, 111 (1978).
10. See, for example, L. Maiani in Proceedings of the 1977 International Symposium on Lepton and Photon Interactions at High Energies, DESY, Hamburg, Germany, 1978.